Calibration Studies of the Front-End Electronics for the ATLAS New Small Wheel Project

Bohan Chen
Department of Physics
McGill University
February 2019

A thesis submitted to McGill University in partial fulfillment of the requirements of the degree of Master of Science

Abstract

To continue to probe new avenues of physics, the Large Hadron Collider (LHC) will see a series of upgrades starting in 2019 that will see the luminosity surpass the design specifications. The increased data intake will quickly exceed the capabilities of the current data-acquisition systems of the ATLAS experiment. Therefore, several sub-systems of ATLAS will also undergo a number of upgrades in parallel with the LHC. One of these areas is the New Small Wheel project, which forms one sub-system of the muon detectors. The current detector technology will be replaced with small-strip thin gap chambers (sTGCs) and micro-mesh gaseous detectors (micromegas). This thesis will highlight McGill's role in testing the individual sTGC detectors. Specifically, much of the work presented relates to the preparation of specially designed boards and integrated circuits used in data-acquisition. During this process, both the analog and digital baselines are measured along with any faulty or erratic channels. In doing so, a custom algorithm is developed in order to calculate the pedestal for each readout channel. The results of these scripts are then implemented in a much larger cosmic ray analysis software application that then determines the efficiency of the detector among other metrics of performance.

Résumé

Pour continuer à explorer de nouvelles voies de la physique, le grand collisionneur de hadrons (LHC) bénéficiera à partir de 2019 d'une série de mises à niveau qui permetra à la luminosité de dépasser les spécifications de conception. L'augmentation du volume de données dépassera rapidement les capacités des systèmes actuels d'acquisition de données d'ATLAS. Par conséquent, plusieurs sous-systèmes d'ATLAS feront également l'objet de plusieurs mises à niveau parallèlement au LHC. L'une de ces mises à niveau est le projet New Small Wheel, qui constitue l'un des sous-systèmes des détecteurs de muons. La technologie de détection actuelle sera remplacée par des chambres à petite bande mince (sTGC) et des détecteurs de gaz à micro-mailles (micromégas). Cette thèse mettra en évidence le rôle de McGill dans le test de chaque détecteur sTGC. En particulier, une grande partie du travail présenté concerne la préparation de cartes et de circuits intégrés spécialement conçus pour l'acquisition de données. Au cours de ce processus, les lignes de base analogiques et numériques sont mesurées ainsi que tous les canaux défectueux ou erratiques. Ce faisant, un algorithme personnalisé est développé afin de calculer le piédestal pour chaque canal de lecture. Les résultats de ces scripts sont ensuite implémentés dans un logiciel d'analyse des rayons cosmiques qui détermine l'efficacité du détecteur parmi d'autres paramètres de performance.

Acknowledgements

The work presented in this thesis would not have been possible without the support of many people. The first person that I would like to acknowledge is my M.Sc supervisor, Prof. Andreas Warburton. From our meetings, I was able to gain a better understanding of the academic process as well as the field of particle physics in general. This is in addition to taking time out of his busy schedule to offer feedback and advice in the writing of this document.

Secondly, I would also like to extend a thanks to Prof. Brigitte Vachon. As the supervisor of the sTGC lab, she provided an immeasurable amount of support in terms of the work presented in this thesis. In doing so, she never hesitated to pass on her expertise about the quadruplet and the new small wheel project as a whole. Another member of the lab who I have had the great pleasure of working alongside with is our post-doctoral fellow, Tony Kwan. I would like to thank Tony for giving me the countless hours of advice and guidance on nearly aspect of my project from the very start of my thesis right up to the completion of my degree.

I would also like to thank my colleagues in the McGill ATLAS group, who have given me an opportunity to learn about other avenues of research. In particular, I would like to acknowledge Benoit Lefebvre and Waleed Ahmed who have had a direct impact on the success of the sTGC project as developers of the cosmic ray analysis software.

On a more personal level, I would also like to mention John McGowan who assisted with many of the measurements. Lastly, I would like to thank Thomas Rosin who I have known since my second undergraduate year and has helped me with the translation of my abstract.

Finally, I would like to thank my parents, Angela and Roger, and my younger sister who is just about to start her university career. They have always instilled in me a sense of hard work and have always encouraged me to pursue a field that I was passionate about.

Contribution of Authors

The author makes no contributions in the following sections: Introduction (Section 1), Theory: Particle Properties and their Detection (Section 2) and Apparatus (Section 3). These sections were included as contextual information. The author contributed in the McGill sTGC Testing Lab section (Section 4) by participating in the preparation of the lab space for the arrival of the production detectors. The author made contributions in the QS3P.4 Set-up section (Section 5), specifically pertaining to the readout electronics as well as developing several scripts used to perform the measurements described in this section. Finally, the author also made contributions described in Appendix A by participating in the data taking used to develop the hit maps. The author did not develop the cosmic ray analysis software in Appendix B but did contribute to the advancement of the software from the results obtained in the thesis. Lastly, the author compiled the mapping scheme of the QS3P described in Appendix C, derived from an official mapping guide supplied by the sTGC collaboration.

Contents

List of Figures

List of Tables

1 Introduction

The standard model (SM) has been heralded as a great success in the field of subatomic physics predicting the existence of particles decades before actual detection and observation. Much of these successes have resulted in the expansion of the SM with the addition of new particles. However the SM is not without its shortcomings, and a great deal of the modern day particle physics searches are dedicated to bolstering these discrepancies. Popular topics such dark matter, neutrino oscillations and super-symmetry are just a few examples of so-called Beyond the Standard Model (BSM) phenomena that are areas that have seen rapid growth in the past decade. With new frontiers of energy being achieved, it is likely that these areas will see increased activity in the years to come.

Many of the searches for new phenomena as well as precision measurements of known SM processes are conducted at collider based experiments such as the Large Hadron Collider (LHC). Collider based experiments are able to observe processes occurring at the upper limit of terrestrially achievable energy scales. At the LHC, currently the world's highest energy particle accelerator, the energy reaches a maximum of 13 TeV. Located underneath the France-Switzerland border, protons are accelerated through a chain of pre-accelerators before being injected into the 27 km ring and accelerated up to this energy limit. At these energies, collisions of oppositely rotating protons generate a large number of interesting processes.

In order to gather all of the information needed to reconstruct an event, large scale particle detectors such as ATLAS are built around the LHC ring at one of the interaction sites. The ATLAS detector is composed of a number of sub-systems that are arranged in concentric cylindrical shells around the interaction point. As one of two general purpose detectors, ATLAS conducts both precise measurements of SM processes as well as tests of BSM theories.

In 2019 the LHC will see an increase in the intensity of the proton beams during the long shutdown. This will undoubtedly open new avenues for potential physics research, but comes with the challenge of coping with the increased rate of data-collection. The current data buffers will quickly be overrun and the readout electronics won't be able to cope with this increased rate. Therefore upgrades are planned for experiments such as the ATLAS detector to reduce the data-taking rate to a much more manageable level by reducing triggers on background events.

One area that is being upgraded are the small wheels, found on the inner end caps and make up part of the muon system. The current detector technology will be replaced with small-strip Thin Gap Chambers (sTGC) and Micro-mesh Gaseous Detectors (Micromegas) to deal with the increased rate. Canada is part of a 5-country collaboration that constructs and tests the individual sTGC detectors. The majority of the work described in the thesis relates to the preparation of a functioning test bench at McGill University for conducting cosmic ray tests of individual sTGC. Along with preparing the space, characterization and calibration studies are performed on the specially designed front-end boards used to read out cosmic ray hits. During these studies, the threshold for each chip is determined and the status of each readout channel is verified. These results are then incorporated into a cosmic analysis software created by members of the McGill sTGC group[1] (Benoit Lefebvre, Waleed Ahmed) that is used to characterize the performance of the detector.

1.1 Thesis Outline

The thesis begins with a general overview of the fundamental properties of the Standard Model in Section 2. Since this thesis revolves around detectors, the same section contains a brief discussion on particle interactions with matter and describes the operating principles of ionization chambers, the class of detectors that the sTGC belongs to. Section 3 describes some of the general features of the LHC and the ATLAS detector. Here, the NSW project is introduced and Canada's role in the project is also illustrated. Sec-

[1]sTGC Cosmic Analysis Software Gitlab: `https://gitlab.cern.ch/McGill-sTGC/tgc_analysis/`

tion 4 describes the various systems making up the sTGC testing lab at McGill University. Section 5 describes the procedure of characterizing the two different readout boards and gives the results of these procedures. Section 6 concludes the thesis by providing a summary of the project as well as providing areas that could be improved as part of potential future work. Lastly, Appendix A contains examples of hit maps from an actual cosmic data-taking run. Appendix B shows the efficiency plots produced by the cosmic ray analysis software. Finally, Appendix C contains a description of the mapping scheme between electrode number and read out channel number.

2 Theory: Particle Properties and Their Detection

This section will begin by covering the basic properties of the particles making up the current Standard Model (SM). Furthermore, some of the defining theories that have led to the current understanding of the SM are highlighted and discussed. In doing so, the successes and failures of the SM are also discussed. Finally, since the content of this thesis is related to particle detection, a subsection is provided on particle interactions with matter as well as a detailed discussion of the different detector techniques.

2.1 The Standard Model (SM)

All matter in the known universe is composed of elementary particles and is subjected to one or more of the four fundamental forces: strong, weak, electromagnetic and gravity. The Standard Model of Particle Physics details the interactions of these elementary particles and the fundamental forces. The development of the theory occurred in steps and largely began with the unification of the Electromagnetic and the Weak forces in 1961, a theory known as the Electroweak interaction developed by Sheldon Glashow [1]. This would be further expanded upon in 1967 by Steven Weinberg [2] and Abdus Salam [3] when they included the Higgs Mechanism into Glashow's Electroweak theory. Following this, the Strong interaction (one of the four fundamental forces) would be included following the proposal of asymptotic freedom in 1973-74 [4]. Asymptotic freedom of Quantum Chromodynamics (QCD), developed by David Gross and Frank Wilczek 1973, is the notion that the strength of interactions involving some particles decrease as they come closer together or as the energy increases [5]. The modern day Standard model is organized into two groups of particles, fermions and bosons. Fermions are characterized as having half-integer spin states while bosons are recognized as having integer spin states.

The fermion group of the SM is further subdivided into two sub-groups, namely the quarks and the leptons that form the basic building blocks of matter. The model includes six quarks and six leptons and their respective anti-particles, organized into three two particle groups known as generations. The boson group includes 4 gauge bosons which are the force-carriers of the strong, weak and electromagnetic force. The gravitational force has not been correctly incorporated into the current understanding of the standard model. In 2012, the ATLAS Collaboration announced the discovery of the scalar Higgs boson [6], which by the Higgs mechanism gives the other gauge bosons mass. An illustration of the different fermions and bosons is shown in Figure 2.1.

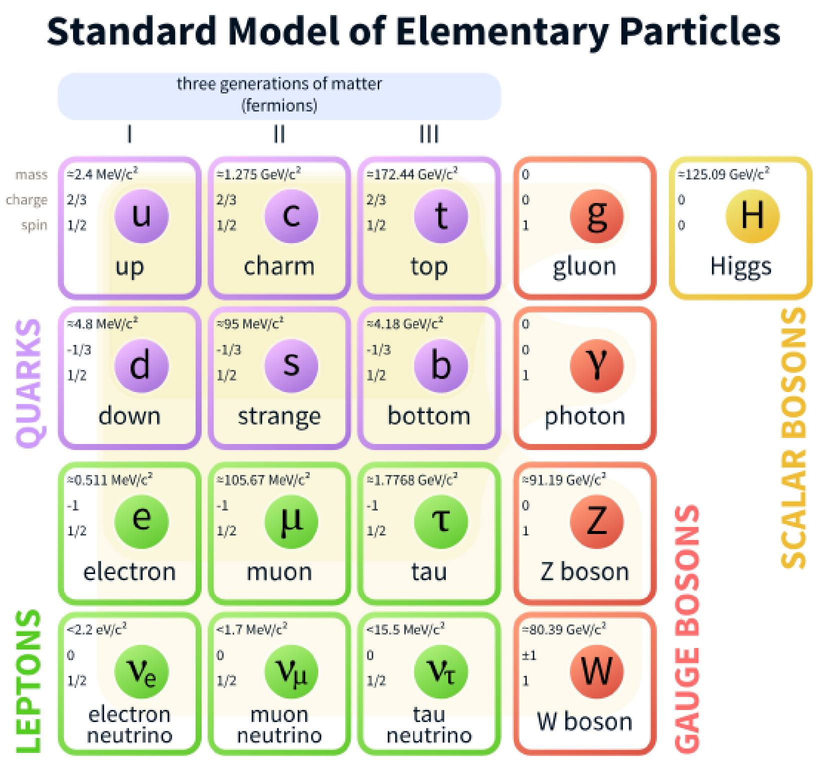

Figure 2.1: Standard model of particle physics detailing the different elementary particles including their mass, charge and spin. [7]

The quark model was first independently proposed by Murray Gell-Mann [8] and George Zweig [9] in 1964. Their theory only predicted the up, down and the strange quark. The remaining quarks would be observed in later decades ending with the discovery of the top quark in 1995 by the CDF and D∅ experiments at Fermilab [10]. Quarks hadronize in groups of two (mesons) or three (baryons) to form more complex particles such as the basic constituents of atomic nuclei, the proton (*uud*) and the neutron (*udd*). More complex structures involving groups of five quarks, known as pentaquarks have also been observed.

The leptons are also made up of three generations, the electron, muon and tauon and their respective neutrinos. Neutrinos were long believed to be massless, however the theory of neutrino oscillations (a prediction first put forth by Bruno Pontecorvo in 1957 [11]) would eventually attribute mass to the neutrinos; this is the quantum mechanical ability of neutrinos to change from one leptonic flavour to another. This phenomenon would eventually be observed in atmospheric neutrinos by the Super-Kamiokande experiment [12] in 1998 and the Sudbury Neutrino Observatory (SNO) [13] in 2002. This discovery would lead to the Nobel Prize in Physics in 2015. The electron is one component of the atom and is therefore ultra stable; it is also the lightest of the three leptons with a mass of approximately $0.5\ MeV$. On the other hand, the muon and the tauon are much heavier compared to the electron with masses of approximately $100\ MeV$ and $1700\ MeV$ respectively; they are also extremely unstable [14].

The four gauge (vector) bosons are described as mediators of the fundamental forces such that particle interactions will include one or more of these particles. The photon carries the electromagnetic force, the $W^{\pm}$ and the Z^0 (approximately $80\ GeV$ and $90\ GeV$ respectively) carry the weak force and the gluon (theoretically massless) mediates the strong force [14]. The prediction of the existence of these particles as well as approximations for their masses were seen as one of the great successes of the Standard Model. However, the SM says nothing about gravity, due to its extremely weak strength.

The Higgs Boson differs from the other bosons because it is a scalar particle, meaning that it is invariant under a parity transformation. In addition, the Higgs is also the most massive of the bosons with a mass of approximately $125\ GeV$ [14]. The Higgs is not a mediator of any fundamental force, but rather is a quanta of the Higgs Field, particles generate mass by interacting with this field via the Higgs mechanism. A successful model of mass generation without breaking gauge theory was worked out by three groups in 1964: (1) Robert Brout and François Englert, (2) Peter Higgs, (3) Gerald Guralnik, C. R. Hagen, and Tom Kibble [15–17].

The prediction of the Higgs boson and subsequent observation confirmation in 2012 was seen to be one of the successes of the Standard model. As mentioned above, some of the other successes revolve around the prediction of the existence of the other elementary particles before the actual observation. Another success of the standard model relates to the measurement of the anomalous magnetic dipole moment of the electron results from first-order loop corrections. This result was first discovered by Julian Schwinger in 1948 [18], and offers a precise test of Quantum Electrodynamics (QED). This yielded a very precise prediction of the fine-structure constant, which agrees with experiment to more than one part in one billion, specifically $\alpha = 137.035999710(96)$ is currently the most precise measurement of the fine-structure constant [19]. As a result, QED is one of the most precisely measured theories ever put forth.

Despite all of the recent successes, the Standard Model is not without its deficiencies. One of the most prominent areas of the Standard Model that needs modification revolves around the non-zero mass of the neutrinos. The current Standard Model predicts neutrinos to be massless, however the recent observation of neutrino oscillations attributes a non-zero mass to the neutrinos, disagreeing with the underlying theory in the Standard Model. Another problem of the Standard Model is the so-called Hierarchy problem which has to do with the large discrepancy in strength between the weak nuclear force and the gravitational force, a discrepancy on the order of 10^{24} [20].

Some of the aforementioned areas may be addressed by more exotic theories beyond the standard model. One exotic theory that is actively being pursued is the Supersymmetric theory. This theory proposes that there exists a relationship between the two classes of particles, Bosons and Fermions. Supersymmetric particles (SUSY) state that each particle of one spin type would have a partner with a particle in the other spin type. Supersymmetry is an exciting field of study because it could be the solution to some of the issues befalling the standard model. Undiscovered SUSY particles could be dark matter candidates; neutralinos have been considered a strong candidate for the constituent particles of dark matter [21]. Supersymmetry can also resolve the Hierarchy problem, by avoiding issues with fine-tuning between the electroweak scale and the Planck scale that afflicts the Hierarchy problem without SUSY [22].

2.2 Particle Interactions

The basis of particle detectors revolves around understanding the basic properties of the particles of interest and understanding their interactions with matter to produce an observable signal. Particles can be split into two groups depending on whether the particle is charged or uncharged, and the two different groups of particles interact with matter very differently. Charged particles interact via two main processes, either by exciting bound atomic electrons (soft inelastic collisions), or ionization (hard inelastic collisions) [23]. Other interactions inlude Bremsstrahlung, Cherenkov radiation, transition radiation and nuclear reactions; these have much less of an effect than energy loss through ionization. The equation relating energy loss of a charged particle passing through a target material is given by the famous Bethe-Bloch equation [24]:

$$-\left\langle \frac{dE}{dx} \right\rangle = \frac{4\pi}{m_e c^2}\frac{nz^2}{\beta}\left(\frac{e^2}{4\pi\epsilon_o}\right)^2\left[ln\left(\frac{2m_e c^2\beta^2}{I(1-\beta^2)}\right)-\beta^2\right]; n = \frac{N_A Z\rho}{AM_\mu} \tag{1}$$

The Bethe-Bloch equation only depends on the velocity of the incoming particle and not the mass of the particle through the β-factor. The parameters that depend on the target material are the atomic number, Z, the average atomic mass, A, the density, ρ, and the molar mass constant, M_μ. In addition, there is an additional constant, I which is referred to as the mean excitation energy and is a property of the material. The graphical form

form of the Bethe Bloch for different particles of varying momentum in different materials is shown in Figure 2.2. There are a few regions of interest for different momenta. Perhaps the most relevant for the purposes of this thesis is the minimum of each curve. This point is known as the minimum ionizing particle, and occurs for relativistic particles whose energy loss rates are close to the minimum.

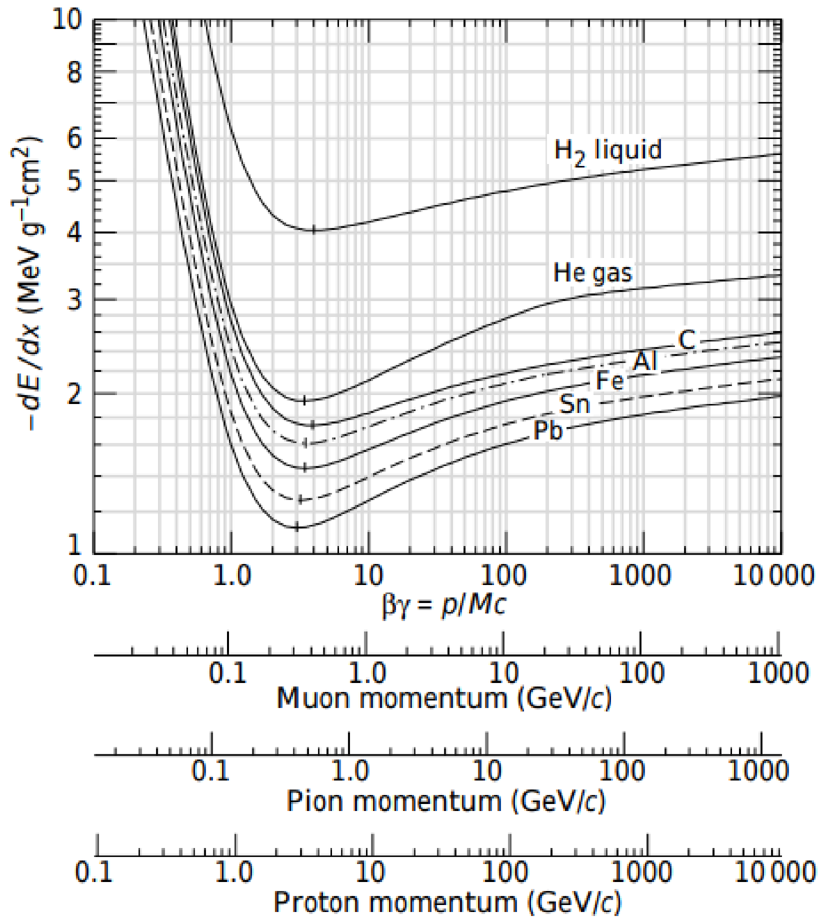

Figure 2.2: Mean energy loss for different particles in various materials plotted in units of $\beta\gamma$, which is related to the momentum of the particle. [14]

Uncharged particles, such as photons interact differently with matter than charged particles and interact via three main processes whose cross-section depends on the energy of the photon. At low energies, the photoelectric effect dominates whereby the photon is absorbed by an electron in the material and subsequently ejects an electron, assuming that the original energy of the photon surpasses the work function of the material. At medium energies, Compton scattering dominates, whereby the photon collides with an electron in the material causing the electron to scatter off at an angle resulting in a wavelength shift of the scattered photon. At high energies, the incoming photon mainly loses energy via pair production, here the incoming photon interacts with nuclei in the material resulting in the creation of an electron-positron pair [23], the minimum energy for this process to occur is approximately $1.02\ MeV$, which is the mass of two electrons. All three processes are captured in Figure 2.3 comparing the cross-sections of the three processes mentioned above as a function of the energy of the photon.

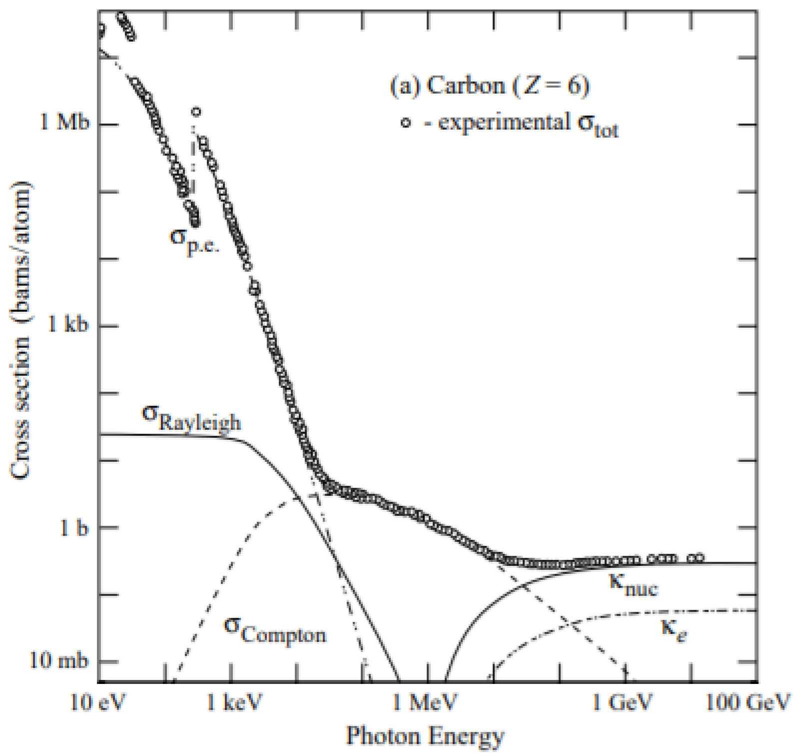

Figure 2.3: Cross section of the three main energy loss processes for photons. Different processes dominate at different energy regimes [14].

2.3 Cosmic Rays

Cosmic rays is a term that is given to energetic forms of radiation that originate from sources usually outside of the solar system and are mainly composed of protons and alpha particles with trace amounts of other atomic nuclei [25]. One source of cosmic rays proposed by Baade and Zwicky in 1934 suggested that a large majority of cosmic rays originates from supernovae [26] where the supernovae outburst accelerates the shower of particles to the high energies characteristic of cosmic rays. When a high energy cosmic ray interacts with particles in the upper atmosphere, the cosmic ray can initiate a shower of new particles as shown in Figure 2.4, which illustrates the different components that can make up an air shower. Secondary particles produced by a primary event particle can contain an electromagnetic component containing electrons, positrons, and photons. However, secondary particles can also be hadronic in nature, hadrons such as protons, neutrons, pions and kaons can all be found in air showers. Other elementary particles such as muons and neutrinos are produced by the further decay of secondary particles (such as pions).

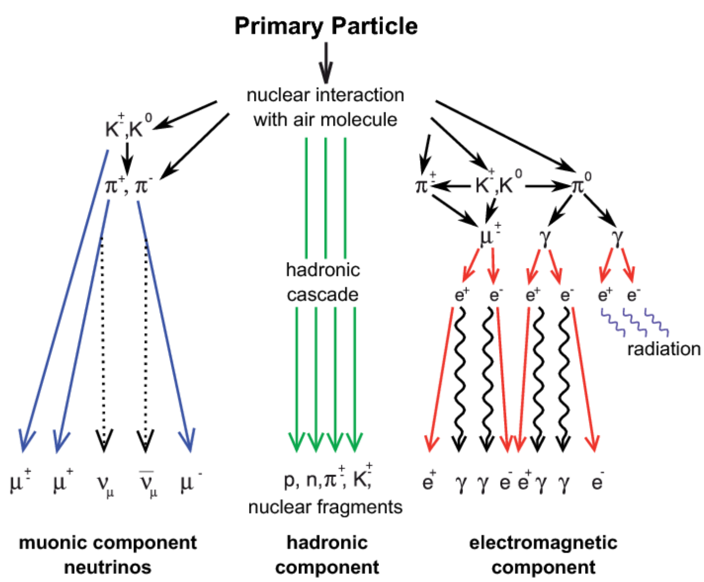

Figure 2.4: A cosmic ray possibly originating from a supernovae event interacting with the Earth's atmosphere results in a cascade of secondary particles through various processes leading to different components of the air shower [27].

Most experiments aim to filter out the constant background of cosmic rays in order to isolate their signal. Experiments looking to observe exotic events are often found underground in order to use the natural shielding of the earth to reduce the rate of background events. However, cosmic rays do have advantages for use in certain situations. Secondary particles have a large spectrum of energies and are generally emitted isotropically making them an attractive candidate for use in the testing of certain detectors.

2.4 Basics of Particle Detectors

As shown above, there is a wide variety of different particles whose interaction depends on the characteristics of the incoming particle as well as the detector material. Furthermore, depending on what information needs to be measured, there has been an equally wide variety of detection techniques developed. Therefore for the purposes of this thesis, this subsection will only focus on the basics of scintillators, photo-multiplier tubes (PMT) and ionization detectors relevant for the purposes of this thesis.

2.4.1 Scintillators

Scintillators are a class of materials that have the property that, when struck by an incoming particle, the energy of the particle is absorbed and re-emitted as light. The actual material can be inorganic crystals, organic crystals, liquids or gases [23] whose light production mechanism differs depending on the material. An important feature and one of the main advantages of scintillators is the fast response time, here response time is defined as the time between the initial absorption of the primary particle and the emission of light. This allows scintillators to minimize dead time and maximize the collection rate of particles. Specifically a good approximation for the time evolution of the light can be accurately described by a two part exponential:

$$N = A \exp\left(\frac{-t}{\tau_f}\right) + B \exp\left(\frac{-t}{\tau_s}\right) \tag{2}$$

Where in the above equation, the number of photons N decays exponentially comprised of a fast component and a slow component characterized by a fast decay constant,

τ_f and a slow decay constant τ_s, respectively. This is depicted in Figure 2.5 showing these two exponential decay components.

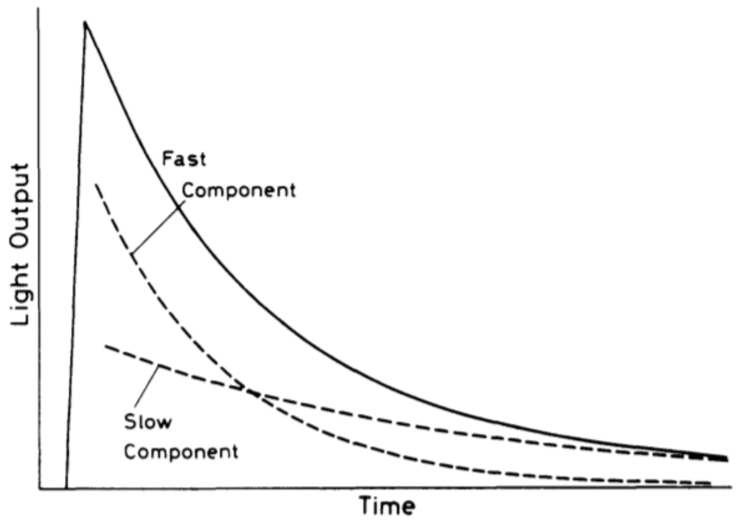

Figure 2.5: Light produced by scintillating materials can be accurately described by a sum of decaying exponential with a slow and fast decaying component (dotted lines), the emission time is shown as the gap between the origin and the peak of the solid line and this can vary depending on the scintillating material [28].

To further increase light collection, scintillators are often wrapped with an opaque material in order to make use of total internal reflection as well as to reduce stray activation by ambient light. Finally, scintillators are often combined with light guides that direct the light to photomultiplier tubes for collection and transformation into an analog signal.

2.4.2 Photo-Multiplier Tubes (PMTs)

The first photomultiplier tube can be traced back to 1934 whose action was first demonstrated by Iams and Salzburg [29] and were able to attain a gain of eight. PMTs are devices that are extremely sensitive to light and are able to produce secondary electrons using the photoelectric effect. As mentioned above, PMTs are often coupled to the ends of scintillators as shown in Figure 2.6

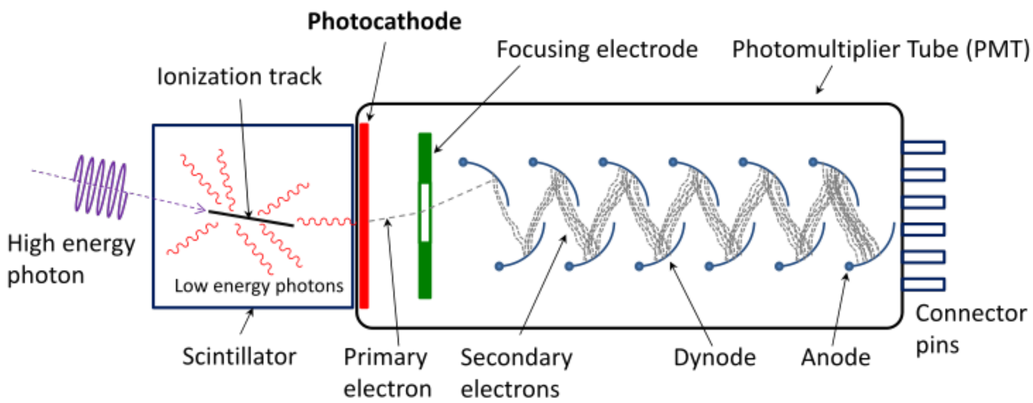

Figure 2.6: Photomultiplier tubes connected to scintillators produces photoelectrons via the photoelectric effect that are then accelerated through a potential difference towards a series of dynodes initiating an avalanche of photoelectrons arriving at the cathode [30].

The basic operation of a PMT begins with photons produced through scintillation impinging on a photocathode with a low work function as to begin the avalanche of photoelectrons. Because the PMT is held at a potential difference, the photoelectrons are accelerated towards the first dynode producing secondary electrons upon being impacted with accelerated electrons. After traversing a series of these dynodes, the multiplied signal is collected at the anode.

2.4.3 Ionization Detectors

Ionization is a significant energy loss process for charged particles. Ionization detectors measure the amount of ionized charge produced by a charged particle traveling through a gas volume. The simplest configuration for an ionization chamber involves two planar electrodes held at a potential difference with a gas contained in between the two electrodes [23]. When a charged particle passes between the electrodes and ionizes the gas, the positive and negative ions drift towards opposite electrodes that can be read out as a signal.

A significant improvement on the basic planar ionization chamber was made in 1968 by Georges Charpak with the multi-wire proportional chamber (MWPC) [31]. In a MWPC, the anode plane is replaced by a plane of equally spaced anode wires held at a positive potential sandwiched between two cathode planes. When a particle passes between the cathode planes and produces ionization, the ions drift towards the nearest anode wire, generating a signal. The basic structure of a MWPC is shown in Figure 2.7.

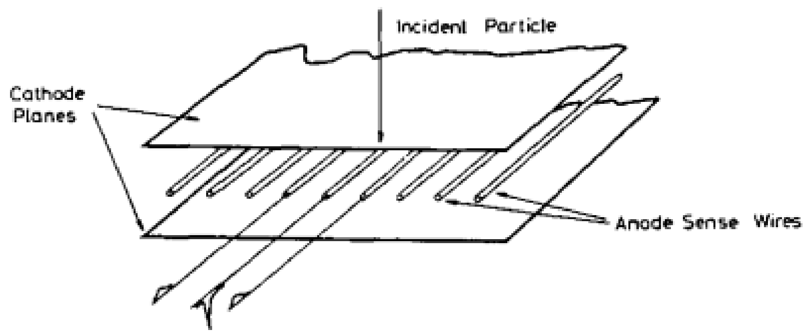

Figure 2.7: Multi-wire proportional chambers contain one or more planes of equally spaced anode wires in between two cathode planes. A charged particle passing through this space ionizes the gas; the ions then drift towards the nearest anode wire generating a signal. One of the successes of the MWPC was the much improved spatial resolution which could be further improved upon by minimizing the spacing between the wires [28].

The many advantages of a MWPC make it an attractive choice for many detector operations. For one, by dividing the anode plane into individual wires, the spatial resolution of the particle is greatly improved, furthermore, by combining more than one plane of anode wires, a complete three dimensional coordinate can be established. Finally, since each wire acts as an independent detector, it was possible for more than one track of particles to be detected at any one time. This would greatly decrease dead time and increase the rate [28].

3 Apparatus

This section will describe the structure of the LHC, and in particular, the different subsystems making up the ATLAS detector: inner trackers, calorimeters, muon system, triggering and data acquisition. This thesis focuses on one component of the muon system that will see an upgrade in 2019, the New Small Wheel. Therefore, a dedicated discussion of the motivation for the upgrades and detection techniques is given highlighting Canada's participation in the project.

3.1 Large Hadron Collider (LHC)

The LHC is currently the world's largest and the highest energy particle collider located underground on the France-Switzerland border and spanning $27\ km$ in circumference. The initial idea of placing a hadron collider in the tunnels of the former Large Electron-Positron collider (LEP) was proposed by former CERN director John Adams [32]. Up until this point, lepton (more specifically, electron-positron) colliders had already produced interesting results in the field of particle physics and have made up the majority of collider-based experiments up to that point. However, most hadron experiments were still confined to fixed-target experiments with the exception of the Intersecting Storage Rings (ISR) and the Fermilab Tevatron. During the next few decades, the finer details and goals of the LHC would be confirmed. The first of the proposed goals of the LHC would be to investigate the Brout-Englert-Higgs (BEH) mechanism which details the process by which the W and the Z bosons obtain mass [33]. Additional goals include investigating the electro-weak symmetry breaking, looking for signs of supersymmetry, looking for more exotic forms of matter as well as investigating the conditions of the early universe such as the quark-gluon plasma [32].

In recent years, the LHC has seen considerable success, especially in 2012 following the announcement of the discovery of the Higgs Boson. The LHC today, recently temporarily ended proton-proton operations at a center-of-mass energy of $13\ TeV$, and a design luminosity of $10^{34}\ cm^{-2}\ s^{-1}$ with a collision rate of $40\ MHz$ with approximately $25\ pp$ inelastic collisions occurring at each bunch crossing [34]. The LHC consists of two beam-pipes that cross at four interaction sites housing the four main experiments at the LHC. ATLAS (A Toroidal LHC ApparatuS) and CMS (Compact Muon Solenoid) are the two general complementary detectors. Both detectors have a similar wide variety of goals, from investigating Higgs boson processes to rare exotic searches. ALICE (A Large Ion Collider Experiment) conducts analyses on heavy ion collisions forming conditions akin to the early universe. LHCb (Large Hadron Collider Beauty) is specifically designed to study processes involving the b or bottom quark. Figure 3.1 is a schematic of the beam-pipes and the location of four interaction sites.

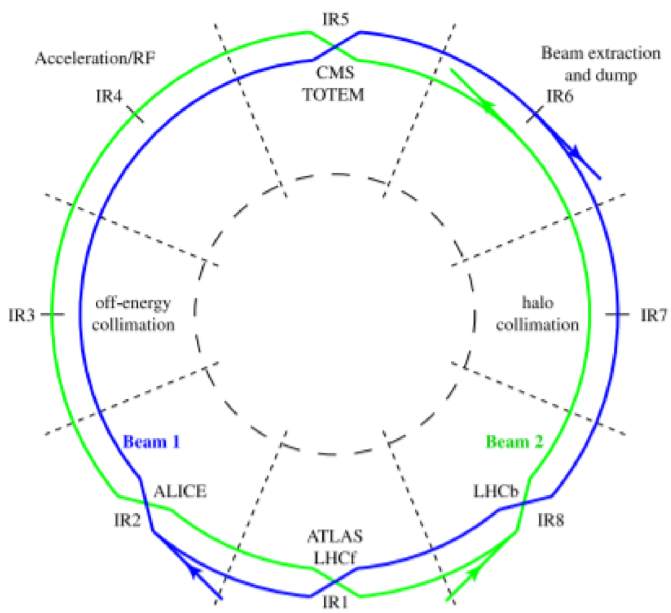

Figure 3.1: The large hadron collider is currently the world's highest energy particle collider operating at $13\ TeV$, located underneath the France-Switzerland border. Along the $27\ km$ circumference are the four main experiments: ALICE, ATLAS, CMS, and LHCb, at one of the four interaction sites. [35].

Injection into the LHC requires a number of pre-accelerators. The process begins by ionizing hydrogen gas, stripping the electrons and feeding the now bare proton into a linear accelerator ("LINAC") that accelerates the protons up to an energy of $50\ MeV$. This beam is then injected into the Proton Synchrotron Booster (PSB) accelerating the proton beam up to $1.4\ GeV$. The beam then enters the Proton Synchrotron (PS) accelerating the protons to an energy of $25\ GeV$. The final pre-accelerator in the chain is the Super Proton Synchrotron (SPS) that pushes the protons to a final energy of $450\ GeV$ before they enter the LHC and are accelerated to their highest energy of $6.5\ TeV$ at which they collide at the four interaction sites [36].

3.2 ATLAS

ATLAS (A Toroidal LHC ApparatuS) is one of the two general purpose physics detectors located at the LHC [37]. As such, ATLAS investigates a wide variety of different physics topics. One of the most prominent topics in recent years relates to different processes involving the Higgs Boson following its observation in 2012. Other areas of active research were mentioned in the previous section.

The entire detector stands at 25 meters in diameter, 46 meters in length and weighs around 7000 tonnes. The instrumentation that makes up ATLAS is arranged in such a way that the overall shape resembles an onion, in that sub-detectors are placed in concentric cylinders around the interaction site. A model labeled with the various sub-detectors is shown in Figure 3.2.

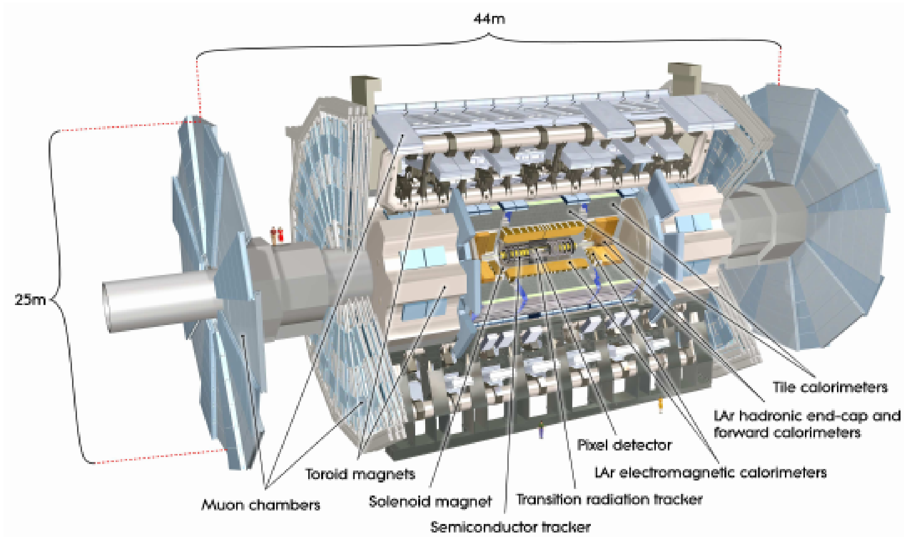

Figure 3.2: A model of the ATLAS detector labeled with the various sub-detectors as well the dimensions of the overall detector. [37].

The coordinate system for the ATLAS detector has the origin as the interaction point. The z-axis lies along the beam axis with the positive x-axis defined as pointing from the origin to the center of the LHC ring. The y-axis is defined as pointing towards the earth's surface. The azimuthal angle (ϕ) is defined as usual as the angle around the beam axis (z-axis) and the polar angle (θ) is the angle measured from the beam axis. A useful spatial coordinate that is commonly used instead of the polar angle is known as the pseudorapidity, η and is defined in terms of the polar angle:

$$\eta = -\ln(\tan(\theta/2)) \tag{3}$$

The reason that pseudorapidity is preferred over the polar angle is because particle production is roughly constant over η and differences in η are invariant under Lorentz boosts [38].

3.2.1 Inner Tracker

The inner tracker refers to the set of sub-detectors closest to the beam axis and is responsible for tracking charged particles by measuring the particle's charge and momentum while being immersed in a 2T magnetic field generated by a central solenoid. When a charged particle enters a magnetic field, the direction of curvature determines the charge, and the radius of curvature gives a measurement of momentum. To achieve the precise momentum measurements used for physics analyses, the inner tracker consists of three components: the pixel detectors, the semi-conductor tracker and the transition radiation tracker as shown in Figure 3.3 covering a region $|\eta| < 2.5$ with full 2π coverage in ϕ.

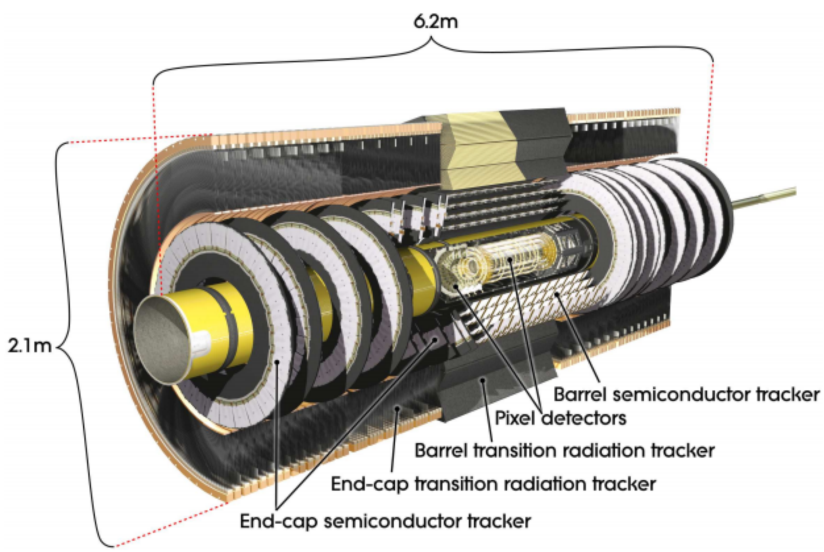

Figure 3.3: A cross-sectional view of the ATLAS inner detector, with each of the sub-detectors labeled. [37].

The innermost set of subdetectors are the pixel detectors and cover a radial distance from $50.5\ mm$ to $150\ mm$, offering high granularity tracking capabilities [39]. The basic building blocks of the pixel detector are modules consisting of silicon sensors. A single silicon pixel is 50 microns in the ϕ direction and 400 microns in z, a single module is made up of 46,080 individual silicon sensors. A silicon sensor consists of an array of bipolar diodes placed on a n-type bulk material, each sensor is made by combining a pn (positively-doped and negatively-doped) junction on either side of a wafer in order to create a depletion region. Reverse biasing the wafer increases the size of the depletion region; charge carriers produced by ionized particles passing through this depletion region can then be detected. As a result of the large number of pixels operating in this fashion, the transverse impact parameter resolution is 15 microns and the longitudinal track resolution is better than 1 micron in addition to offering 3D vertex reconstruction.

The next outer-most layer of sub-detectors after the pixel detectors is the semi-conductor tracker (SCT). The active regions of the detectors cover a radial distance from $299\ mm$ to $560\ mm$ and consist of 4088 silicon strip modules, which allows for a two dimensional position measurement [40]. The design of each silicon strip module is very simple, two planes of silicon act as the active region of the detector. In between these is a core sheet known as a baseboard providing both thermal and mechanical strength giving each module an overall length of $128\ mm$ (there are different dimensions for modules on the barrel and the endcap). On the barrel, each strip has a spatial resolution of 17 microns in the $r - \phi$ coordinate and 580 microns in the z coordinate.

The final layer of the inner detector is the transition radiation tracker (TRT) and consists of 298,034 straw tubes each with a diameter of $4\ mm$ covering a radial distance from $563\ mm$ to $1066\ mm$ [41]. A straw tube operates as a cylindrical drift chamber; a 31 micron diameter tungsten wire running along the central axis of each straw tube acts as the anode immersed in a gas mixture of Xe(0.7):CO_2(0.27):O_2(0.03). Charged particles passing through the tube would produce ionization that would then drift towards the anode wire generating a signal. The TRT also allows for electron identification by way of polypropylene fibres (barrel) and foils (endcap) dispersed between the straw tubes to measure transition radiation. These have higher energy signatures than ionized charges providing an easy solution for separating electrons from the sea of other charged particles [42].

3.2.2 Calorimeters

Calorimeters are devices that measure the energy of a particle passing through by collecting the energy of the secondary shower initiated by the incident particle. The ATLAS detector has two sampling calorimeters covering a range of $|\eta| < 4.9$ [37]: an electromagnetic calorimeter, and a hadronic calorimeter. Figure 3.4 shows a cross section of the ATLAS calorimetry system. Both ATLAS calorimeters are constructed as sampling calorimeters in which there are alternating layers of absorbing material (such as Lead) which produces the particle showers and active detector material collecting the energy. The other class of calorimeters are known as homogeneous calorimeters, in which there is only one type of material that performs both tasks of producing and measuring the signal.

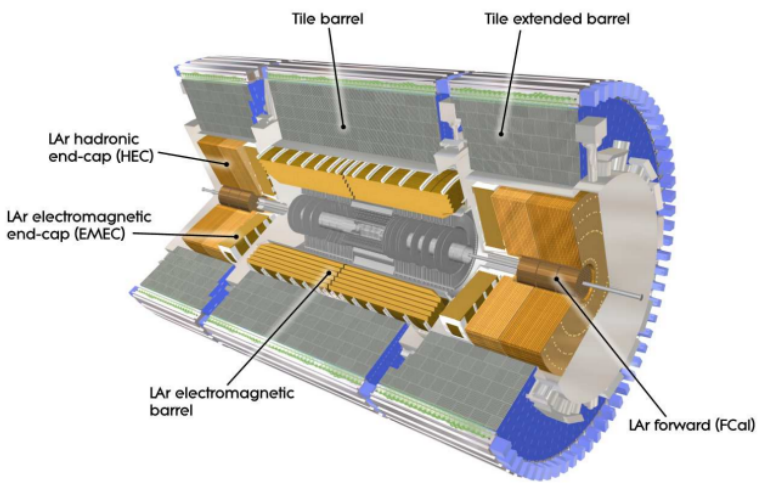

Figure 3.4: ATLAS contains two different sampling calorimeters, an electromagnetic calorimeter for electrons and photons, and a hadronic calorimeter for strongly interacting particles. [37].

The electromagnetic calorimeter (EM) is responsible for measuring the energy of charged particles such as electrons and covers the spatial range of $|\eta| < 3.2$ [43]. The EM calorimeter uses lead as its passive absorber and liquid Argon as its detection media kept in a liquid state by a crysotat. When a charged particle impacts a layer of lead and creates a particle shower, the secondary particles generate ionization in the liquid Argon layers that drift under high voltage to anode wires that then collect the charge. Since the amount of charge released by the ionization event is proportional to the energy, the energy of the primary particle can be deduced.

The Hadronic calorimeter (HCAL) is responsible for measuring the energy of strongly interacting particles and consists of three sections [37]. The tile calorimeter covers a region $|\eta| < 1.7$ and uses steel as the absorbing material and plastic scintillators as the active detector. The next section is the liquid-Argon hadronic end-cap calorimeter which uses liquid Argon as the detector medium interleaved with copper plates acting as the absorber and covers a region from $1.5 < |\eta| < 3.2$ overlapping slightly with the tile calorimeter. The final section that makes up the hadronic calorimeter is the liquid-Argon forward calorimeter, which in itself is made up of 3 modules; one module is made of copper optimized for electromagnetic interactions and the other two modules are made of tungsten optimized for hadronic interactions.

3.2.3 Muon System

The muon system and its upgrade in 2019 form the basis of much of the work described in this thesis. The current design consists of several sub-systems as shown in Figure 3.5 and is responsible for measuring the properties of muons (and other weakly interacting particles) [37]. Since muons interact relatively weakly, they will usually pass through the calorimeters undetected. Large barrel ($1.6 < |\eta| < 2.7$) and end-cap ($1.4 < |\eta| < 1.6$) magnets produce magnetic fields that bend the particles producing tracks. Tracks formed in the barrel region of the muon system are measured by three concentric cylinders of detectors, while those that are found in the end-cap are measured by three layers of detectors arranged in planes.

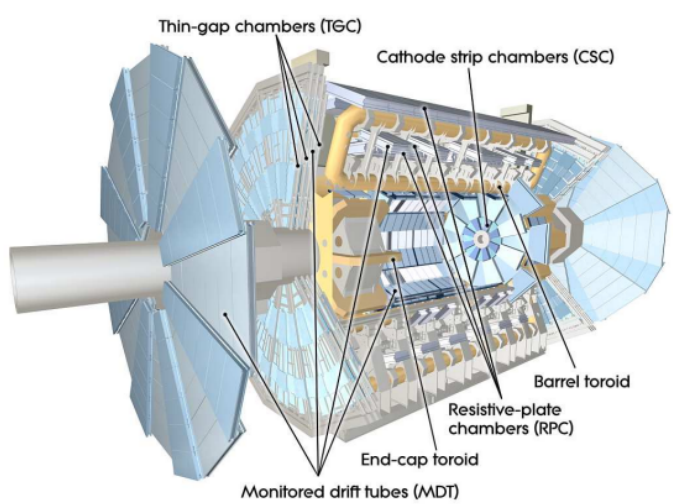

Figure 3.5: A cross sectional view of the ATLAS muon system, muons and other weakly interacting particles passing through the calorimeters are bent by toroidal magnets are measured by Monitored Drift Tubes (MDTs) and Cathode Strip Chambers (CSCs). [37].

Monitored Drift Tubes (MDTs) form the majority of the detectors covering a large portion of the η-range of the muon system, these function as cylindrical drift chambers allowing for precision measurements of the degree of curvature produced by the toroid magnets [37]. For areas that are exposed to high rates such as in high η ranges, Cathode Strip Chambers (CSCs) function as multi-wire proportional chambers, offering higher granularity. Finally, triggering and data filtering are performed by Resistive Plate Chambers (RPCs). RPCs consists of a gas gap sandwiched between two cathode planes (similar to planar gas detectors) divided into strips [23]. The division of the cathode plane into strips and the distribution of the signal on a cluster of strips allows for a quick measurement of the particle's momentum, this is turn allows for rapid decision-making capabilities on whether the data is meaningful or not.

3.2.4 Triggering and Data Acquisition

A dedicated trigger and data-filtering system is required for a number of reasons. The first reason is to select out potentially interesting events from the collection of uninteresting background events. Another reason is to reduce the rate of data arriving into the acquisition system, which will quickly become overwhelmed by the influx of data. A quick back of the envelope calculation reveals that for the 40 MHz bunch crossing rate and a single event with an approximate size of 25 MB, there would be approximately 1 petabytes worth of data every second. The ATLAS trigger and data acquisition (TDAQ) system decreases the data rate from 40 MHz to 200 Hz and an event size of 1.3 MB giving a data rate of approximately 300 MB/s [44].

The ATLAS TDAQ system is divided into three levels and filters data coming from the lower level triggers. The first level, L1, receives the initial influx of data at the nominal 40 MHz rate from the calorimeters and the muon system. Some of the interesting events that are selected by L1 include: jets, hadrons, tau leptons, electrons, photons as well as looking for missing transverse energy and momentum [45]. The operation of L1 begins with 256 trigger items, which are a set of programmed thresholds in the central trigger processor. Each trigger item contains a set of conditions for which events will be accepted. Furthermore, a pre-scale factor N can be specified for each trigger item to maximize the bandwidth available [46].

The next level of data filtering, L2, receives and refines the data from L1 applying more sophisticated algorithms [44]. It applies these algorithms within a certain Region of Interest in order to minimize computational power and time. The refinement process uses data with a higher granularity relative to L1 and employs measurements and constants obtained during calibration. The result is that the rate is further decreased from a maximum of 100 kHz to 3 kHz.

The final level of the trigger is the Event Filter (EF). The EF uses offline analysis algorithms along with a full set of constants reducing the rate down to the final value of 200 Hz [44]. In addition, the EF also classifies events based on a set of pre-determined event streams that are added to the final file structures.

3.3 New Small Wheel (NSW) Project

The current small wheel is the inner-most station on the end-caps forming one set of sub-detectors of the muon system. The current technology makes use of MDTs, CSCs and RPCs whose operation were briefly discussed in Section 3.2.3. However with the long shutdown scheduled for 2019 and 2020, the current small wheels will be replaced with new detector elements.

3.3.1 Motivation for Upgrade

Following the long shutdown and upgrade, the instantaneous luminosity will increase up to a factor of five above the the design luminosity of 10^{34} cm^{-2} s^{-1} allowing ATLAS to produce rarer events at an increased rate. However, the increased luminosity will also increase the muon trigger rate, quickly surpassing the readout capabilities of the current readout electronics. Furthermore, the current small wheel is susceptible to "fake" muons (fake rate of about 90%) [47]. Fake triggers occur when low energy particles are produced in the region between the small wheel and the big wheel (end-cap muon trigger) depicted in Figures 3.6 and 3.7. Simply raising the muon threshold will decrease the fake rate, but this will significantly reduce the signal acceptance as well.

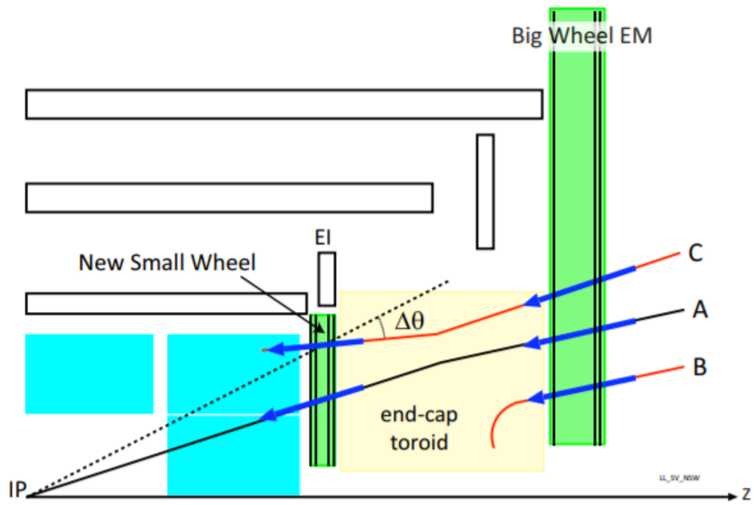

Figure 3.6: The current small wheel has a very high fake rate of 90%, muons produced in between the small wheel and the big wheel that have no tracks reconstructed back to the interaction point (IP) are still being triggered by the end-cap muon trigger. Tracks B and C are examples of fake muons with no tracks leading back to the interaction point and yet are still triggered by the big wheel trigger [47].

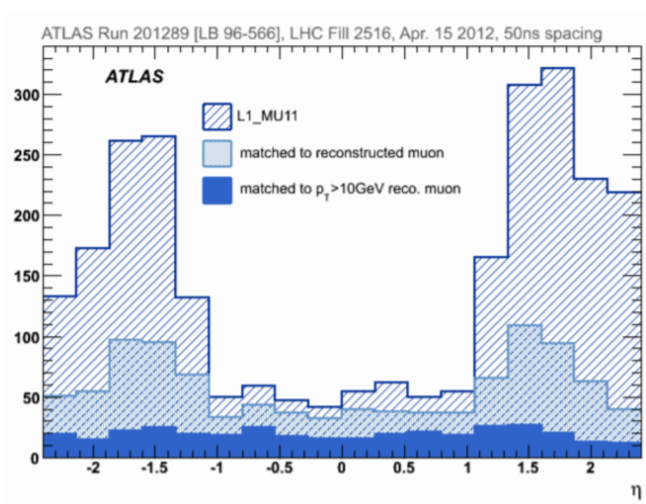

Figure 3.7: Distribution of the level 1 muon triggers in η compared with the offline reconstructed muon tracks with $p_T > 3\,GeV$ and reconstructed muons with $p_T > 10\,GeV$ that shows that an extremely large proportion of triggered events are not matched to reconstructed muons leading to the high fake rate characteristic of the current small wheel [48].

3.3.2 New Small Wheel Layout

The new small wheel (NSW) (shown in Figure 3.8) is divided into sectors, 8 large sectors, and 8 small sectors alternating around the circumference of the wheel. Each sector is further divided into an arrangement of quadruplets which are trapezoidal-shaped detectors arranged in two multilayers. Each multilayer consists of 4 layers of small-strip Thin Gap Chambers (sTGC) and 4 layers of Micro-Mesh Gaseous Structure (Micromegas) detectors (both of which will be discussed in later sections), therefore each sector of the NSW will contain 16 layers of detector planes.

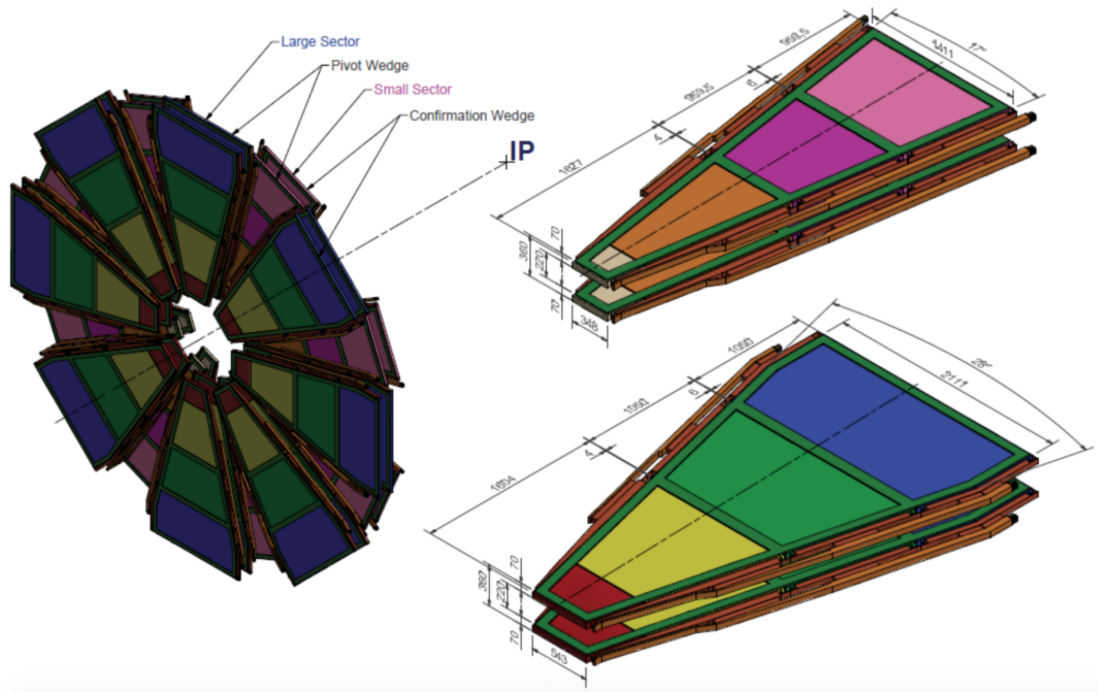

Figure 3.8: A schematic of the new small wheel and the small and large sectors partitioned into quadruplets [49].

The layers are arranged such that two Micromegas detectors are sandwiched between two sTGC detectors (sTGC-MM-MM-sTGC) so as to maximize the distance between sTGC detectors in order to improve angular resolution [50]. Furthermore, using eight planes of detectors per multilayer improves robustness, reliability and precision in an area of the detector that is exposed to a high influx of background events and radiation. Finally, the two detector types, the sTGC and the Micromegas, were chosen due to their compatibility; the sTGCs are capable of measuring a track resolution up 150 microns and the Micromegas will be used for triggering purposes along with the sTGCs [50].

3.3.3 Small-Strip Thin Gap Chambers

In its most basic form, the sTGC is a multi-wire proportional chamber (MWPC) operated in a high voltage regime. The MWPC was discussed in Section 2.4.3, and here only the most salient features of a MWPC will be reiterated. A MWPC contains a plane of equidistant anode wires immersed in a gas held at a potential difference. Charged particles passing through the gas create ionization that then drifts towards the nearest anode wire, generating a signal. The distribution of charge on adjacent wires gives an idea of the particle's path through the detector.

For the NSW project, each sTGC quadruplet consists of 4 independent sTGC gaps, referred to as gas gaps as shown in Figure 3.9, and makes up 4 of the 8 layers comprising a multilayer. The gas mixture that is used in this case is a CO_2(0.55):pentane(0.45) mixture. Each gas gap contains 3 different types of readout electrodes: pads, strips and wires. Each of the wires is made out of gold-plated tungsten and has a diameter of 50 microns and a pitch of $1.8\ mm$ and held at a potential of 2.9 kV [51]. The wires are arranged in groups, referred to as wires groups and provide one out of three spatial coordinates. Cathode planes sandwich the wire plane $1.4\ mm$ above and below. Behind one cathode plane are copper strips that run perpendicular to the wires and are spaced $3.2\ mm$ apart. Due to the large number of strips, they provide another spatial coordinate orthogonal to the wires with fine granularity. Finally, behind the other cathode plane are relatively large rectangular-shaped pads that are used to provide a 3-out-of-4 coincidence used for triggering purposes. In addition, pads are used to determine a subset of strips that a track may have passed through.

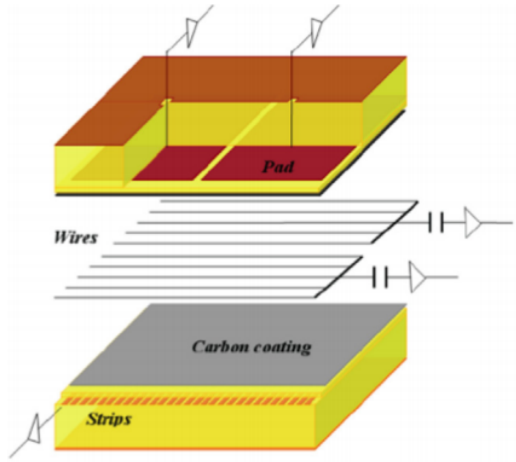

Figure 3.9: One of the 4 gaps of the sTGC quadruplet made up of strips, pads and wires [51].

3.3.4 Micro-mesh Gaseous Detectors

Micro-Mesh Gaseous Detectors or Micromegas are an advancement made upon the MWPC by the same inventors, Georges Charpak and Ioannis Giomataris in 1992 [52] with the original schematic shown in Figure 3.10. For Micromegas detectors, the wire plane characteristic of a MWPC is replaced by a fine mesh separating the gas volume in two. The Conversion gap is found above the mesh and is held at only a fraction of the electric field of the Amplification gap found below the mesh. Anode copper strips with pitch on the order of hundreds of microns are placed in the amplification gap. When a charged particle passes through the conversion gap and ionizes the gas, the positive ions drift towards the cathode while the electrons drift towards the mesh. When the electrons encounter the mesh, they experience a much larger electric field. They gain enough energy to generate secondary ionization events resulting in an avalanche of charge arriving at the anode strips.

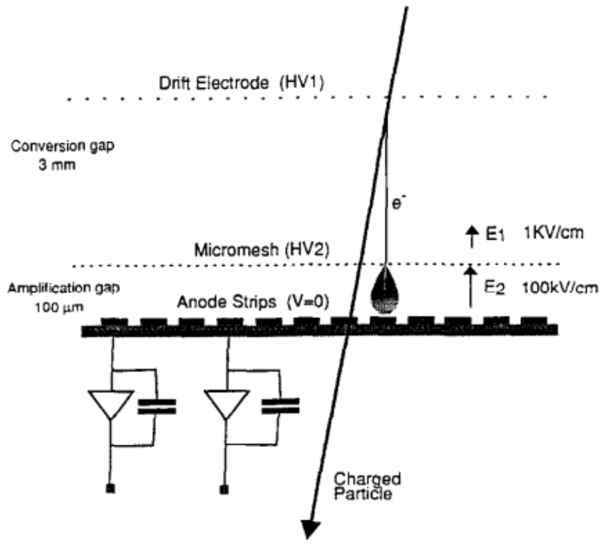

Figure 3.10: A schematic of a Micromegas, an improvement made upon the traditional MWPC whereby the wire plane is replaced by a mesh and the signal readout is done by copper strips [52].

The micromegas composing the NSW are very similar to the original design with a few differences as shown in Figure 3.11 (Left) [53]. First, the mesh is kept in position by 128 micron pillars that are configured into a grid on the readout strips. Second, in order to combat one of the main weaknesses of sparking that were characteristic of the original design, an insulator material as shown in Figure 3.11 (Right) is applied. Shorting produced by unwanted particles such as slow-moving alpha particles or debris in the detector can lead to damage to electronics and large dead times [50]. This resistive material ensures that the avalanche of charge is not directly impinging onto the anode strips but rather is capacitively coupled. This does decrease the height of the signal but allows for the application of higher potential differences and thus a higher gas amplification. Moreover, the original concept had the mesh held at a negative high potential relative to the grounded anode strips. The Micromegas produced for the NSW have the mesh grounded and the strips connected to a positive high voltage, again this is to prevent potential sparking [50].

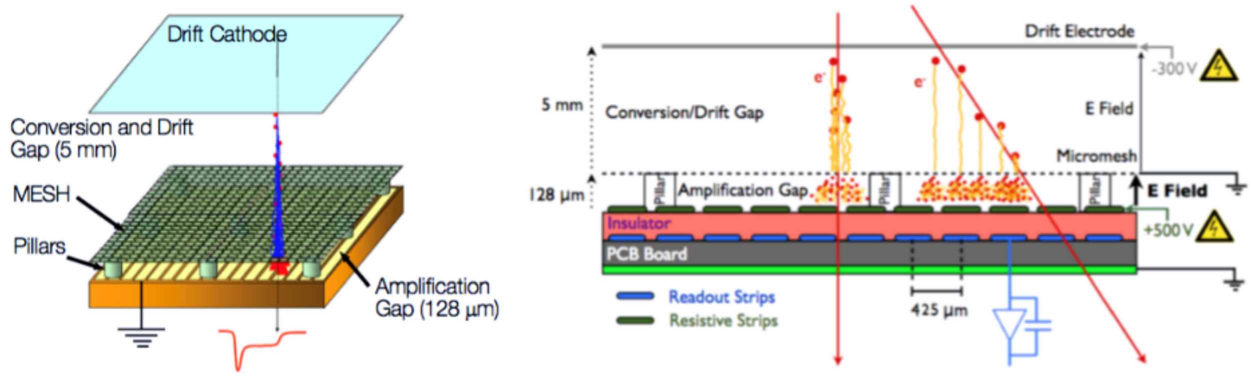

Figure 3.11: A schematic of a Micromegas used in the NSW (Left), a resistive coating is applied to the readout strips in order to prevent sparking produced by unwanted particles or debris that could damage the detector (Right) [54].

3.3.5 Canadian NSW Participation

Canada, along with four other countries that include Israel, Chile, China and Russia, participates in the construction and testing of sTGC quadruplets. The Canadian effort involves three institutions beginning with TRIUMF which constructs the individual cathode planes by delimiting the positions of the strips and the pads and spraying the planes with a graphite coating. The completed cathode planes are then shipped to Carleton University where the assembly of the four gas gaps takes place and where the wire groups are strung across the gaps. Finally, the completed quads are sent to McGill University where the majority of the testing takes place. It is worth mentioning that the shipping is done by land in order to maintain a climate controlled environment. If the quads were shipped by air, the extreme temperatures and pressures may cause residual gas in the layers to condense, damaging the quad. Testing of each quad at McGill is done using cosmic rays to test the readout of each strip, pad and wire. In addition, hit efficiency and spatial resolution measurements are conducted. Along with characterization of the front-end electronics, the efforts at McGill will form the majority of the remainder of the thesis. Upon completion of testing at McGill, the tested quads are shipped to CERN where they undergo further testing with test beams before they are assembled into the NSW and integrated into the ATLAS detector.

4 McGill sTGC Testing Lab

McGill's current role in the sTGC project is the testing of the QS3P production quadruplets; these are the outermost quadruplet on the small sectors. The "P" stands for pivot and is used to distinguish this quadruplet from another which has a "C" denomination standing for Confirm and is the other sTGC detector on the second multi-layer. This section will describe the set-up of the lab at McGill University containing the test bench, gas system, scintillators/PMTs, and the slow control. These systems operate together to perform a data-taking run.

4.1 Test Bench

The test bench, as shown in Figure 4.1, is an aluminum structure containing four removable shelves that are used to house the quadruplets. Since each quad sits directly below one another, this allows a maximum of four quads to be tested simultaneously. At the time of writing this thesis, only 1 quad (resting on the top shelf) can be tested at any one time due to the limited number of front-end boards (FEBs) available. The other three shelves contain various other pieces of support equipment. On the third shelf sits an early prototype of a sTGC quadruplet, this was used for gaining a basic understanding of the quadruplet and behaviour of FEBs prior to the arrival of the first production quads in the summer of 2018. Other support equipment includes the switch which acts as a hub for the various Ethernet signals and oscilloscopes for visualizing the signals. Finally, mounted on the right center aluminum post is the KC705; this is a vendor issued demonstration circuit board that houses a Xilinx Kintex 7 Field Programmable Gate Array that bridges the data collection system and the individual FEBs. Besides acting as the mechanical structure, the aluminum frame is also used for grounding purposes in order to protect the electrostatically sensitive front-end boards.

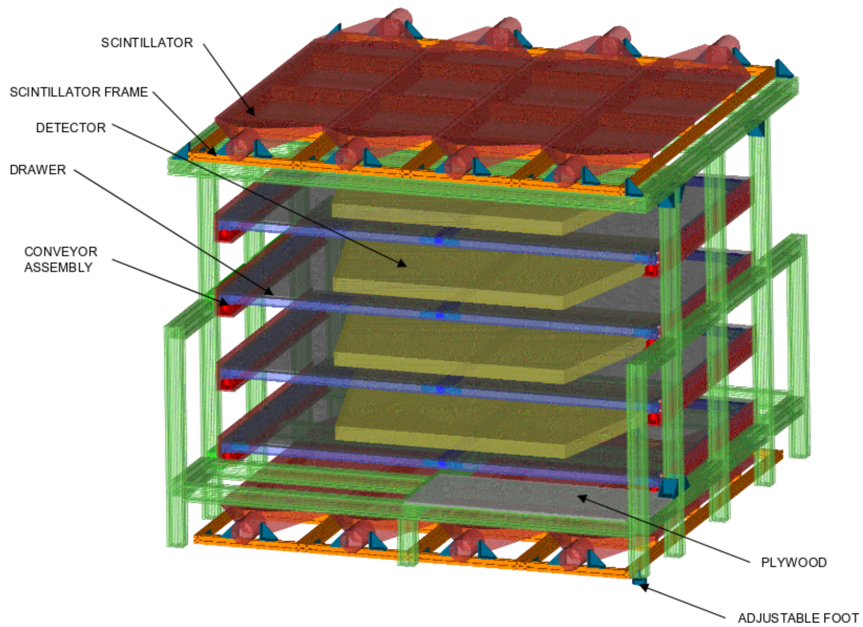

Figure 4.1: Picture of the test bench for the sTGC lab at McGill University, the production quad QS3P.4 sits on the top shelf surrounded by other pieces of support equipment [55].

4.2 Trigger System

A combination of 8 scintillators and 16 PMTs, as shown in red in Figure 4.1 and schematically depicted in Figure 4.2, are used as an external trigger fed into the data acquisition system. A trigger is defined as a particle that passes through the sTGC quad and all 4 shelves of the test bench within a time interval of 100 ns. To accomplish this, 2 groups of 4 plastic rectangular-shaped scintillators are placed above and below the test bench. When a particle passes through both sets of scintillators a coincidence signal can be recorded from the 16 PMTs and this is fed into the NIM logic crate.

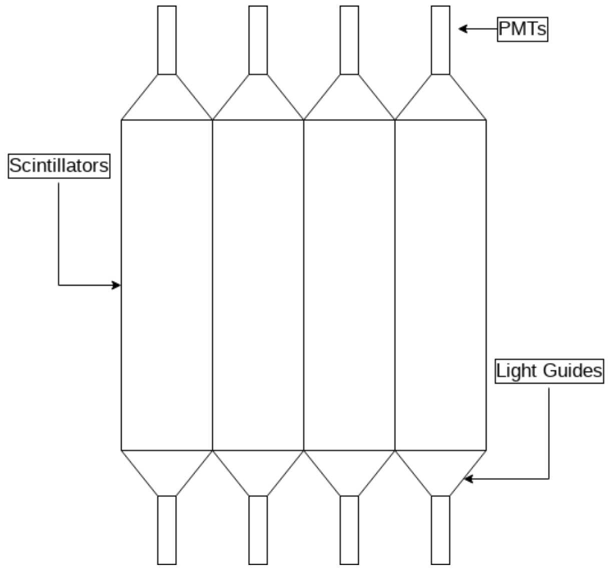

Figure 4.2: A series of 8 scintillators each attached with 2 PMTs are arranged above and below the test bench; a particle passing through both sets will produce a trigger signal.

A block diagram of the NIM logic circuit is shown in Figure 4.3, the first step is feeding each of the 16 PMT analog signals into a multi-channel discriminator that outputs a NIM digital signal once a set threshold is reached. Next, the output from each channel is fed into an eight-fold logical OR module that independently performs a logical OR operation of the top 8 PMTs and the bottom 8 PMTs resulting in two outputs. These two outputs are then fed into a logical AND module generating the NIM trigger signal, this NIM signal is widened into a 1 μs pulse using a gate generator before being sent to the timing and trigger controller (miniTTC) attached to the KC705. To reduce the trigger rate, the same gate generator produces 6 μs gaps between consecutive trigger pulses. Therefore, a trigger signal is only sent when a particle crosses both the top set and the bottom set of scintillators, yielding a final trigger rate of coincidental events of approximately 150 Hz. Other peripheral devices such as a counter are used to monitor the number of raw and coincidental events.

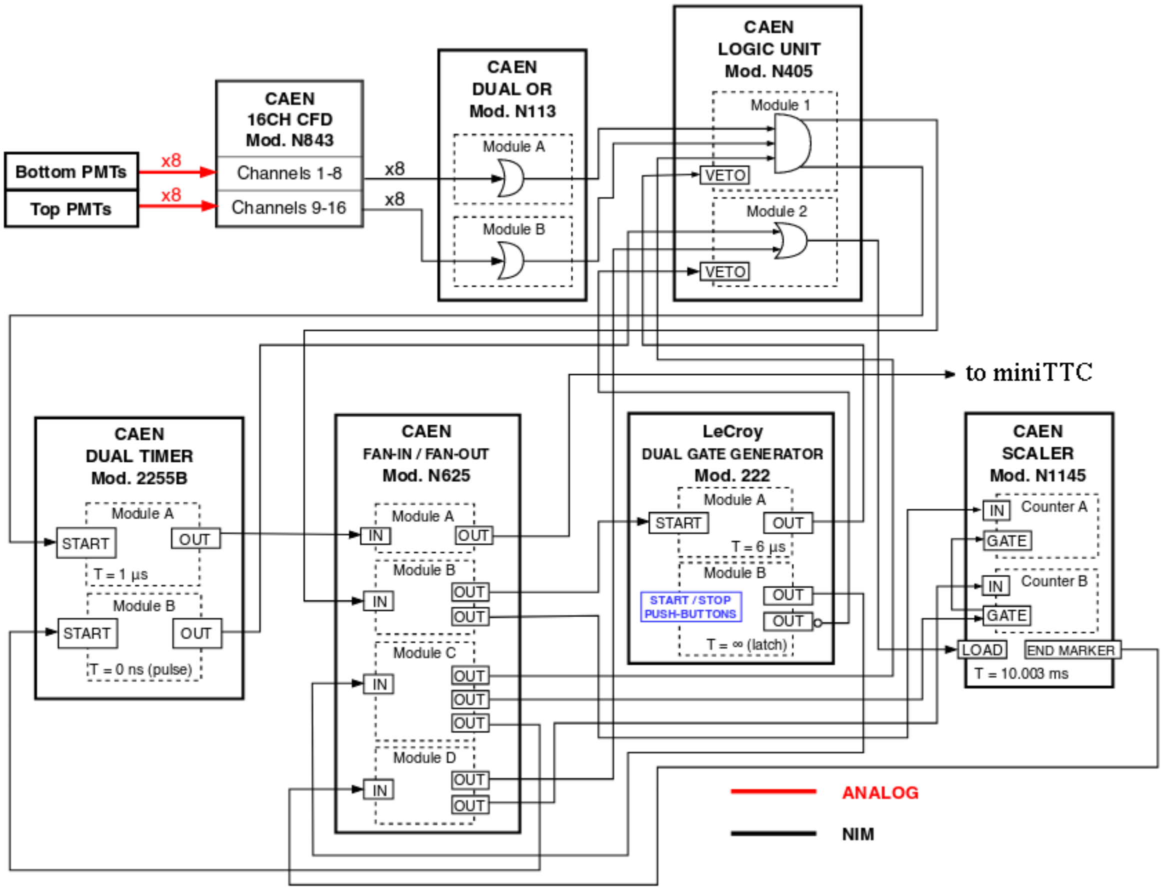

Figure 4.3: The NIM logic crate uses a series of discriminators, logical OR and logical AND modules to generate 1 μs wide NIM trigger. A gate generator produces a 6 μs veto in between consecutive trigger pulses [55].

4.3 Gas System

During a complete run, all four 4 gaps of a quad must be continuously supplied with a mixture of CO_2:pentane (55%:45% by volume). The choice of the gas mixture was made to absorb any photons produced during the ionization process. Photons generated in wire chambers are undesired because photons could initiate new avalanches on neighboring electrodes which worsens the spatial resolution. Therefore, pentane acts as a quenching gas in order to absorb excess photons [56]. To accomplish this, a custom gas system as shown in Figure 4.4 was designed at McGill to properly perform the mixing and delivery of the gas into the quad [57]. The gas system has the capability of delivering a constant rate of flow in 10 lines independently.

Figure 4.4: The three sides of the custom gas system designed for the McGill sTGC testing lab. The gas system mixes CO_2 and pentane into the proportions needed for proper operation of the sTGC quads. Left and Middle shows the bubblers, rotameters and manifold valves of the 10 independent lines. Right shows the solenoid valves and electronics for the data acquisition system [57].

Temperature control is used to create the 55:45 mixture of CO_2 and pentane. The mixing stand depicted in Figure 4.5, consists of a pentane mixing vessel, Peltier thermoelectric cooler and scale. Pure CO_2 contained in a gas cylinder is pumped through the mixing vessel containing liquid pentane creating a saturated CO_2:pentane mixture at room temperature but at a higher concentration than what is desired. The Peltier is cooled to 14.5°C so that the concentration of pentane drops to the desired 45% via condensation. The condensed pentane is then recycled by gravity back into the mixing vessel.

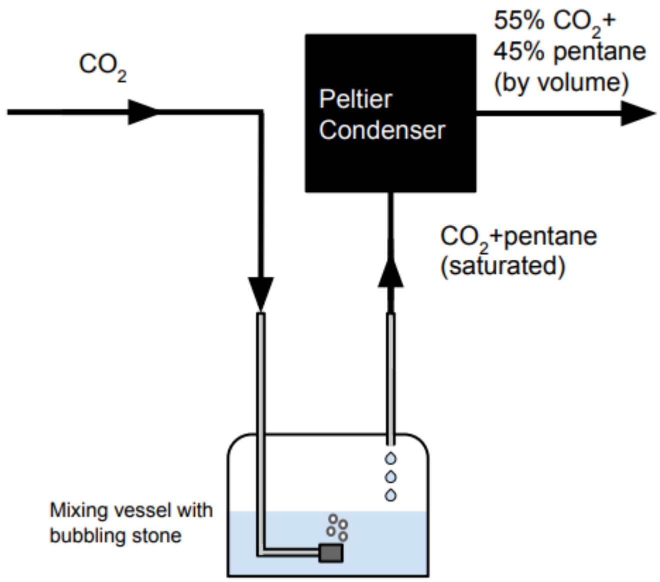

Figure 4.5: A schematic diagram of the mixing apparatus, CO_2 bubbled through liquid pentane in a mixing vessel creates a saturated mixture of CO_2:pentane, the percentage of pentane is lowered to a final percentage of 45% by volume through condensation using a Peltier cooling block. [57].

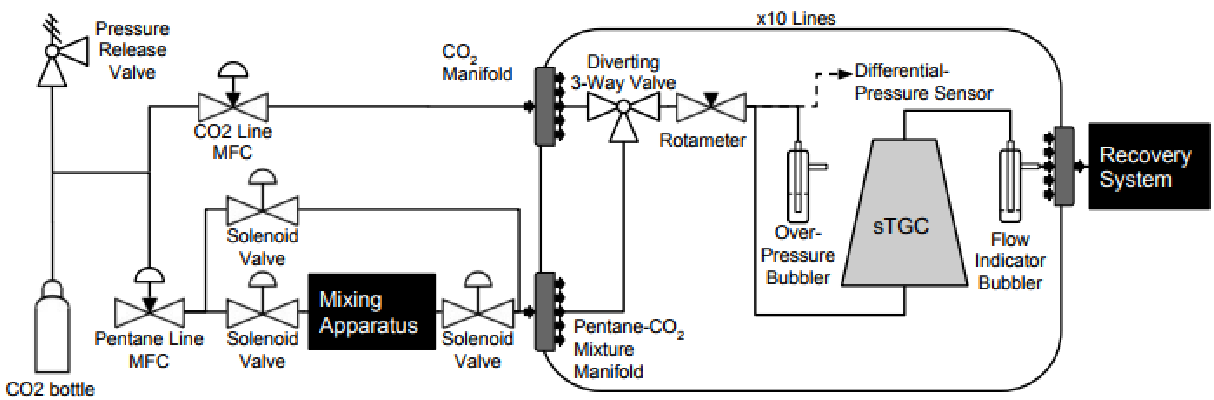

Figure 4.6: A complete schematic of the full gas system. The gas flows from left to right, with a flow rate controlled by two MFCs (one for pentane and one for CO_2) and several different valves and manifolds before entering the 4 gas gaps of the sTGC quad. A recovery system collects the gas output downstream of the sTGC quad [57].

A complete schematic of the gas system is shown in Figure 4.6, the gas mixture which now contains the correct proportions of CO_2 and pentane flows into a manifold which splits the gas flow into each individual gas line. Before finally entering the quadruplet, the relative flow in each line is controlled via a rotameter that is used to equalize the flow in each line. Precise control of the flow of CO_2 and pentane mixture is achieved using

Mass Flow Controllers (MFC) controlled by the user through the state machine which will be described in the following section. There are two sets of bubblers, one located upstream of the sTGC quad and one downstream of the quad. Over-pressure bubblers filled with oil upstream of the sTGC protect against overpressure which could exert stress on the button supports in an individual gas gap. These are also used as indicators of back-flow if oil is observed in the inner tube submerged in the oil. The second set of bubblers, downstream from the quad are used as visual indicators of flow. Upon exiting the quad, the gas is directed to a recovery system consisting of another gas vessel stored in a nearby refrigerator.

Solenoid valves are implemented throughout the gas system for precautionary reasons and are monitored using temperature sensors. These valves operate by running a current through an internal solenoid generating either a closing or opening motion upon activation depending on the dormant state of the specific valve (normally open vs. normally closed). In normal operations, the solenoids are in a state where during gas operation, gas is allowed to flow freely throughout the system and into the quad. In case of a potential malfunction, emergency situations (examples of such scenarios are provided in the next section), or sensor mis-communication, the solenoid valves switch states diverting the gas to an exhaust entering a so-called CO_2 bypass state which will be discussed in the following section.

Safety is a built-in feature of the gas system [57], and as such, beyond recognizing that the valves are in the correct orientation, very little user intervention is required. Beyond the standard WHMIS protocols, safety procedures in the lab are geared towards understanding the different states that the gas system can be in and the implications of each of these states.

4.4 Slow Control/State Machine

The slow control system is used to monitor all of the sensors in and around the gas system as well as enabling/disabling the high and low voltages. The values of the sensors are programmed in LabView and updated in real time. The slow control and data acquisition system in general have a number of other purposes besides monitoring, including changing states and providing safety precautions.

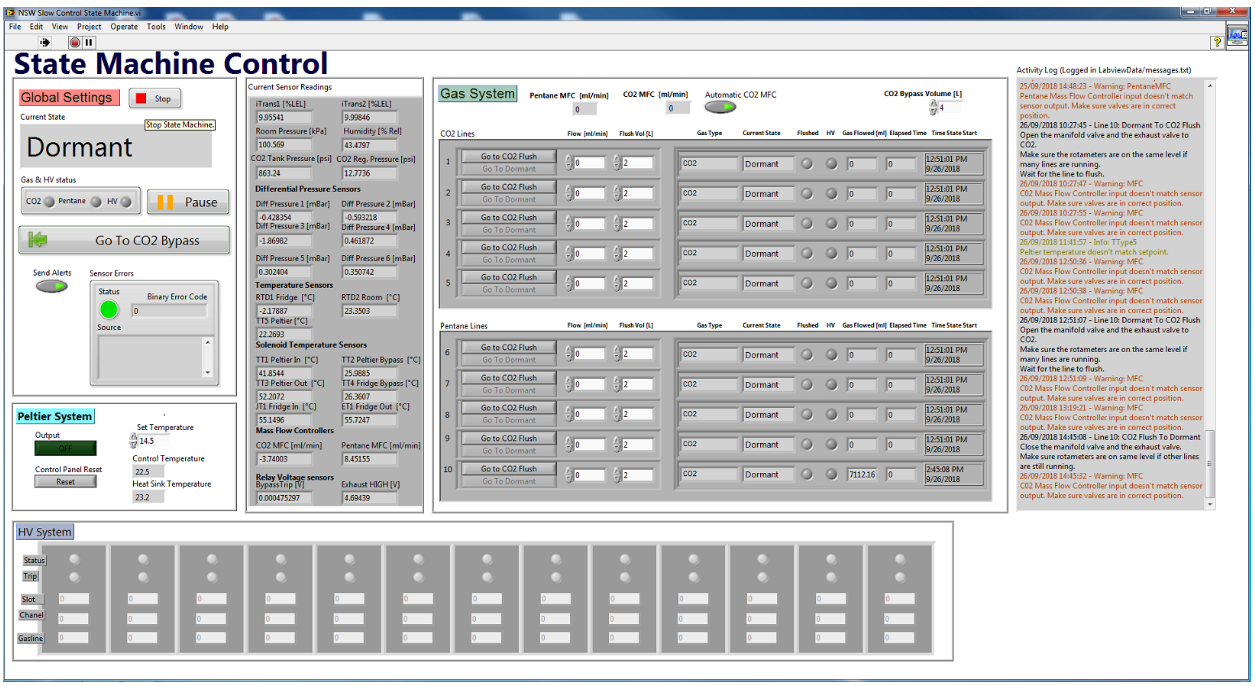

Figure 4.7: A screenshot of the main state machine control screen which monitors the slow control data and allows transitions from a dormant state to gas operation.

The state machine is the main screen shown in Figure 4.7, for driving the gas system to different states. On the far left is the panel showing the current state of the gas system. Below that is a panel showing the status of the temperature controller. In the center-left panel are the various sensors connected to the slow control. These include the iTrans gas sniffers, which are used to detect gas levels in the environment and can force a CO_2 bypass state if a certain threshold is reached. Other sensors include the differential pressure sensors, temperature sensors for the fridge and the solenoid valves and the MFC values. The main central panel displays the current state for each of 10 gas lines indicating the flow rate, and allows the user to change the state of each line independently. Along the bottom is the state for each of the high voltage lines. Finally, the far right panel contains a history of errors and warnings.

The gas system is predominantly in the so-called dormant state. In this state, there is no gas flowing and the state machine simply collects the different sensor inputs. In order to begin an actual data-taking run the gas system must first enter the CO_2 flush state. Here, pure CO_2 flows into the gas gap to flush the gap of any impurities or any residual pentane remaining after previous runs. The CO_2 flow rate is often set at 100 mL/min. CO_2 flush occurs for at least two volume changes (at test beam sites, the quad is flushed for 5 or more volume changes). Following this, one can finally transition to a gas operation state where the CO_2-pentane mixture flows through the gaps normally at 40 mL/min and high voltage can be enabled to begin taking cosmic ray data.

Along with monitoring slow control data, any errors and warnings are also indicated. These are used to indicate whether the system needs to enter a bypass state for safety reasons. A CO_2 bypass state is characterized by a switching of the solenoid valves to divert the gas to an exhaust. A bypass state might be entered for any number of reasons including: mismatch between MFC and monitored data, the iTrans displaying an abnormal value, or if there is a sudden power outage. This is to ensure that the gas system enters a safe state if there is no one present in the lab and requires manual intervention to return to a "normal" operating state.

The other systems needed to perform a full run are the high and low voltage supplies which are routed to a CAEN power crate and are also operated via LabView. The high voltage module is used to power the 16 PMTs which operate at around 1.5 kV, as well as the 4 high voltage lines for the quad which are each ramped up to a final voltage of 2.9 kV. The low voltage module supplies the 8 front-end boards with 8 V each. To prevent damage to the boards, the user also sets a current threshold. Any devices surpassing their set current threshold will cause a current trip shutting off power to that device.

During the learning phase, the background knowledge needed to operate each of these systems was gained. This allowed testing of the production boards beginning in July 2018 to proceed much more smoothly. The prior knowledge enabled the setup to be brought online (and offline) with much more ease as more familiarity with the system was established.

5 QS3P.4 Set-Up

This section will cover the set-up process of the quad and the various pieces of hardware used for data collection. This includes the KC705 data-acquisition (minDAQ) board and the 4 pad front-end boards (pFEBS) and 4 strip front-end boards (sFEBs) and the different application specific integrated circuits (ASICs) found on the board. Each of these pieces of hardware will be described in this section. The characterization of the miniDAQ system forms the majority of the work presented in this thesis. There will also be a brief discussion on the data format for a general data-taking run.

5.1 QS3P Production Quad

The QS3P.4 is the name given to the 4th iteration of the outermost pivot quad on a small sector of the NSW. As part of the Canadian efforts, the cathode planes are first produced and tested at TRIUMF and then are sent to Carleton for wiring and assembly. Finally, the completed quads are sent to McGill where the efficiency and resolution are measured. The first of the QS3P production quads that will actually be assembled into the NSW only began arriving at McGill in the summer of 2018. The QS3P is illustrated in Figure 5.1, has dimensions approximately $1.5m \times 1m \times 0.1m$ and contains 3 different types of electrodes. Pads of which there are 24 on layers 1 and 2, and 39 on layers 3 and 4 provide a localized region to be read out and is used to provide a 3-out-of-4 layer coincidence. The localized region determined by the pads is used to select a subset of strips of which there are 307 strips on each of the four layers to be read out and is used to provide the radial coordinate. Finally wire groups of which there are 37 on layer 1 and 38 on the remaining 3 layers measure the ionized charge and provide a measurement of the remaining coordinate. A more detailed schematic showing the geometry of the three electrode types can be found in Appendix C.

The data from the three different electrode types are fed into Front end boards (FEBs) containing application specific integrated circuits (ASIC). The FEBS are connected to the adapter boards via GFZ connectors which is a rectangular grid containing an array of very fine electronic pinouts each attached to very small spring. Each of the 4 gas gaps are effectively independent and thus each requires one pFEB and one sFEB resulting in a total of 4 pFEBS and 4 sFEBS required for the entire quad. Each gas gap must also be supplied by its own gas line and HV line as well.

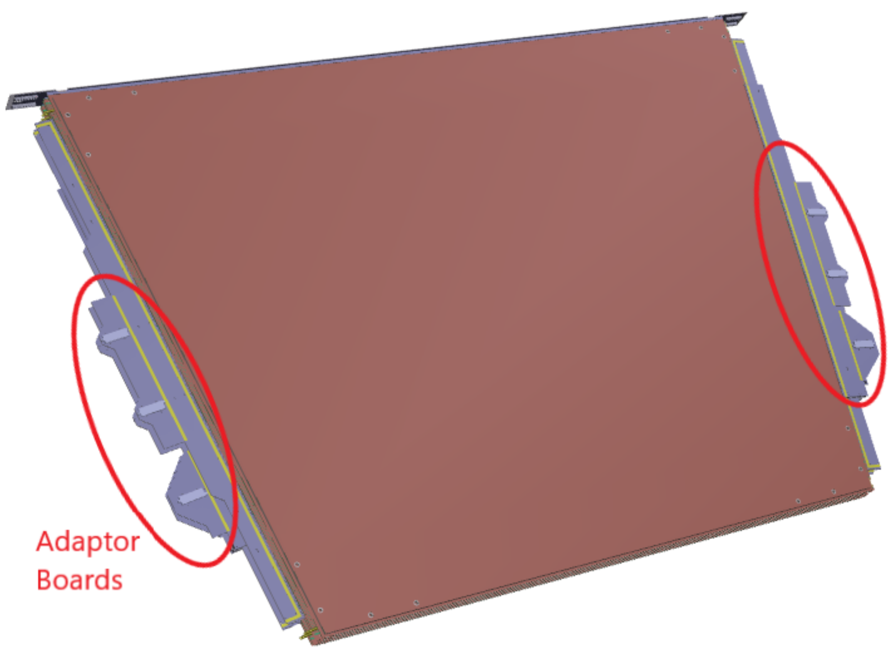

Figure 5.1: A technical drawing of the QS3P production quad, whose testing is the primary focus of the McGill sTGC lab. The positions of the adapter boards where FEBs are attached are indicated. The lighter rectangles on the adapter boards indicate the positions of the GFZ connectors. Each of the sFEBS requires two GFZ connectors, and each pFEB requires 1.

5.2 Readout Electronics

The readout electronics consists of the sFEBS, the pFEBs and the KC705. The KC705 shown in Figure 5.2 is a field-programmable gate array (FPGA) which is an integrated circuit containing a large array of programmable logic blocks. The KC705 (and specifically FPGAs) was chosen over an ASIC due to the reduced cost and flexibility when it came to updating applications. The KC705 bridges the 8 FEBs connected by Twinax cables; a Twinax cable is similar to a coaxial cable but with two inner conductors instead of one. The Twinax cables are connected through the mSAS mezzanine card which contains one elink (female Twinax port) for each of the 8 FEBs. The mSAS also allows for a trigger and timing control (miniTTC) module (shown in Figure 5.3) containing a LEMO slot for an external NIM trigger signal output from the NIM logic crate discussed in Section 4.2.

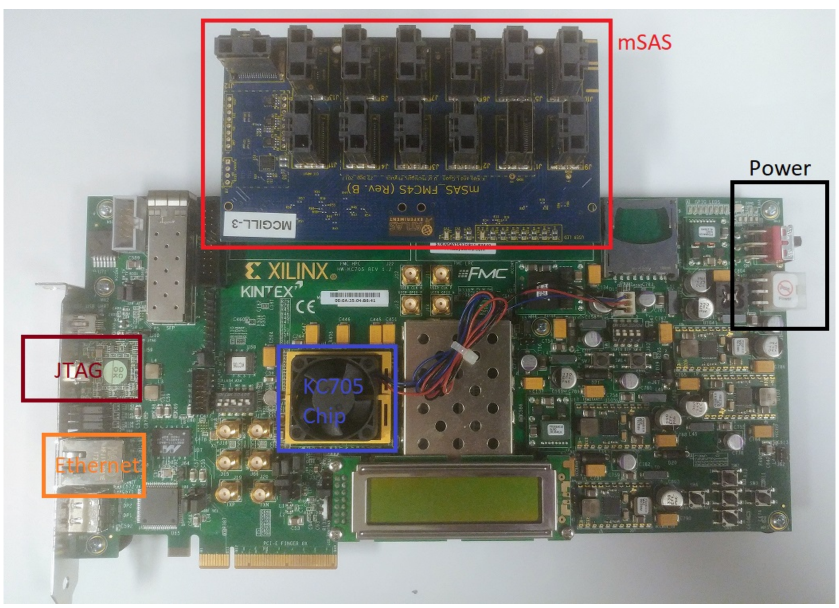

Figure 5.2: The KC705 FPGA is used to collect the readout from all 8 FEBs attached via Twinax cables to the mSAS mezzanine board. Firmware is loaded using a miniHDMI cable through the JTAG port. Communication with the DAQ computer is conducted using an ethernet cable.

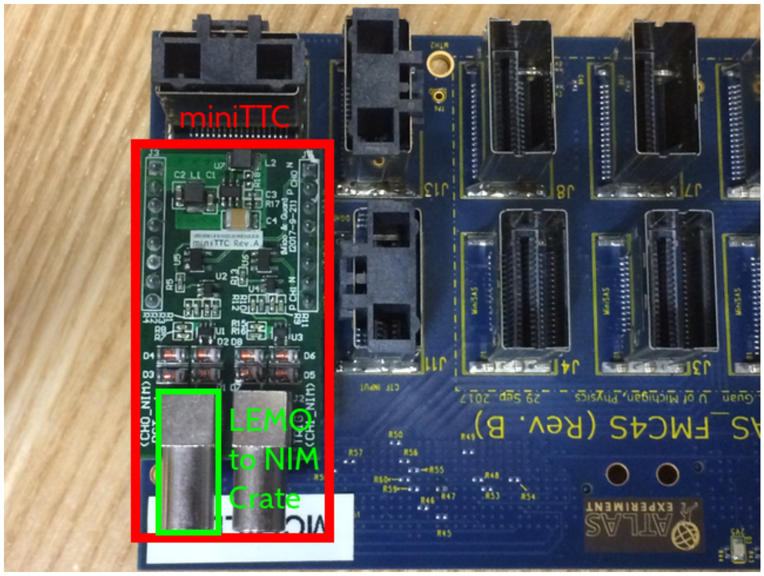

Figure 5.3: The miniTTC is responsible for providing trigger signals to each of the FEBs. The trigger signal processed by the NIM logic crate is fed into the miniTTC via LEMO cable.

The FEBs contain a number of different ASICs, but the main workhorse on the FEBs is the VMM3, an integrated chip that is currently in its most developed state having gone through 2 prior iterations. The chip was designed specifically for this project and is used in both the sTGCs and micromegas. The chips are indicated in red in Figures 5.4, 5.5. Each of the 4 pFEBS contains 3 VMM3 chips (of which 2 are physically connected) and each of the 4 sFEBs contains 8 VMM3 chips (of which 5 are physically connected). Due to the number of computations performed by the VMMs, the FEBs need to be properly cooled. This is especially important for the sFEBS because of the larger number of VMMs. Therefore, copper heat sinks are attached to the FEASTs of each sFEB board using thermally conductive sticky tack. The FEASTs are modules responsible for analog power supply, and act as DC-DC converters that transform one voltage level to another. These regions were identified using an infrared camera as regions of higher temperature. Resistance-temperature detectors (RTDs) attached to the underside of each FEAST continuously monitor the temperature. In addition, fans placed on the test bench are used to further cool the boards.

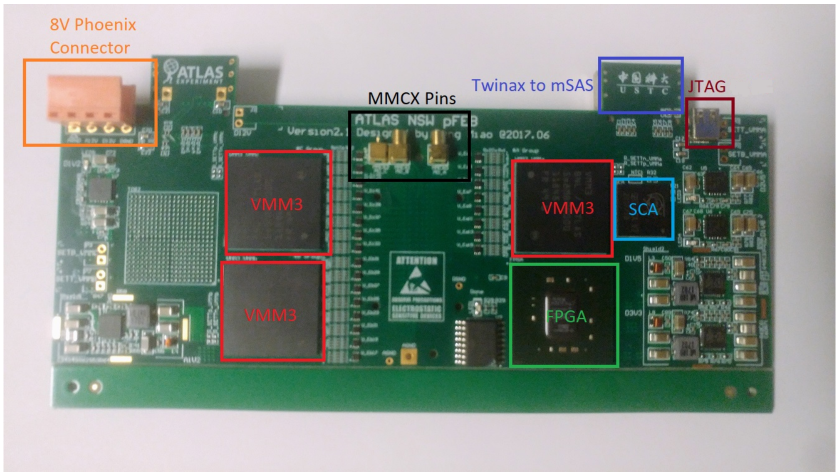

Figure 5.4: The pad front end boards contain three VMM3 ASICs that are used to read out wires and pads. Only two out of three VMMs are ever used since there are less than 64 wires or pads for any one layer. The slow-control adapter (SCA) is used to deliver configurations to each of the VMMs. The board is powered by an 8V phoenix connector and communicates with the KC705 system via a Twinax cable. The MMCX ports (labeled in black) are used to connect to an oscilloscope and are used in tests requiring visualization of the signal.

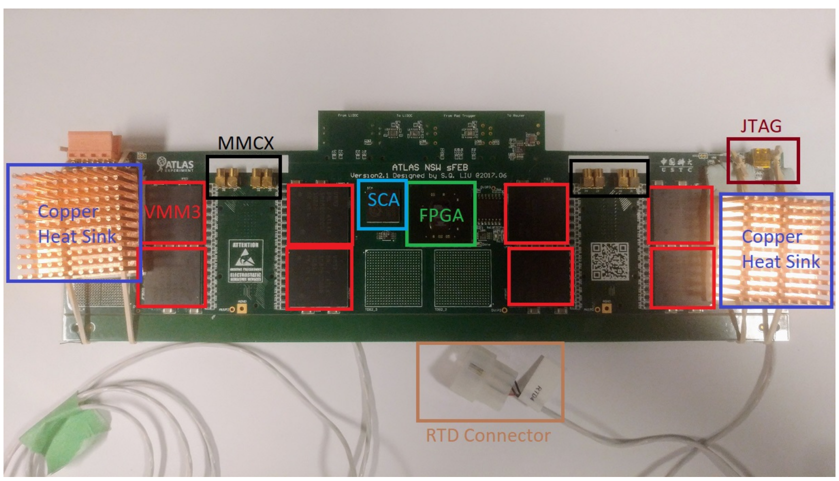

Figure 5.5: The strip front-end boards have similar design to that of the pFEBs and contain the same ASICs. There are 8 VMMs instead of 3 in order to read out the ∼300 strips on the quad. The sFEB is more prone to high temperatures that would damage the board if there is no cooling. Copper heat sinks are attached to passively cool the device with RTDs mounted to monitor the temperatures.

The complete electronic set up is shown diagrammatically in Figure 5.6. Each FEB is connected to its respective elink on the mSAS via a Twinax cable. The KC705 is attached via ethernet to the switch that acts as a hub for incoming and outgoing ethernet signals. Also connected to the switch is the oscilloscope and the miniDAQ PC, which contains the readout software.

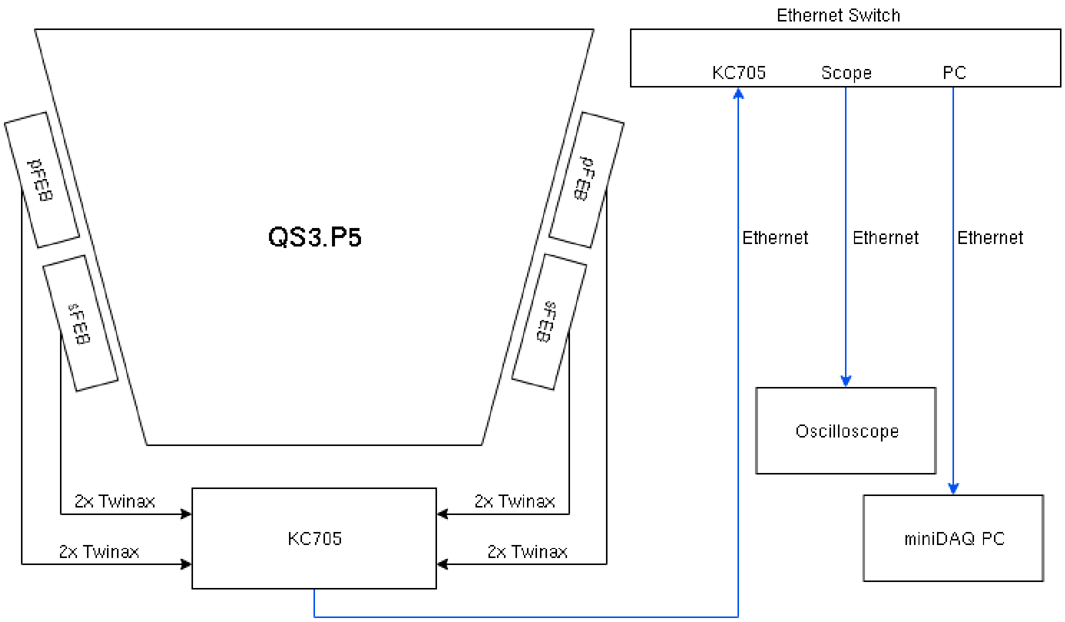

Figure 5.6: A schematic of the wiring and connections of the miniDAQ system with the quad, FEBs, KC705 and DAQ computer.

The VMM3 was designed at Brookhaven National Lab and contains 64 identical read-out channels and has a self-contained amplifier and discriminator for digitization [58]. A test capacitor on each channel allows for test pulses with a user defined height to be sent to any of the 64 channels; this function is used to perform many of the measurements in this thesis. The scope trace of a typical pulse is shown in Figure 5.7. The read out software allows the user to control the properties of the test pulse such as the height [DAC], gain [mv/fC] and peak time [ns].

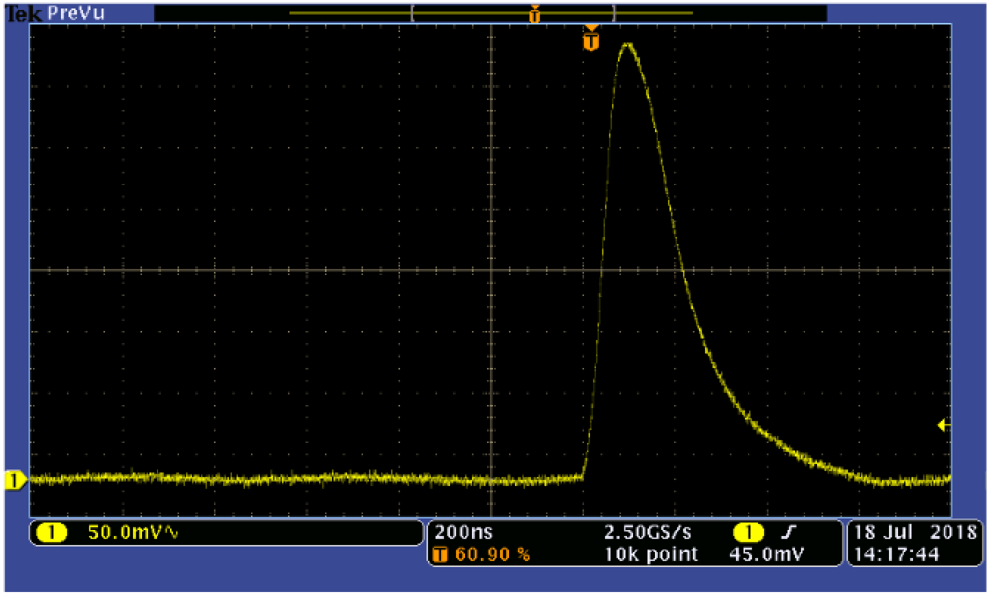

Figure 5.7: Scope trace of a typical test pulse.

Despite having a capacity of 64 channels, only a subset of channels is used to record data. The other channels are "masked" to reduce cross-talk noise; masking a channel prevents data from being written out from that channel. Unmasked channels are read out in continuous mode allowing for nearly deadtime-less output. In this mode, a maximum rate of 4 MHz can be handled and routed to an analogue-to-digital converter (ADC) returning a 10-bit digital signal. The signal acceptance is set by a 10-bit digital-to-analogue converter (DAC) threshold and is set by the user for each VMM. A further 5-bits of "trimming" can be applied to each channel to equalize the threshold to account for minor discrepancies from channel-to-channel. Finally, the VMM3 facilitates neighbour triggering, this means that channels that are not explicitly triggered can still be read out. This functionality is especially important for pedestal studies that will be discussed in a later section.

Another important ASIC found on the FEBs is the slow control adapter (SCA). This ASIC is responsible for distributing control and monitoring signals to the front end electronics. Each VMM is configured using settings stored in an xml file and includes settings for thresholds, test pulses, and settings for pulse shape configuration. These files are modified during the calibration steps in order to hard-code optimal threshold and trim values.

5.3 Readout Software

The miniDAQ readout software[2] was written by Liang Guan and Siyuan Sun[3] and is used to monitor and interact with the readout electronics. The main page of the GUI is shown in Figure 5.8, allows the user to begin and end a data-taking run as well as monitoring the number of triggered events. This page also allows the user to initiate communication with the KC705 and the FEBs, and send configurations to the boards.

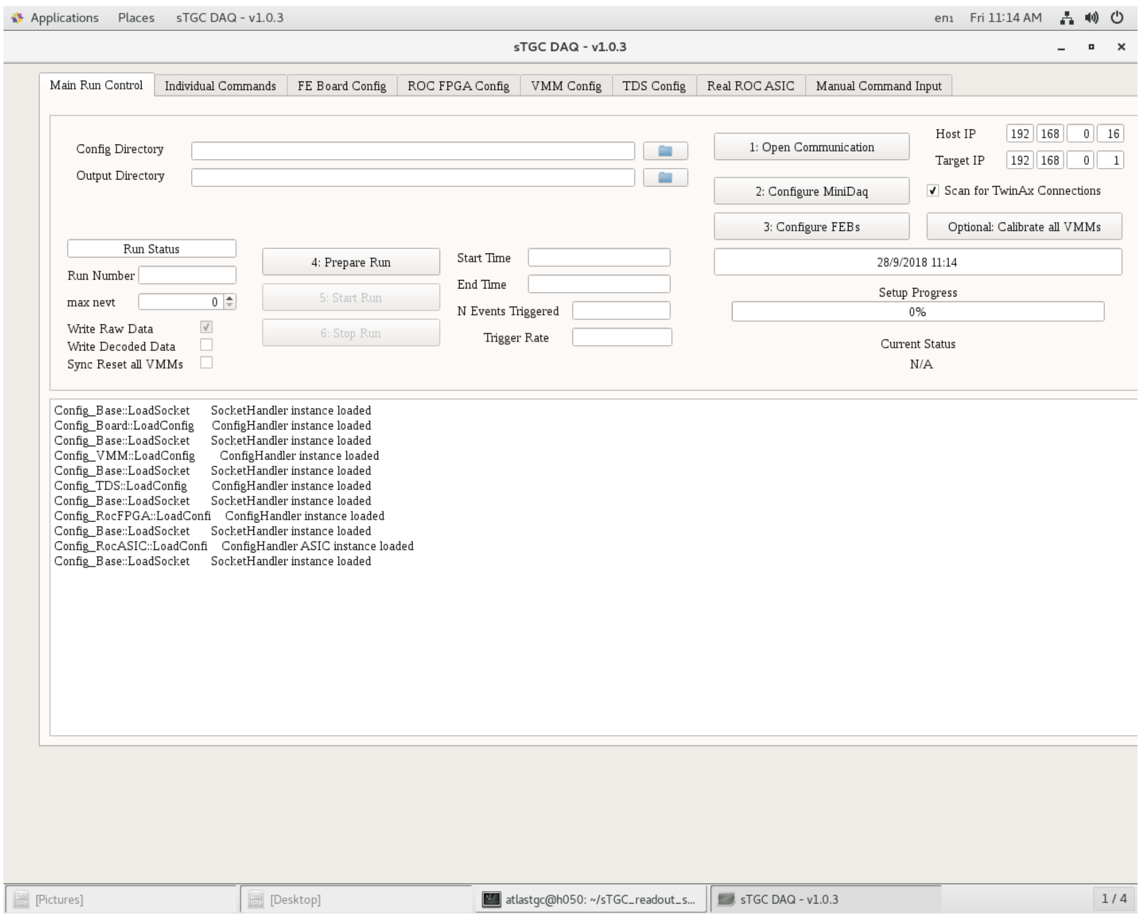

Figure 5.8: The main run control screen of the sTGC readout software gives the user the option of starting/stopping a run.

From here, one can navigate to one of the other tabs for configuring the FEBs. Perhaps the most important tab is the VMM Config tab, which contains settings for controlling the

[2] STGC Readout Software Gitlab: `https://gitlab.cern.ch/ssun/sTGC_readout_sw`

[3] University of Michigan

characteristics of the test pulse, such as the height and the threshold set in units of digital DAC counts. The VMM Channel Registers tab also allows the user to configure the VMMs by enabling and disabling certain channels as shown in Figure 5.9, here any channel with a green square in the last column is masked and no data is read out from that channel. Here one can also see the individual trim values that have been applied (how these values were set will be discussed in a later section). This is also the screen from which test pulses can be activated by enabling the test capacitor for that specific channel. On the right, there are also various buttons that automate various calibration steps, such as scanning the baselines and optimizing trim values.

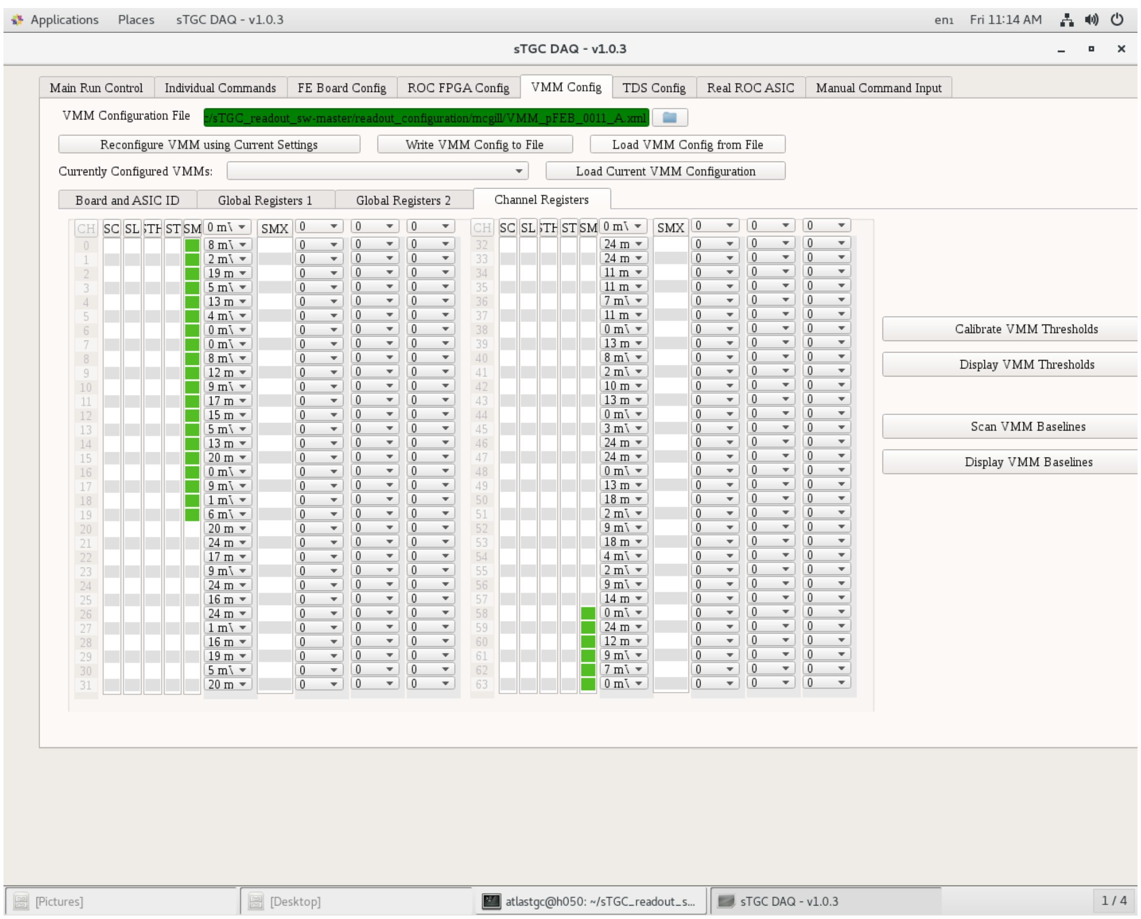

Figure 5.9: The channel registers page allows the user to control the VMMs on a channel-by-channel basis by masking/unmasking certain channels for readout.

5.4 Data Format

The miniDAQ system records hits of particles with sufficiently high energy (surpassing the threshold set by the user). The data for the strips are recorded by the sFEBs. The wires and the pads are recorded by pFEBs into binary format. A decoder written by the same authors of the readout software accepts these binary files and converts it into a user-friendly root file. This root file contains a number of useful monitor histograms. The first set of histograms is a channel-by-channel hit map that shows the number of hits per channel. Other useful histograms are pdo, tdo and bcid (defined below) distributions for each channel. The root file contains a TTree with the following branches:

- m_tdo: Time detector output; the time between the detection of an event above threshold and the external trigger
- m_pdo: Peak detector output; a 10-bit number proportional to the charge deposited in a specific channel
- m_chan: Contains the channel number that recorded an event
- m_vmm_id: Contains the VMM identity of the event
- m_elink_id: Contains the elink on the mSAS that the board is connected to
- m_bcid: Bunch crossing id; a number related to the clock cycle of the LHC (25 ns)

5.5 Data Preparation

The first step in data preparation is to calibrate the FEBs and optimize the settings on a channel-by channel basis. One of the most important steps is to set a digital threshold value, and this forms the basis of this section. A threshold that is too large drastically reduces the number of acceptable events leading to low efficiency. On the other hand, a threshold that is too low results in too many events triggered in the noise. Therefore, it is necessary to carefully set the threshold in order to reduce noise and maximize efficiency. In addition, a scan for dead channels is performed to identify any defective or erratic channels. Both of these measurements were performed by the author and explained in detail below.

5.5.1 FEB Calibration

This section will detail the step-wise procedure for calibrating the boards. Fortunately, the sTGC readout software has a built-in functionality that prepares most of the calibration data. The preparation of this data into plots and interpretation is performed by the author. Before beginning, a few key definitions are needed:

- **Threshold:** A 12-bit digital DAC number that corresponds to an analog value that is the minimum above which a signal will be accepted.
- **Baseline:** Analog value of the amplifier circuit output when there are no input signals, either from cosmic rays or test pulses.
- **Pedestal:** Digital DAC count readout by DAQ system on a channel when there are no input signals.

The first step is to measure the baseline for each channel, the purpose of measuring the baseline is that it provides an estimate of the analog value of the minimum DAC threshold that should be set for each VMM. The baseline is intrinsically an analog value approximately equal to 180 mV, but this analog value is output as a 12-bit digital number by the SCA ADC. The SCA has already been pre-calibrated such that this 12-bit number is mapped to a voltage between 0V and 1V. Therefore the linear relationship between an ADC count and a voltage value can be quantified as follows:

$$V = \frac{ADC}{2^{12}} \rightarrow \frac{ADC}{4.096}\,[mV] \tag{4}$$

When there are no input signals, the distribution of the baseline for each channel takes the shape of a Gaussian. An example of the baseline distribution for a single channel is shown in Figure 5.10. In order to extract the baseline value, a Gaussian fit is applied and the mean is taken as the baseline value. The standard deviation of the Gaussian is taken as the error on the baseline value. This is then converted to a mV value using equation 4 above.

It is necessary to expand upon the use of the standard deviation as the error on the mean. The use of the standard deviation was predicated on the fact that the ADC has some inherent non-linearity, and as a result systematic error attributed to it. These systematic errors should be proportional to the resolution of the ADC (i.e. the least significant bit). It should also be mentioned that in the process of fitting each individual Gaussian-like distribution, there was an associated error on the mean. The more correct error analysis would have used these errors as the error bars on the linear fits, however these were not taken into account as the chi-square values of the linear fits were extremely large. Therefore, the standard deviation was used in order to achieve a better chi-square value on the linear fit.

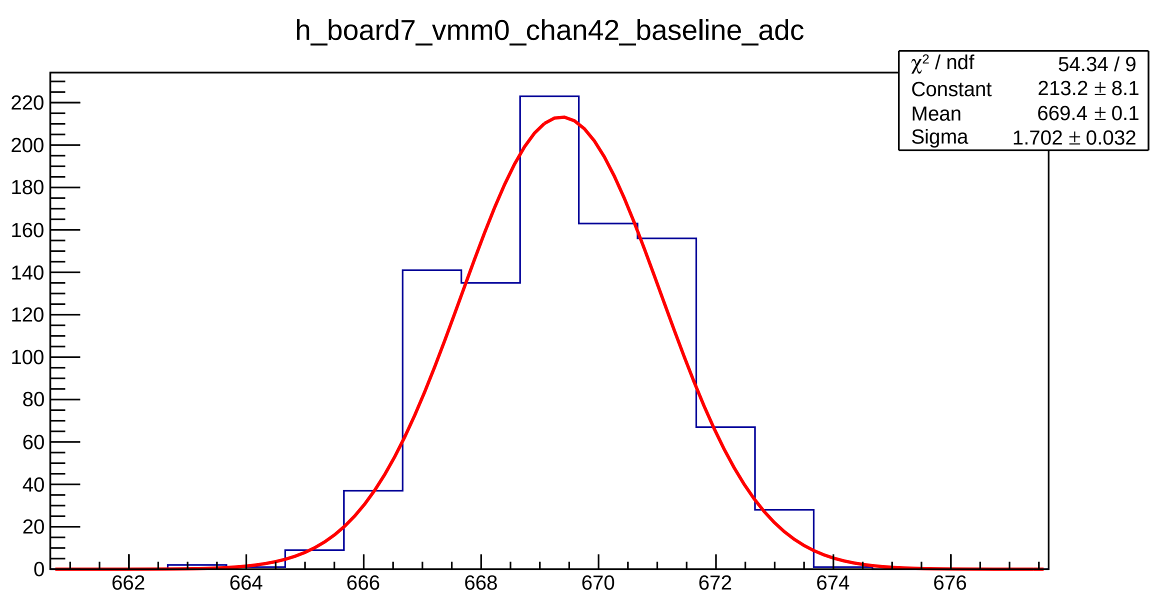

Figure 5.10: The baseline for each channel is extracted from the mean of a fitted Gaussian.

This process is repeated in order to obtain baselines for all 64 channels, Figure 5.11 shows the baselines for the 3 VMMs on a pFEB, and Figure 5.12 shows the baselines for the 8 VMMs on a sFEB. As expected, the majority of the points are clustered around 180 mV, however there is an observable variation on a channel-by-channel basis. Furthermore, there are some VMMs with lower baselines, for these VMMs the thresholds will be set slightly lower. Finally, there are some graphs which have outlying points, these are attributed to channels with poor fit results.

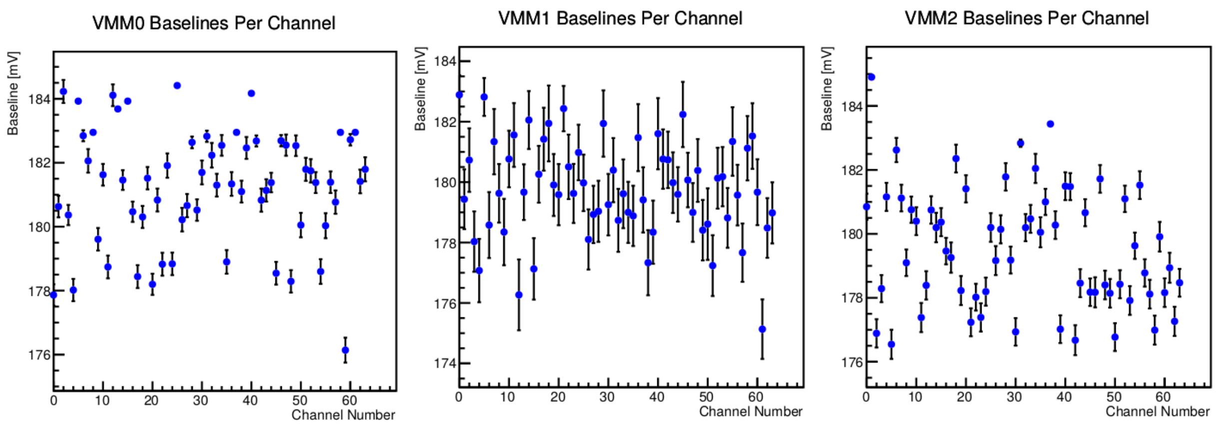

Figure 5.11: The baseline for the 3 VMMs on a pFEB.

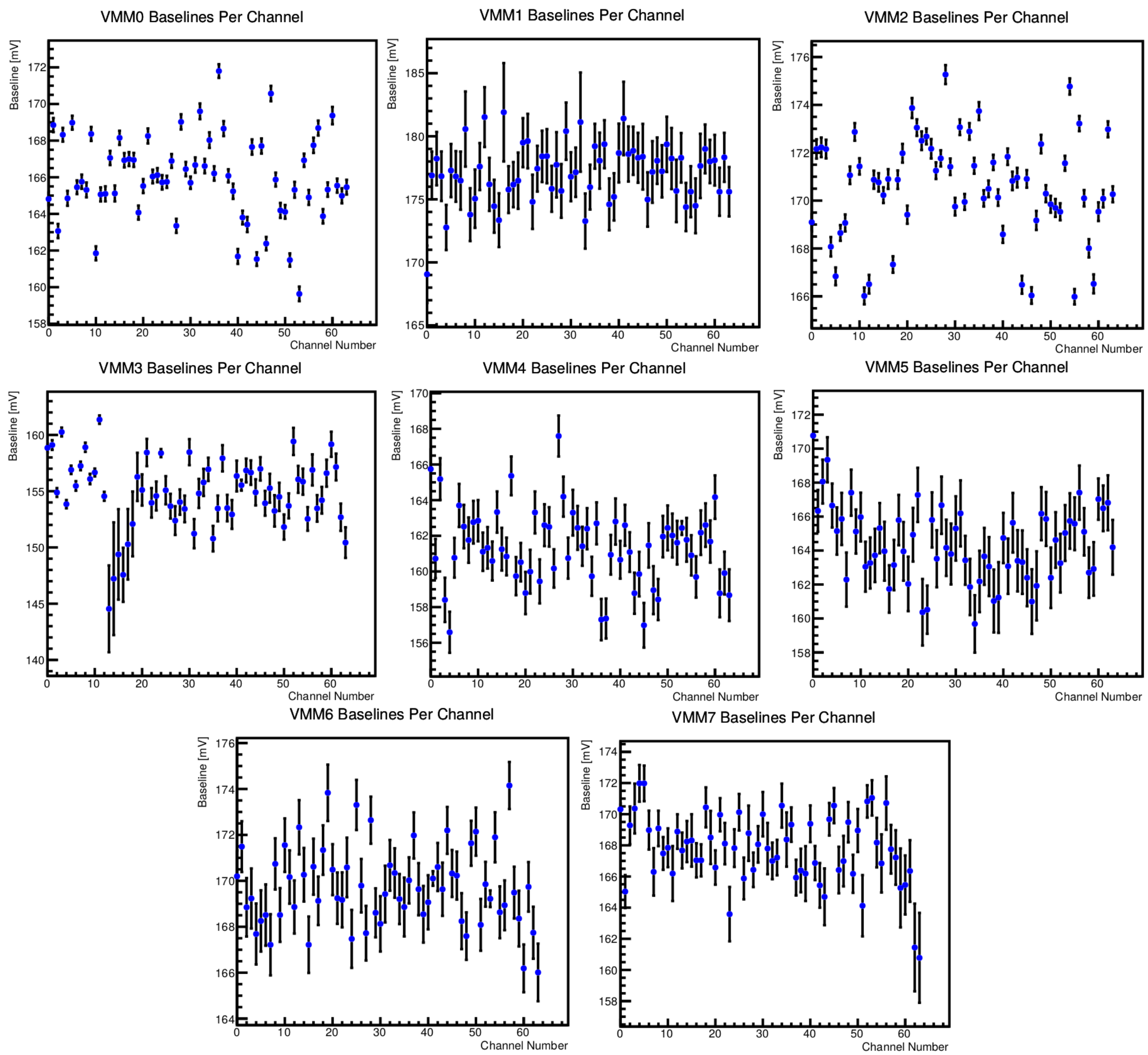

Figure 5.12: The baselines for the 8 VMMs on an sFEB.

In the process of producing the data used for these plots, the software also determines the optimal threshold trimming bit for each channel. A global threshold value is set for all 64 channels on a VMM, however due to differences between channels, there may be slight differences in the analog threshold value. Therefore an analog trim value (a mV value) is applied to each channel to account for these differences and equalize thresholds.

After the trim values for each channel are determined, the next step is to determine the calibration plot that allows us to convert a threshold value in mV to a digital DAC value accepted by the software. Again the software generates the data used for producing these calibration plots. During the global calibration step, the software sets progressively higher threshold values starting from a DAC value of 100 and increasing in steps of 20 counts until 480 counts. For each step, the mV value is extracted using the same procedure for the baselines, by fitting a Gaussian and extracting the mean as the threshold in DAC counts and dividing by 2^{12}. Figure 5.13 shows four plots at threshold values 100, 200, 300 and 400.

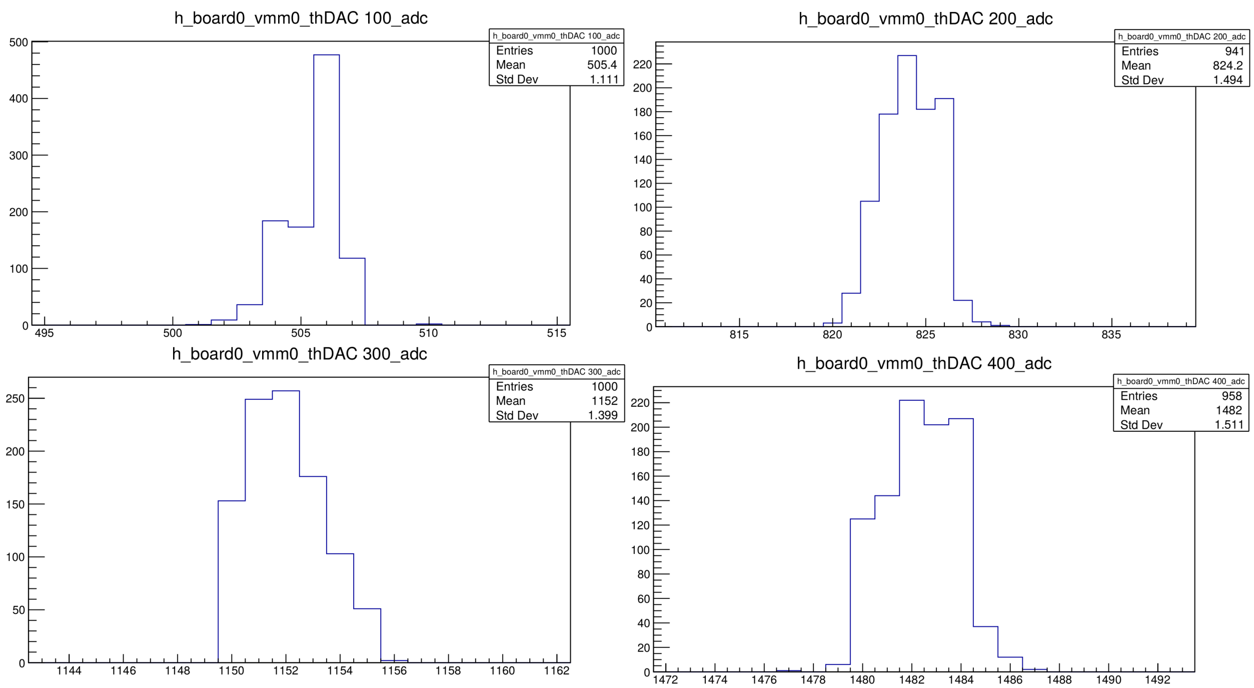

Figure 5.13: The software steps up from a threshold in DAC counts from 100 to 480, the mV value is extracted in order to produce calibration plots from mV to DAC.

Using the mV value corresponding to each threshold DAC value, one can produce a linear fit relating the threshold in mV to the threshold in DAC counts. Each mV also has an associated error which, as in the baseline plots, is the width of the Gaussian fit. Figure 5.14 shows the linear fits for the 3 VMMs on a pFEB and Figure 5.15 shows the linear fits for the 8 VMMs on an sFEB. Again there are occasional points where the Gaussian fit failed, and this is attributed to some graphs displaying double peaks. Ignoring these erratic points, it is evident that a linear fit works well for describing the relationship between mV and DAC, as expected.

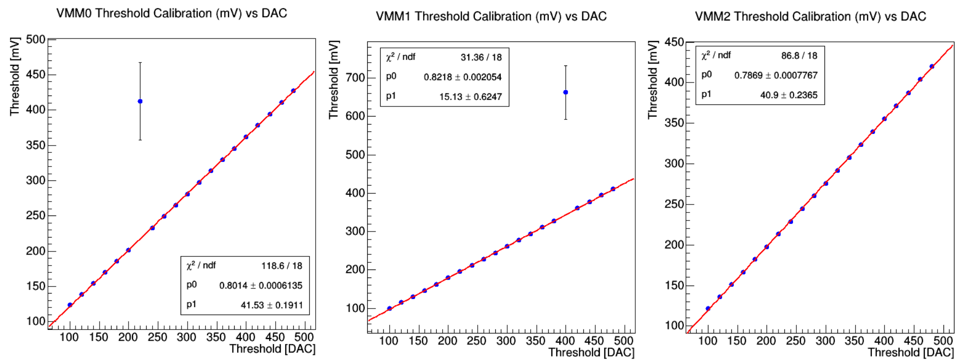

Figure 5.14: The linear relationship between the threshold in mV and the threshold in digital DAC counts. These correspond to the 3 VMMs on a pFEB.

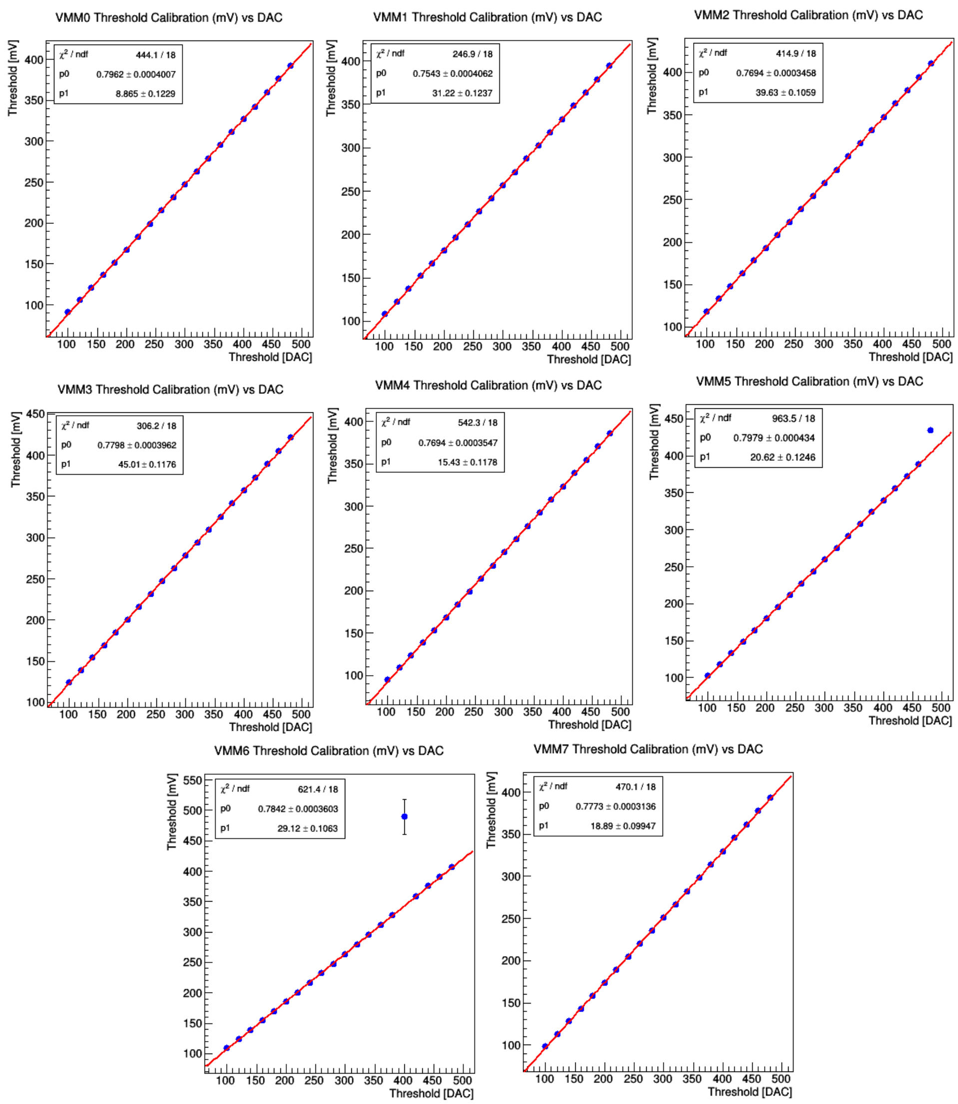

Figure 5.15: The linear relationship between the threshold in mV and the threshold in digital DAC counts. These correspond to the 8 VMMs on a sFEB.

The baseline plots and the threshold plots provide two important pieces of information necessary for setting a global threshold value. The final measurement that needs to be made is a noise measurement for each of the pad channels. To perform these measurements, the channel monitor feature of the readout software is used along with a Tektronix oscilloscope to measure the RMS value around the baseline value. Noise measurements are conducted for each of the 4 layers because each layer may have a different level of noise. For example, Figure 5.16 (Left) shows the noise level for the 24 pads attached to gas layer 1, which has an approximate noise level of 2-3 mV. In contrast, Figure 5.16 (Right) shows the noise level for the 39 pads attached to layer 3, which shows a much higher noise value of approximately 8-9 mV. For VMM channels that are physically unconnected to a pad or a wire (or masked), the RMS is measured to be approximately $\leq 1\ mV$.

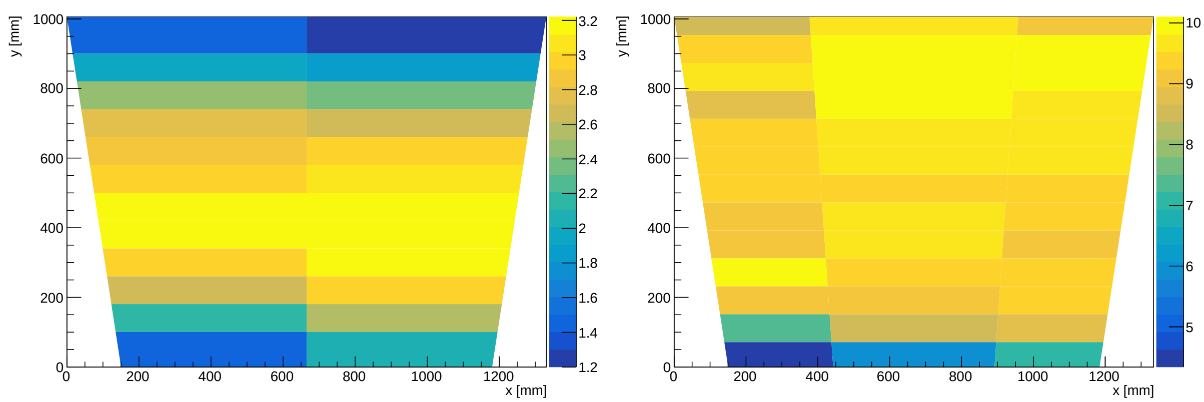

Figure 5.16: Comparing the noise levels (in mV) for each of the 24 pads on Layer 1 (left) and 39 pads on Layer 3 (right). There are apparent differences in noise between pads on the same layer, as well as differences between layers as well.

The noise could arise from a number of different sources and a great deal of effort has been expended to reduce noise wherever possible. For example, sources of noise that have been identified include the KC705, the fans used for cooling, as well as the various electronic devices scattered around the lab. Moreover, different sources for grounding are also potential sources of noise. It has also been observed that when there are multiple FEBs powered on that the noise increases significantly.

Using these noise measurements for each layer, a threshold value is set such that the noise is excluded as much as possible while maintaining minimal degradation of the signal. Using the baseline values for each VMM, the desired threshold value is calculated as follows, where th is the threshold in mV, bl is the baseline value in mV, and δ_{RMS} is the average RMS noise value in mV as measured by the oscilloscope for each layer:

$$th = bl + 3 \times \delta_{RMS} \tag{5}$$

This gives us a threshold value in mV, however it is necessary to convert to a DAC count that is accepted by the readout software. To accomplish this, the parameters of the linear fit between mV and DAC are used to convert from mV to DAC counts. Doing this for each VMM allows for a threshold value to be set.

5.5.2 Dead Channel Scan

During test runs using cosmic rays, it has been observed that certain channels display zero counts. It is necessary to determine whether these faulty channels are an intrinsic problem of the electronics in the board, poor connectivity with the GFZ connectors, or potential physical issues with the quad itself. A scan for these so-called dead channels is performed with the test pulser capability of the VMM3. Any channels that are found to be dead are purely electronic. Furthermore, these are compared with the hit maps using actual cosmic rays and any discrepancies are noted as due to other factors not linked to electronics. An example of hit maps taken during an actual data-taking run using cosmic rays is shown in Appendix A.

Using the test pulser capability of the VMMs, test pulses are enabled for all 64 channels on all of the VMMs. Any channels with zero events are recorded as a dead channel. The results are recorded in a text file and are incorporated into the cosmic analysis software. The results of a dead channel scan for the 3 VMMs on a pFEB are shown in Figure 5.17, and for the 8 VMMs on an sFEB are shown in Figure 5.18. The horizontal axis shows the VMM number, the vertical axis is the channel number, and the color map shows the number of hits. Dead channels can clearly be seen as white squares on the plots where no hits were recorded.

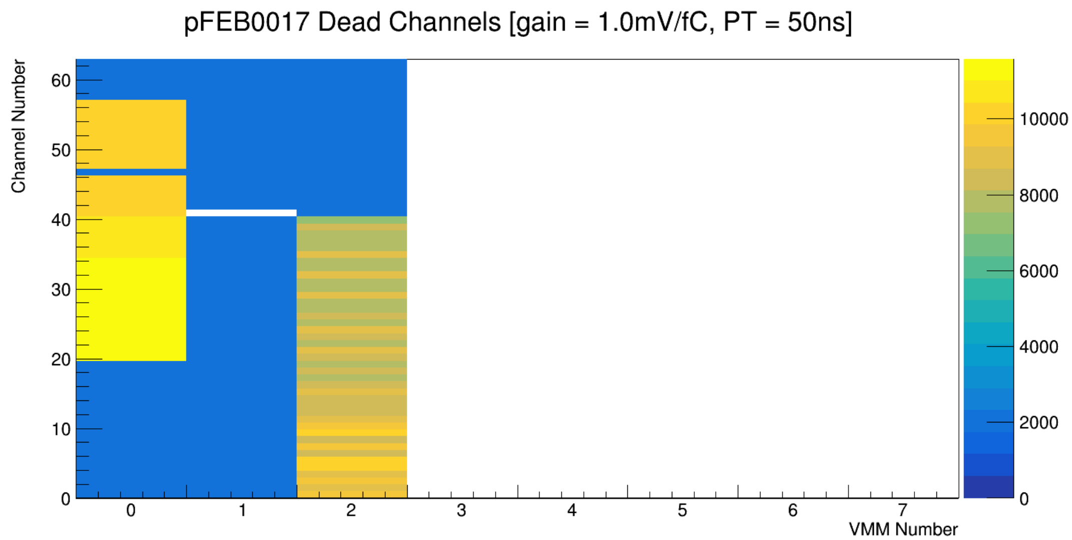

Figure 5.17: Dead channel results for a pFEB, dead channels are channels where no hits were recorded. These are represented as white squares on this plot. There are only 3 VMMs on a pFEB which is why there are no hits in VMMs 3-7.

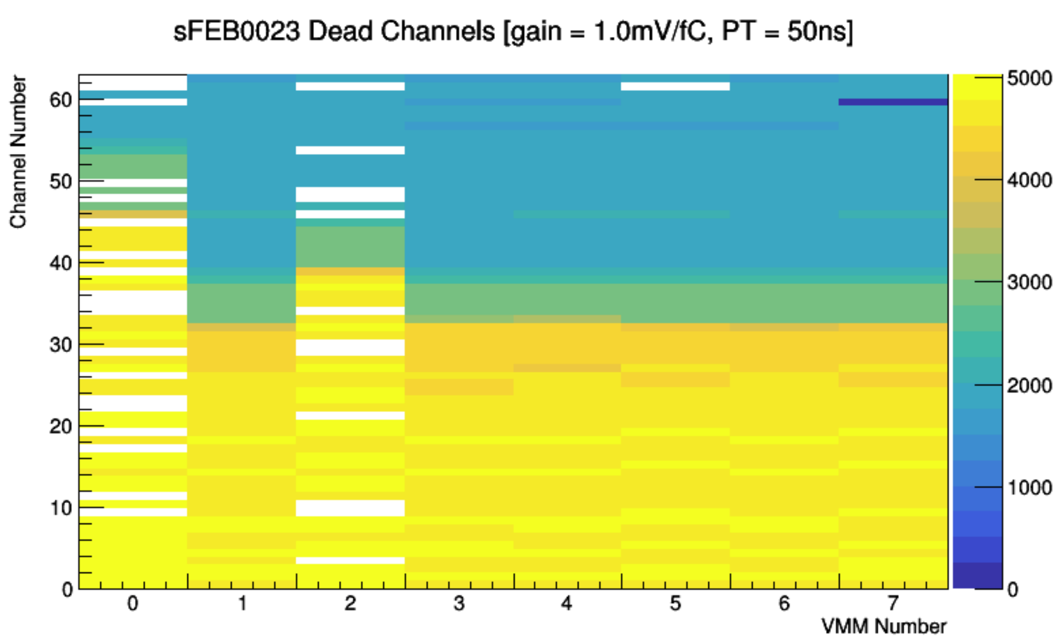

Figure 5.18: Dead channel results for an sFEB: dead channels are channels where no hits were recorded. These are represented as white squares on this plot.

These sorts of dead channel scans are performed periodically to check the consistency of previous scans to see if any new dead channels arise or if any previously dead channels suddenly start recording hits. These plots can also be used to identify channels with abnormally high number of hits, for example channels [20-56] on VMM0 and channels [0-40] on Figure 5.17. The likely cause for these "hot" channels is that these channels require further optimization for the trim bits in order to equalize the number of hits across all 64 channels. Finally, it has also been observed that there is a large drop in the number of counts for channels [35-63] on the SFEBs. This drop is likely due to the test capacitor generating a negative "after" pulse following the initial positive test pulse combined with a large default readout window size of the SFEBs [59]. These two factors are an artifact of the miniDAQ system and have no effect on the results of the dead channel scans in any way, and only affect the aesthetics of the plot.

5.5.3 Pedestal Measurements

Recall that the pedestal is defined as a baseline value, measured in digital pdo values, when there are no input signals. The motivation for measuring this minimum pdo value for each channel is that it defines a cutoff for input signals, any signal with a pdo value less than this cutoff is most likely unwanted noise. Therefore, for offline data analyses this pedestal value is subtracted from the ADC data in order to remove low energy hits attributed to noise. One of the most useful properties of the VMM3 is the neighbour logic flag which allows for readout of channels that have not been explicitly set to accept data. Enabling test pulses on a channel with neighbour logic enabled forces channels adjacent to a triggered channel to be read out even if the threshold is not reached. This functionality is especially useful for measuring the pedestal value for each channel. It should be noted that this functionality was implemented explicitly for strips readout. The spatial resolution of the strips has an upper limit defined by the pitch of the strips if the charge is only deposited on a single strip. However, by sharing the charge among several strips, the position of the incoming particle is more precisely determined by fitting the charge distribution of the neighboring strips and determining the position of the peak charge.

The algorithm for measuring the pedestal value described was developed by the author. To begin, the neighbour logic flag is enabled for each VMM on a board and test pulses are sent to a subset of the 64 channels. To completely cover the 64 channels, two test pulser runs need to be taken. The first run starts with channels [1, 4, 7,..., 61] having test pulses enabled in order to read the pedestal values from the adjacent channels, [0, 2, 3, 5, 6, ..., 62]. The second run enables test pulses in channels [2, 5, 8, ..., 62] and pedestal values are read out for channels that were not covered in the first run.

The process for determining the pdo value makes use of the pdo monitoring histogram for each channel. Figure 5.19 (Top) is an example of a pdo distribution for a channel with no test pulses enabled that shows that the pdo distribution is peaked around a much lower pdo value corresponding to a baseline value. Whereas, Figure 5.19 (Bottom) is an example of a pdo distribution of a channel with test pulses enabled showing a peak at a much larger pdo corresponding to the height of the test pulse set by the user.

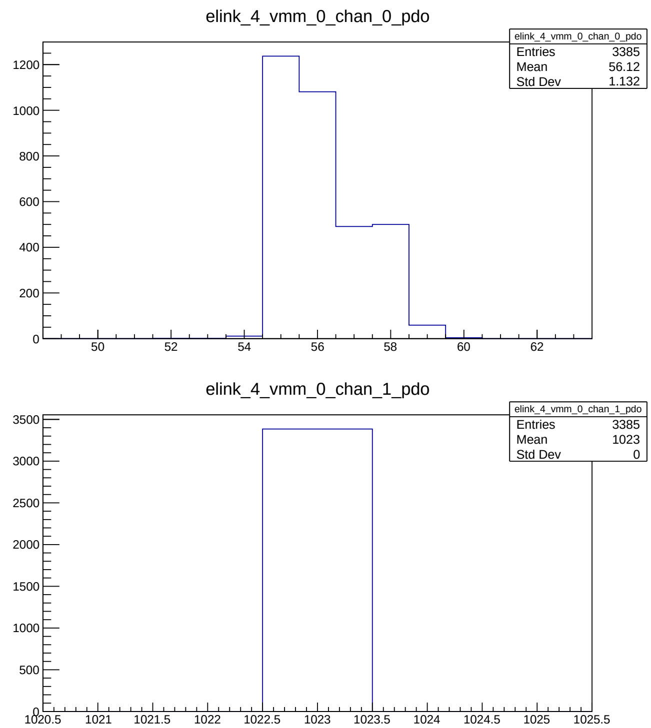

Figure 5.19: PDO monitor histograms that are used to extract the pedestal value for each channel. Top is a channel for which there were no test pulses enabled making use of the neighbour logic feature. Bottom is a channel for which there were test pulses enabled.

Similar to the measurements made for the baselines and threshold calibrations defined in previous sections, a Gaussian fit is applied to the channels with no test pulses enabled. The mean of the fit is taken as the digital pdo value corresponding to the baseline, and the width of the fit is defined as the RMS on this baseline value. However, there is a known issue with the VMM3 ADC known as residual accumulation which causes the nominally 10-bit precision to be reduced by 2 or 3 bits. For certain channels, this results in unwanted bits being enabled yielding a larger 10-bit ADC number. Visually, this is seen in the monitor histograms with two or more visible peaks; an example of such a channel is shown in Figure 5.20.

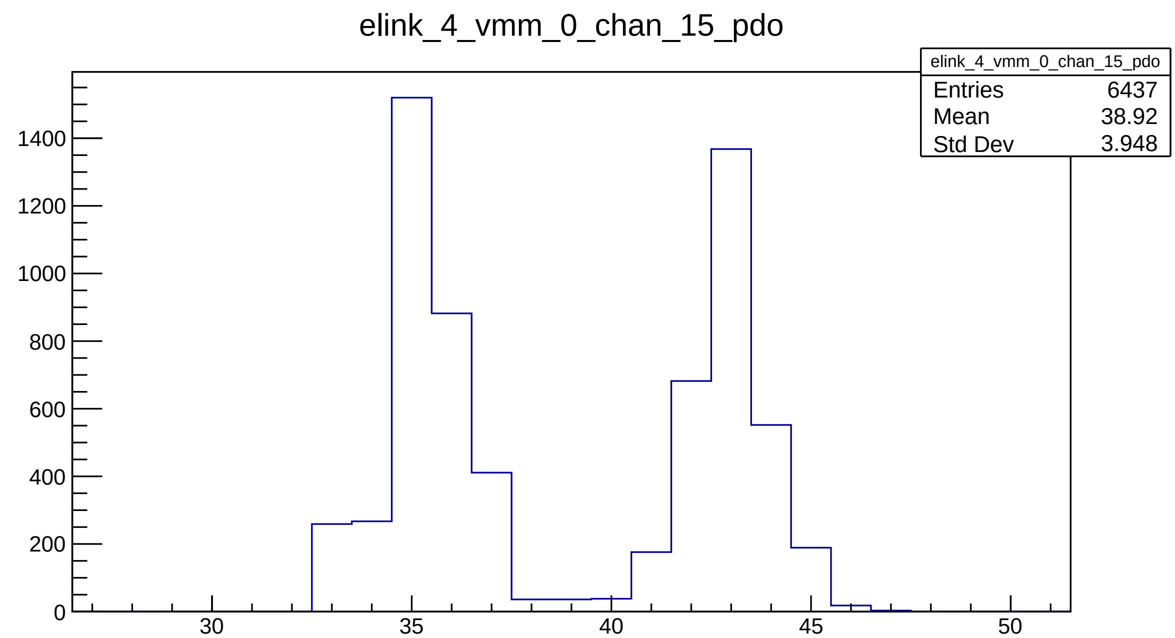

Figure 5.20: Residual accumulation in the VMM3 ADC causes unwanted bits in the 10-bit digital number to be high, resulting in double peaks in the pdo distribution. This is a known issue of the VMM3 ADC which has had minimal impact on the development of the algorithm. This results in slightly lower pedestal values being read out due to the algorithm selecting the left-most peak. Later iterations of the VMM chip will look to address this issue.

For channels exhibiting this behaviour, the pdo value is extracted using the data contained in the left-most peak. This is because the left-most peak is likely to be more accurate in the pdo value as the right peak(s) are likely due to the residual accumulation problem described above. The procedure for handling single-peak and multiple-peak distributions is discussed below. Furthermore, for later analyses it is safer to subtract a smaller pdo value rather than subtracting a value that is too high [59]. The complete iterative decision-making process of the algorithm for determining baselines is outlined in Figure 5.21.

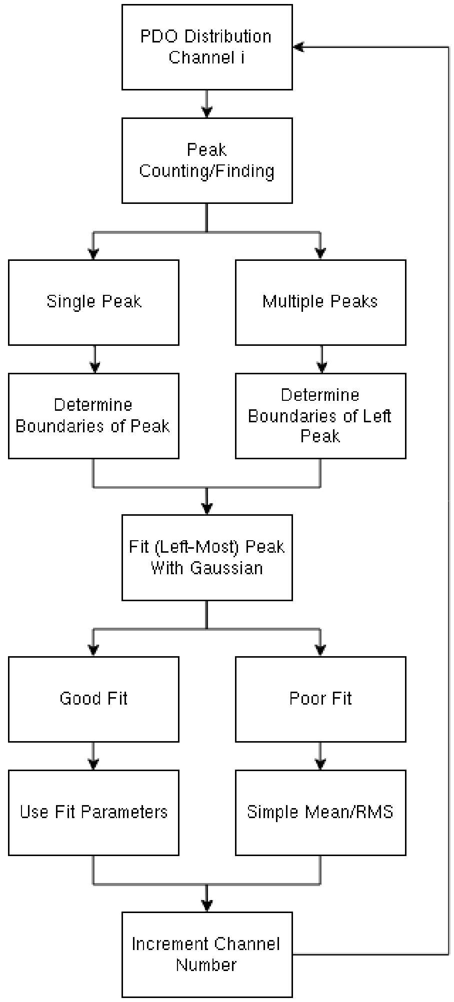

Figure 5.21: The decision making flowchart for extracting the baseline (pdo) value for each channel. The number of peaks is determined followed by an attempt to fit a Gaussian to compare the goodness of fit to a threshold.

5.5.3.1 Peak-Finding Step

The first step of the algorithm is at its core a peak finding and peak counting algorithm. The Root data analysis software [60] does include a peak finding feature in its TSpectrum class, however this feature was not used simply because positions of the peaks were off by a few bins. Therefore, a custom but very simple peak finding algorithm was developed by the student as a substitute. Firstly, criteria on what constitutes a peak is determined. This is done by first finding the bin with the highest number of counts since this will obviously be a peak. Second, a threshold in the form of a decimal number between

0 and 1 is defined, representing the fraction of the max number of counts found in the first step. The program will then scan all of the non zero bins looking for bins with counts greater than or equal to this fraction multiplied by the highest bin count. For example, if the highest bin count is 1000, and the user defined threshold is 0.3, then only bins that have at least $0.3 \times 1000 = 300$ counts are accepted as potential peaks. Finally, for bins that meet the previous condition, the program will then look at the two bins adjacent to it. In order for a bin to be considered a peak, the two adjacent bins must be lower than the bin in between them. For example, suppose that bin i passed the minimum height condition, the program then checks to see if bin $(i + 1) \leq$ bin i and bin $(i - 1) \leq$ bin i. An example of a well-identified peak is shown in Figure 5.22.

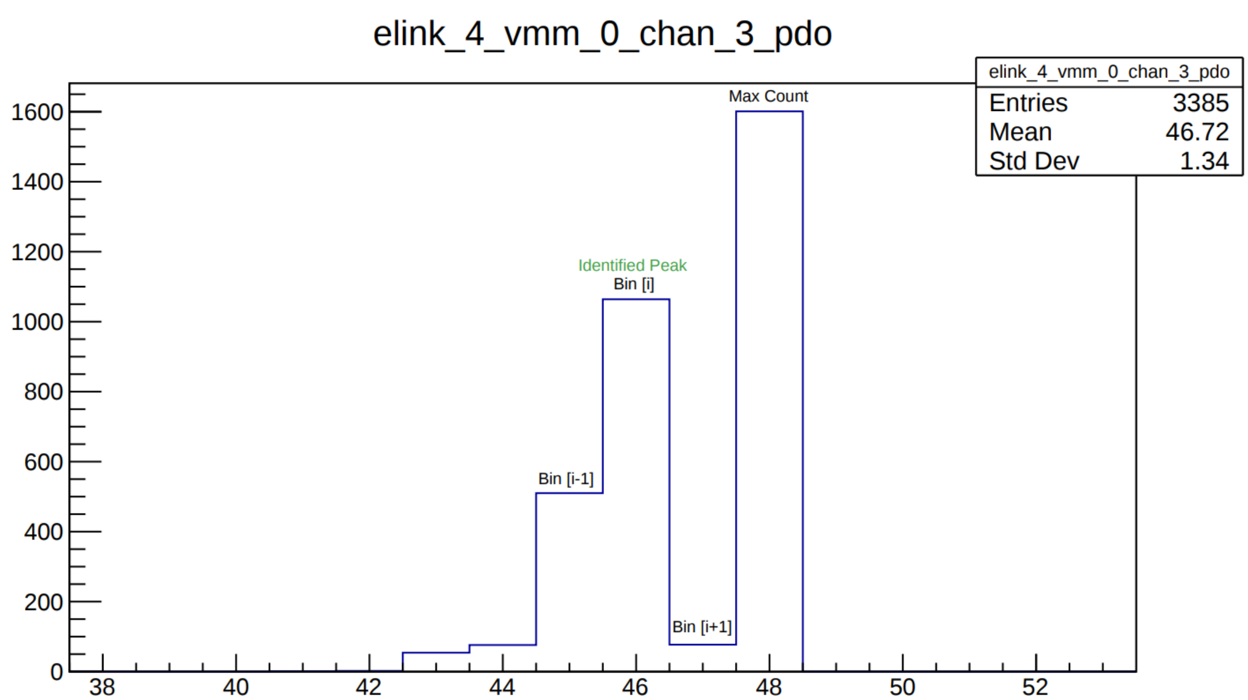

Figure 5.22: An example of a well-identified peak as found by the custom peak finding algorithm.

There are a few known issues with this method of identifying peaks. The first known issue is that the criterion that has been set is not robust, since it only checks the two bins on either side of a potential peak. This causes instances where the algorithm will misidentify a bin as a peak as shown in Figure 5.23 where the bin is identified as a peak by the program but does not visually look like a peak. Potential solutions involve setting the threshold fraction higher to avoid smaller peaks, but this runs into the problem of missing peaks altogether which is why it is currently set at a conservative 0.3. A second solution involves widening the criteria window to include bins $(i+2)$ and bins $(i-2)$ or wider. However, there will still be instances of mis-identification, the variability of the pdo distributions for each of the 64 total channels is the limiting factor for a well-performing peak-finding algorithm.

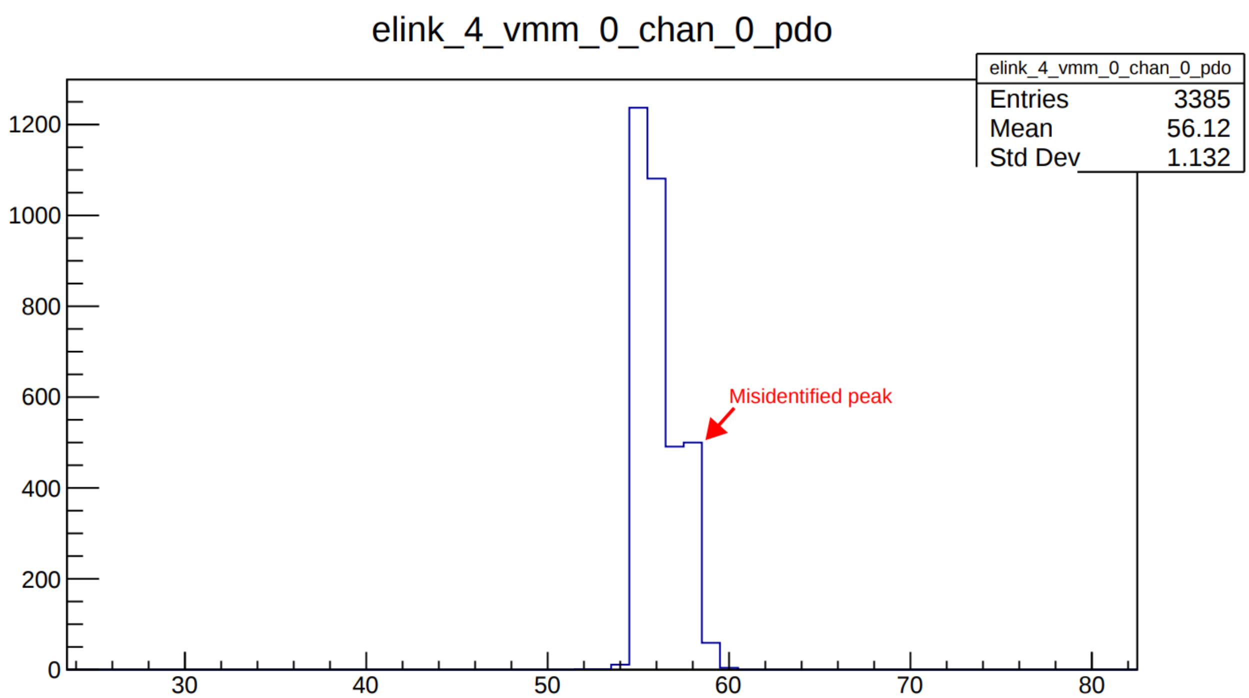

Figure 5.23: An example of a mis-identified peak as found by the custom peak finding algorithm.

There are of course more sophisticated algorithms for peak finding. One notable example is the so-called CLEAN algorithm developed by Jan Högbom in 1974 [61]. This technique was originally developed for finding the number of high intensity points on an intensity map in the field of radio astronomy. The technique starts by identifying the brightness and location of the most intense pixel and then iteratively subtracting a fraction of this brightness from the surrounding regions. One could imagine applying this technique to this project. First, the location and count of the highest peak is determined and

Gaussians are iteratively fit, whilst restricting the fit region to $\pm 3\sigma$. The fit is subtracted from the histogram and repeated for remaining peaks. The only issue with this sort of algorithm is again the variation in the histograms as well as being able to set a suitable threshold for determining secondary peaks relative to the largest peak.

5.5.3.2 Single-Peak Distributions

For channels with one identified peak, the next step is to attempt to fit a Gaussian to the distribution in order to extract the mean and the RMS. To determine whether the fit is good enough, the reduced chi square for each channel is compared to a user set reduced chi square threshold. If the χ^2 of the fit is less than the user set χ^2 threshold, then the mean and RMS of the Gaussian fit are recorded. Otherwise, the discrete mean and standard deviation for a histogram are used and are defined as follows, where the x_i are the bin positions, n_i is the count in the ith bin, and N is the total number of counts.

$$\bar{x} = \frac{1}{N} \sum_{i=LMB}^{M} n_i \times x_i \, ; \quad \sigma^2 = \frac{1}{N} \sum_{i=LMB}^{M} n_i \times (x_i - \bar{x})^2 \tag{6}$$

There is a further complication with so-called "stray" peaks as indicated in Figure 5.24, these are peaks that do not meet the criteria of the peak finder but still need to be excluded from the calculation of the mean and standard deviation. Including these would result in erroneously large standard deviations. In order to include only the bin(s) that make up the main peak, the sums in Equation 6 begin at the Left Most Bin (LMB) defined as the first bin greater than zero. Next, the program looks for the first bin with zero counts past the main peak and defines this as a Marker (M). Therefore, the sum for the mean and the standard deviation only takes into account the bins that make up the left-most peak. For the example shown below, the main peak is a delta function, however for channels that have one peak with a non-zero width, this process eliminates stray peaks.

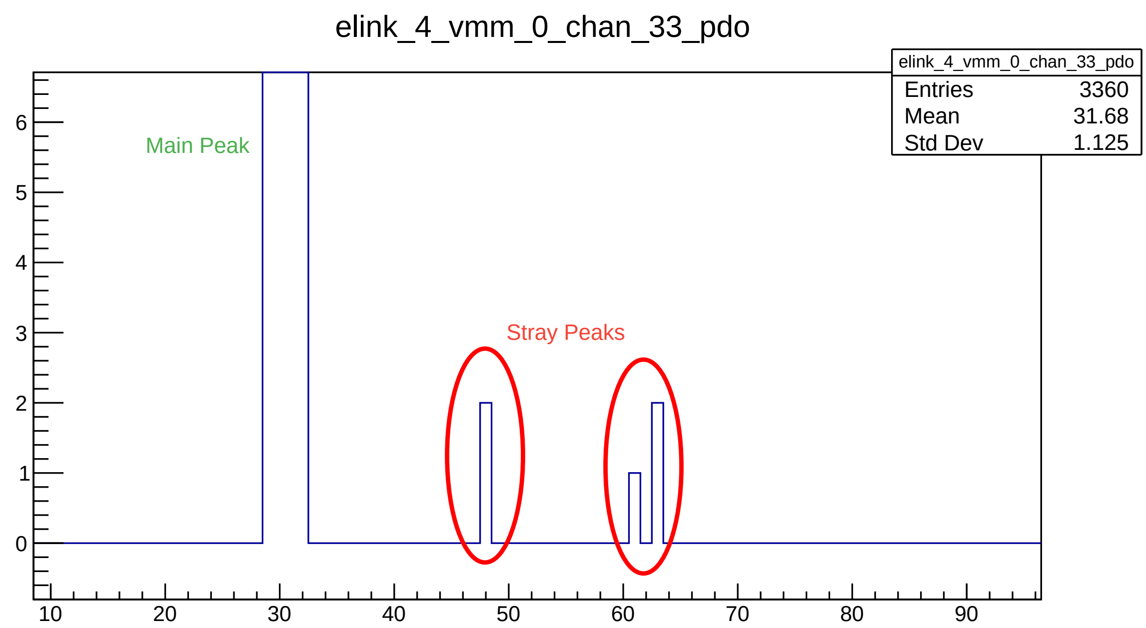

Figure 5.24: Bins with low counts that need to be excluded from calculations.

5.5.3.3 Multiple-Peak Distributions

For channels that exhibit the residual accumulation issue defined above, and have two or more distinct peaks then the process is more complicated. The main problem in these scenarios is determining a systematic approach to distinguishing one peak from the next. Recall that the operations are only performed on the left-most peak. In order to delimit the bins that make up the left-most peaks and nearby peaks (as shown in Figure 5.25), a two bin sliding window is used to define a marker in a similar process to when there was only one peak. Suppose that bin i corresponds to the position of the left-most peak as determined by the peak finding algorithm, then the window begins at bin $(i+1)$ and bin $(i+2)$. The criterion for the boundary between the end of one peak and the start of another is counts[bin $(i+1)$] $<$ counts[bin $(i+2)$] defining the rising edge and the start of another peak. Considering the figure below as an example, the window begins at bin 41 and increases sequentially until it meets the rising edge of the new peak at bin 47 and this is set as a marker. This marker is used as the boundary for fitting procedures and calculations.

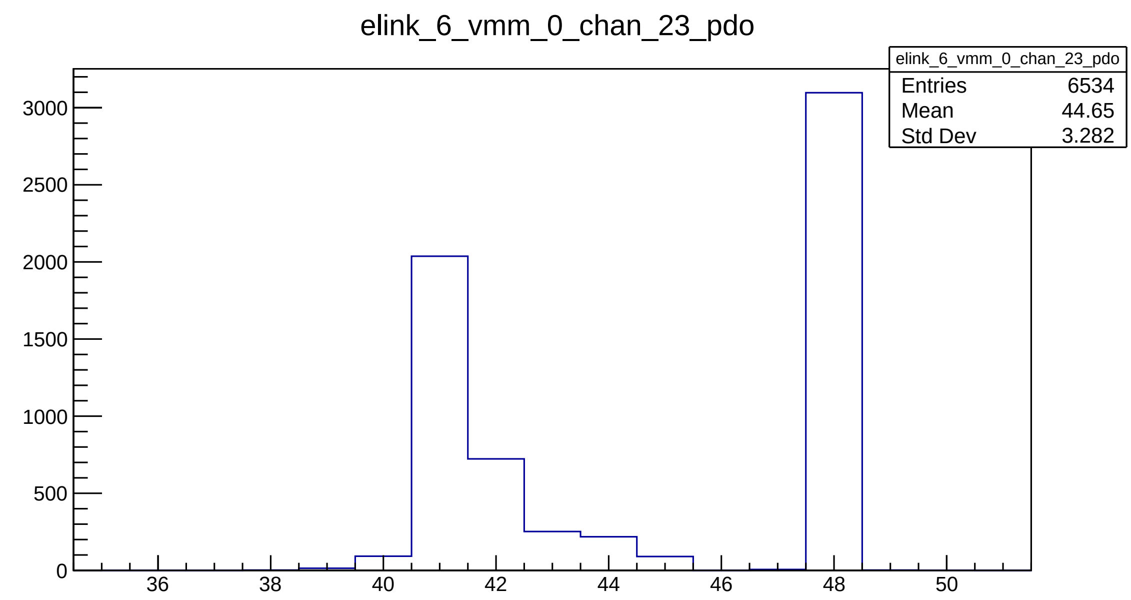

Figure 5.25: A two bin sliding window is used to determine the boundary between two peaks by finding the first bin of the rising edge of a new peak.

This process works for the example shown above where there is a distinctive gap between two peaks since the bins with zero counts will not affect any calculations, but also works for distributions with no gaps between the peaks. However, there are problems with this process for when the peaks are very close together in terms of bin numbers. This ultimately limits the range of the fitter resulting in frequent poor fits due to poor statistics.

After determining this marker, the final steps are very similar to the steps taken for channels with one peak. The program first attempts to fit a Gaussian to the left-most peak restricted by the marker, if the fit results are poor relative to a user set reduced χ^2 threshold, then the fit is rejected and Equation 6 is used to calculate the mean and the RMS using the bins in between the LMB and the Marker. The result of this process is a text file that will be incorporated later into the cosmic analysis software. The text file is organized into columns containing the following information:

VMM	VMM number, runs from 0...7
Channel	Channel number, runs from 0...64
Pedestal	pdo value extracted in units of ADC counts
RMS	Standard deviation of the pdo value extracted in units of ADC counts
MPeaks [0=No/1=Yes]	Binary value, whether there are multiple peaks
Simple [0=No/1=Yes]	Binary value, whether the fit failed and a simple mean/RMS was used

Table 1: Description of the different columns contained in the pedestal text file output by the pedestal measurements program.

This section dealt with the information read-out by the boards as it recorded successful hits. With the measurement of the baseline value, one can get a better idea of the behaviour of the board when there were no inputs. The results of the algorithm used to record the pedestal values were directly implemented into the cosmic ray analysis software which has been distributed to other test sites since November 2018. Finally, having identified any faulty channels, these can be safely masked for future data taking runs.

6 Conclusion

After the long shutdown scheduled to begin in 2019, the luminosity of the LHC will increase, greatly raising the rate of incoming data. In order to cope with the increased rate, there are a number of upgrades scheduled for the long shutdown. One of the areas seeing an upgrade is the inner end cap stations of the muon system, known as the small wheels. The current system will quickly become overwhelmed by the increased rate due to triggering on fake muons. To decrease the trigger rate (and the amount of data that needs to be stored) the current detector technology will be replaced with sTGCs and Micromegas.

sTGCs are divided into trapezoidal shaped wedges known as quadruplets. Canada plays a large role in the production and testing of these quadruplets. The first production quad was completed in the summer of 2018. McGill participates in the cosmic ray testing of these production quads, and a description of the McGill sTGC lab was presented. The main component of the work presented in this thesis revolved around the various characterization procedures of the front-end electronics used to read out the different electrodes making up the quad.

The first step in these characterization studies is to understand the different integrated circuits that make up the front-end boards. In particular, the function of the VMM3 as a pulse-shaping device and ADC was described. As the third iteration of the VMM ASIC, the VMM3 boasts rapid continuous readout with mixed-signal (analog and digital) readout capabilities. A miniDAQ system made up of these boards along with a KC705 FPGA collect the readout signals and feeds them into a read out software designed specifically to interact with the various board components.

The main goal of these characterization studies is to determine a threshold, in order to minimize the amount of noise collected. The baseline for each channel is determined and it is observed that variations between channels and between chips exist, therefore it is necessary to perform these measurements for each VMM on a board. Repeating these measurements multiple times will improve the precision of these baseline measurements. In addition, a more sophisticated fitting procedure might reduce the number of outlying points observed, however the variation in the shapes of the pdo distributions makes developing a smarter fitting algorithm difficult.

In addition, in the process of performing these measurements, a cursory approach to error analysis was used. Here, the systematic error associated with any non-linearity of the ADCs was overlooked because of the poor fits that resulted. Future analyses with similar data should make use of the error on the mean as well as including an estimate of the systematic errors (based on the intrinsic resolution of the 12-bit ADC) for a more complete error analysis.

Furthermore, in the process of performing these measurements, the performance of each channel was checked to see if it is behaving normally or if it is electronically dead. Dead channel scans were shown for one pFEB and one sFEB and it is observed that sFEBS are more prone to dead channels. These scans are performed periodically for each new quad in order to verify the consistency of the previous measurements. The channels reported to be dead are also compared with dead channels reported during actual data-taking runs to check whether it is an electronics issue or a mechanical/connectivity issue.

Finally, much of the time was dedicated to developing an algorithm which performs pedestal measurements intelligently with minimal user intervention. The algorithm uses two user set thresholds: a fractional number used to identify peaks, and a floating point larger than 1.0 used to check the goodness of the Gaussian fits; these are currently set at 0.3 and 10.0 respectively. As a result, mis-identification of peaks and poor fits are the largest problems, and improvements to the peak finding algorithm and fitting procedures have been offered above. These results are a good starting point for future investigations and are accurate enough to be included in the cosmic ray analysis software and the use of which may or may not be fully applied in the ATLAS setting. Further studies involved in fine-tuning these threshold parameters may yield different results, but it is difficult to determine a perfect number. For example, using a larger fraction for the peak threshold may reject smaller, insignificant peaks but may also cause unwanted rejection of peaks falling below this threshold. Therefore, future optimization studies varying the values can be performed in order to observe the effects on the outputted data files.

The C++ scripts used to perform the above calibration steps were written by the author and can be found at the following repository: `https://gitlab.com/charliebchen/mcgill-stgc-feb-vmm3-characterization`. Ultimately, these results are fed into a cosmic analysis software written by members of the McGill sTGC group. A description of the software as well as examples of efficiency plots are shown in Appendix B. Including these, the software also computes the various other parameters used as measures of performance. A quad satisfying these performance criteria is then shipped to CERN where it is finally assembled into a wedge as part of the NSW.

A Cosmic Ray Hit Maps

The bulk of the work making up this thesis used the built-in feature of the VMM3 to generate its own test pulses. However, cosmic ray data is used to characterize the performance of the actual sTGC quadruplets. This section shows the hit-maps for the 3 different types of electrodes (wires, pads, strips) for each of the 4 gas layers. These are used in order to quickly identify any faulty channels, whether they be dead channels or channels showing abnormally high counts, also known as a "hot" channel. These are used to compare with the dead channel scans described in Section 5.5.2 to identify dead channels that are not due to electronic issues. The hit-maps for the wires and the pads for the four layers are shown in Figures A.1 and A.2 respectively. The amount of data constituting the hit-maps below was taken over a collection period of approximately 3 hours.

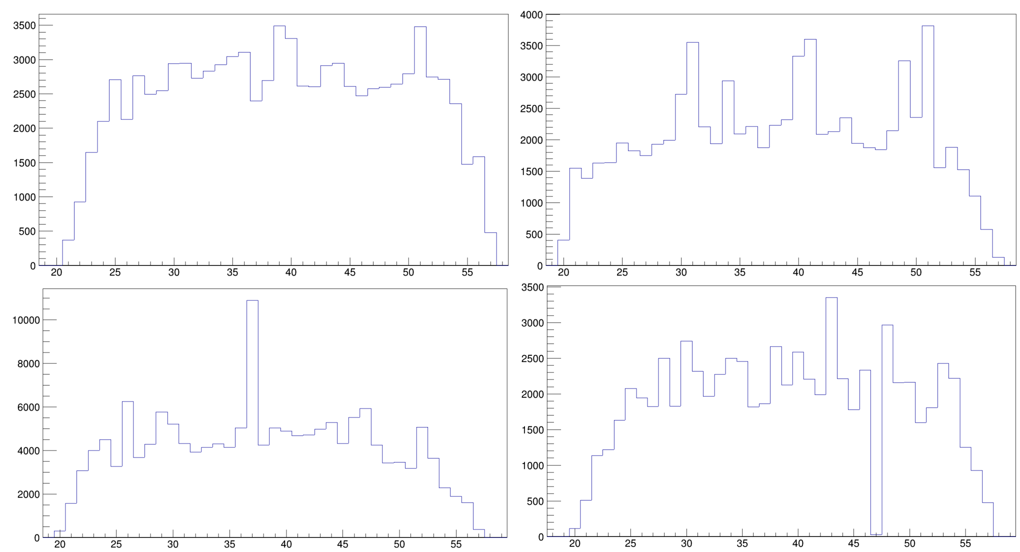

Figure A.1: The hit-maps for the wires for all four layers obtained using cosmic ray data. Top left: Layer 1, Top right: layer 2, Bottom left: Layer 3, Bottom right: Layer 4.

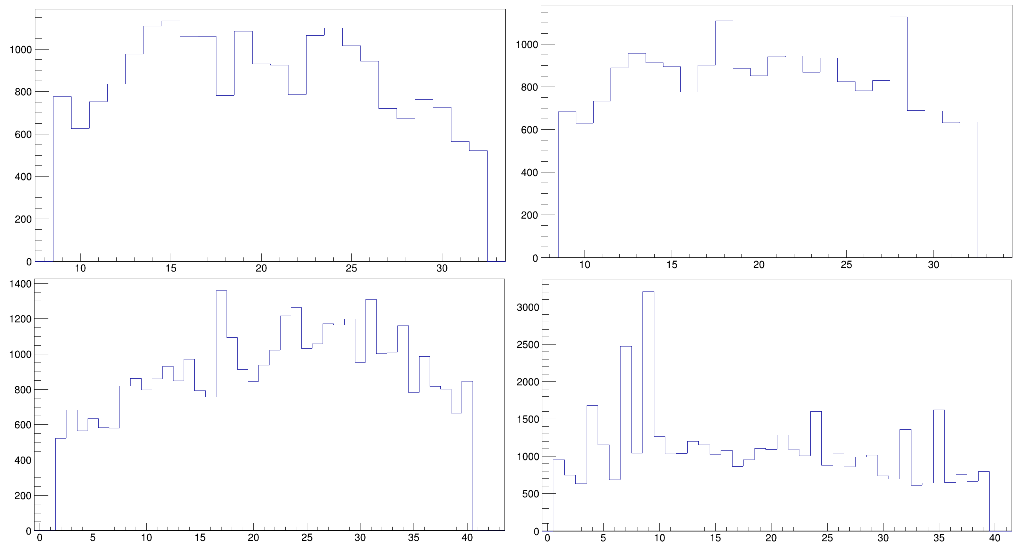

Figure A.2: The hit-maps for the pads for all four layers obtained using cosmic ray data. Top left: Layer 1, Top right: layer 2, Bottom left: Layer 3, Bottom right: Layer 4.

The hit-maps for the strips for one of the four layers is shown below in Figures A.3. Only one layer is shown since the remaining three layers are very similar. In these plots, it is observed that there are periodic dips in counts, and this is attributed to button supports placed periodically on the strip cathode board in order to maintain a constant width between cathode planes. Also, for each layer 5 plots (corresponding to 5 VMMs) are needed to read out all of the strips. This is because a single VMM has only 64 channels, and so a minimum of 5 VMMs are needed to readout the approximately 300 strips in a layer. This cosmic data is later compiled and fed into a cosmic ray analysis software written by members of the McGill sTGC group[4] (Benoit Lefebvre, Waleed Ahmed). This software computes metrics of performance such as the efficiency for each electrode type and layer as well as the spatial resolution.

[4]sTGC Cosmic Analysis Software Gitlab: `https://gitlab.cern.ch/McGill-sTGC/tgc_analysis/`

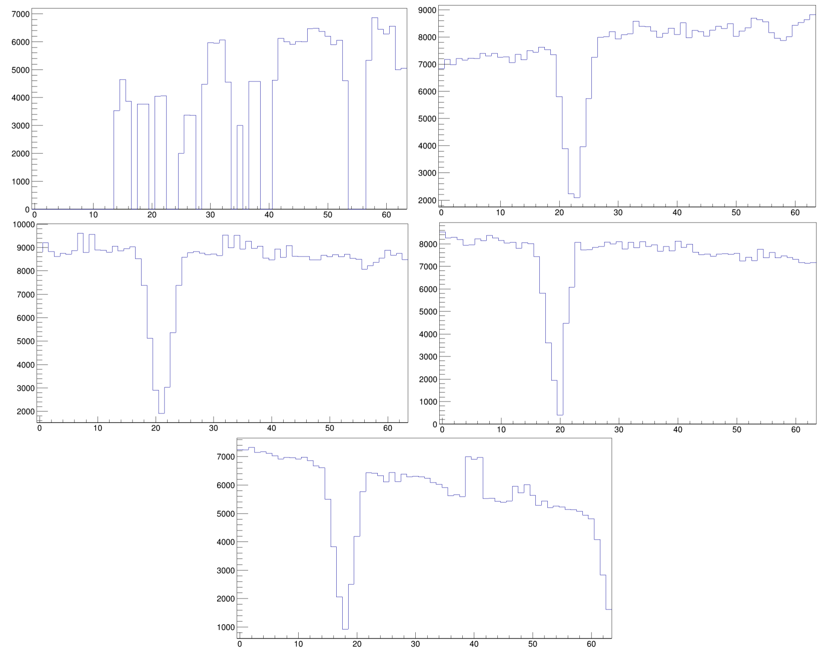

Figure A.3: Hit maps for the strips on Layer 1 using cosmic rays.

B Cosmic Ray Analysis Software

The cosmic ray analysis software is written and maintained by other members of the McGill sTGC group and is used to compute the metrics of performance of a quad. It was originally developed for the first generation VMM1 and a much smaller prototype quadruplet but has now been adapted for the QS3P production quads and the modern VMM3. The software accepts the outputted binary data files and generates a number of high-level plots used to characterize the performance of the quad. Some of the most important plots include raw hit maps, efficiencies for each layer, as well as performing measurements used to detect translational or rotational misalignment. These plots can be used to visually target individual channels with lower efficiencies for further threshold optimization. This software will be made available to the other test sites once other detector geometries are implemented into the software.

The efficiency plots for the pads, wires and strips of each layer are shown below. In these plots, the efficiency is defined as the ratio of particles traversing 3-out-of-4 layers to the total number of triggered events. The plots are constructed according to the geometry and dimensions of the production quad with the origin set at the wires adapter board on the long edge of the trapezoid.

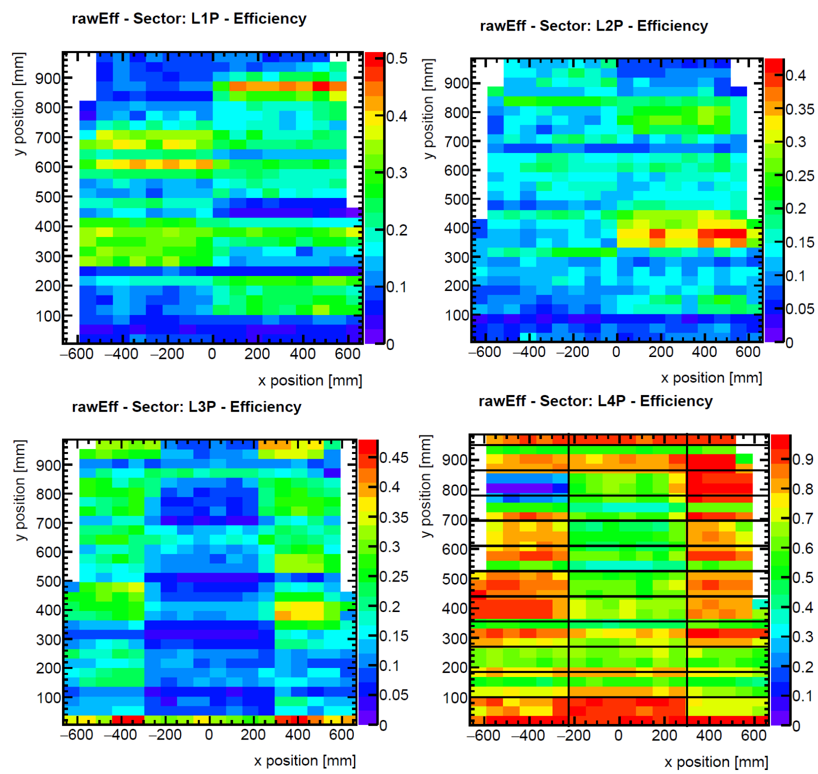

Figure B.1: Efficiency maps for the pads calculated using the cosmic ray analysis software. The abnormally low efficiencies on layers one, two and three indicate that the set thresholds (or trim values) are incorrect. Recall that these values were determined automatically using the built-in calibration functions of the DAQ software and are essentially a "black-box" in terms of functionality. Therefore, different manual threshold optimization steps are being tested to see their effect on the efficiency.

Figure B.1 shows the efficiency map of the pads for the four layers. It is observed that many of the pads, especially on layers one through 3, have extremely low efficiency. This indicates that the thresholds that have been set require further optimization. Layer four on the other hand has much higher efficiency because some pads on this layer had been manually optimized using the digital pdo distributions. This process involves taking data using cosmic rays for a brief amount of time and examining the pdo distributions for select channels. The trim value is then adjusted to shift the pdo distribution out of the noise. This process is extremely time-consuming and thus manual optimization procedures using the analog monitor output capability are currently being investigated.

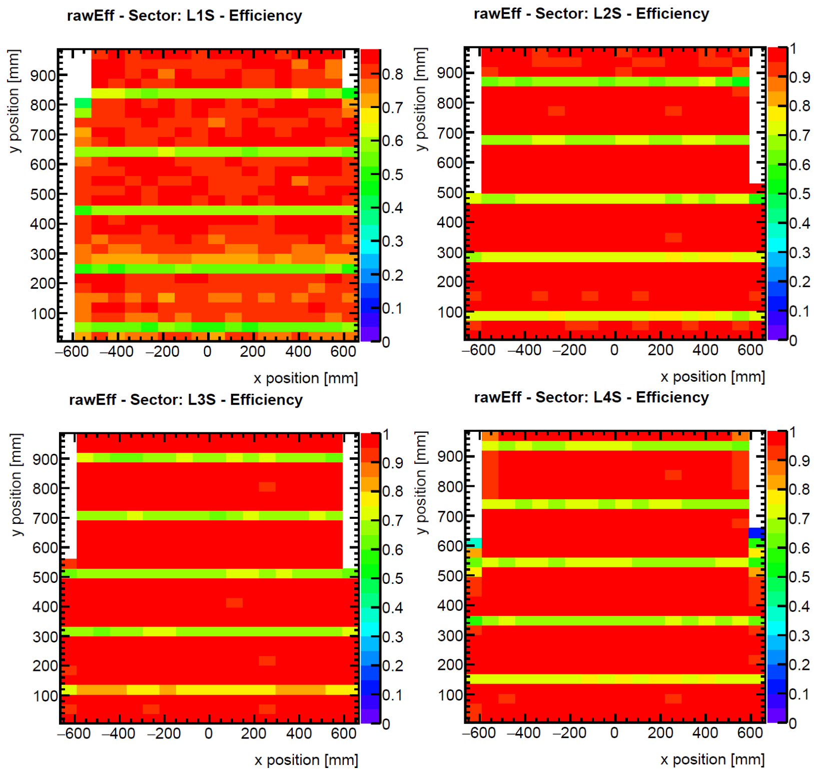

Figure B.2: Efficiency maps for the strips calculated using the cosmic ray analysis software.

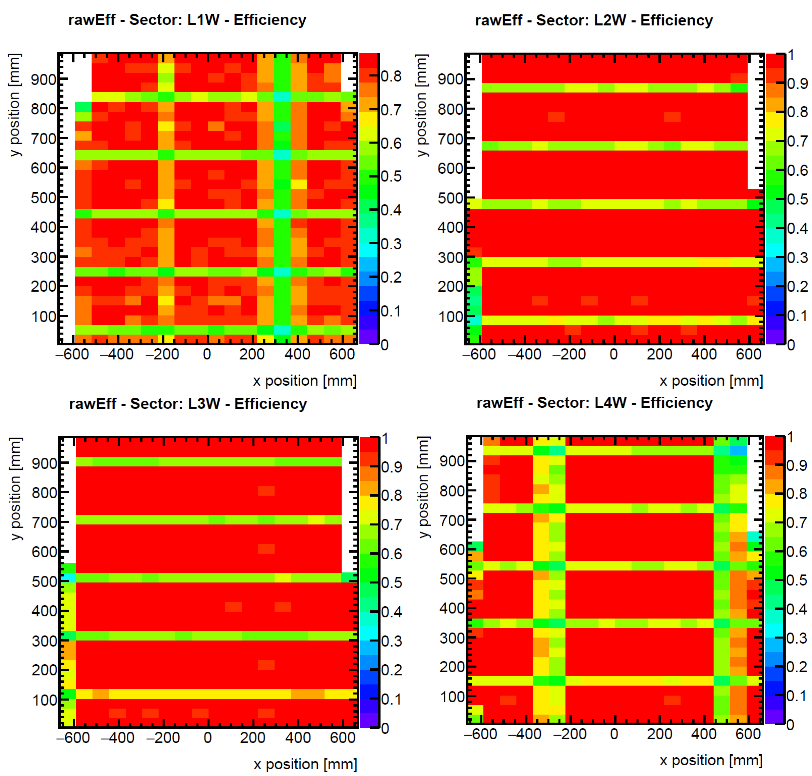

Figure B.3: Efficiency maps for the wires calculated using the cosmic ray analysis software.

Figures B.2 and B.3 show the efficiency plots for the strips and the wires. Unlike the pads, the strips and the wires have efficiencies regularly greater than 90% and indicate that the current thresholds are correctly set. However, both strips and wires show sporadic regions of lower efficiency that could be due to connectivity issues. Both sets of plots also show regularly spaced regions of lower efficiency, but these are attributed to supports and other mechanical structures on the electrodes.

C QS3P Electrode Geometry and Mapping

The QS3P is the naming scheme that refers to the outermost pivot sTGC quadruplet on a small sector. The QS3P is made up of four individual layers that function as four independent multi-wire proportional detectors. Each layer contains three different types of electrodes used for readout: pads, wires and strips, ordered in ascending degrees of granularity. In order to increase resolution during track reconstruction, the cathode planes containing the pads and strips are oriented such that the linear distance between pad cathode planes is maximized. This ordering of the cathode layers is shown in Figure C.1.

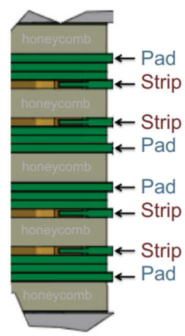

Figure C.1: A schematic showing the arrangement of the pads and strips cathode planes. The distance between consecutive triggering (pad) planes is maximized to obtain an optimal track segment measurement [51].

A general description of the quadruplet and these electrodes, along with an overall technical drawing was presented in Section 5.1. This section provides a more detailed illustration of the electrode geometry for all four layers. The following is a brief guide on converting from VMM channel number recorded by the DAQ to a physical electrode number found on the quad.

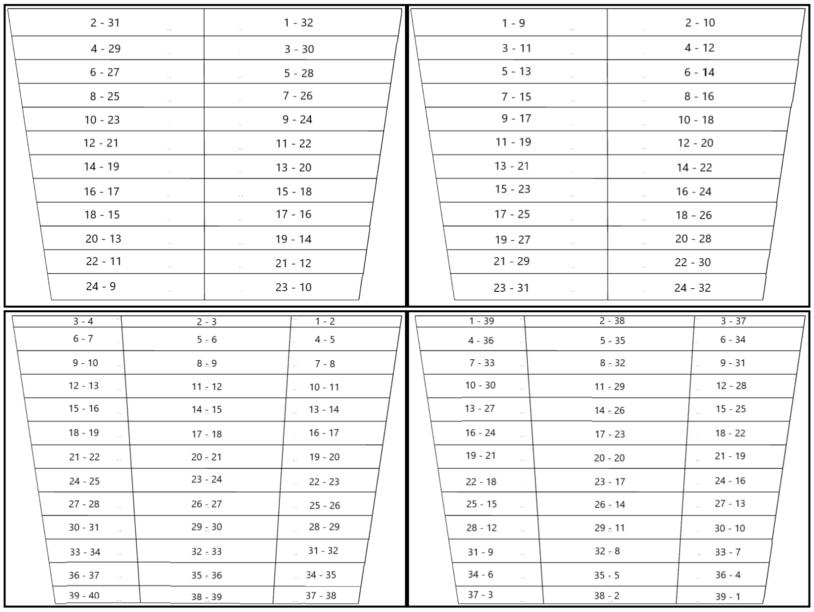

Figure C.2: Pads electrode layout for the four layers of a sTGC quadruplet. Layers 1 (top left) and 2 (top right) each have 24 pads, while layers 3 (bottom left) and 4 (bottom right) each have 39 pads. Also included is a mapping between the pad number and the VMM channel number.

Figure C.2 shows the pad layout for the 24 pads of layers one and two and the 39 pads found in layers three and four. Also labeled is a pad-to-channel mapping, such that the first number before the hyphen is the pad number and the second number is the VMM channel (pads for any single layer are all electrically connected to VMMC). It should be noted that this mapping scheme is done from the perspective of looking from "inside" the gas gaps and looking at the pad cathode plane. Therefore, it is useful to reference Figure C.1 and imagine oneself in between a gas gap and looking at the pad cathode plane in order to accurately make use of the mapping in Figure C.2.

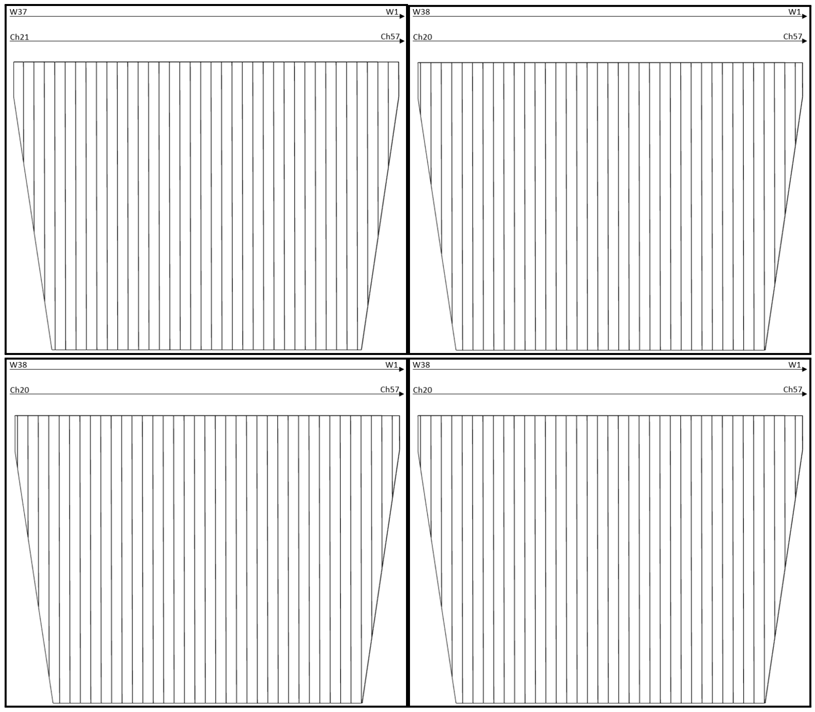

Figure C.3: Wires electrode layout for the four layers of a sTGC quadruplet. Layers 1 (top left) has 37 wire groups while the remaining 3 layers each have 38.

Figure C.3 shows the individual wire groups spanning the width of a quad. In similar fashion to the pads, each wire group is labeled with a number and is electronically connected to a specific VMM channel (VMMA for wires). In the above figure, the two arrows at the top of each drawing show the descending wire number and the ascending VMM channel number as one moves across the quad.

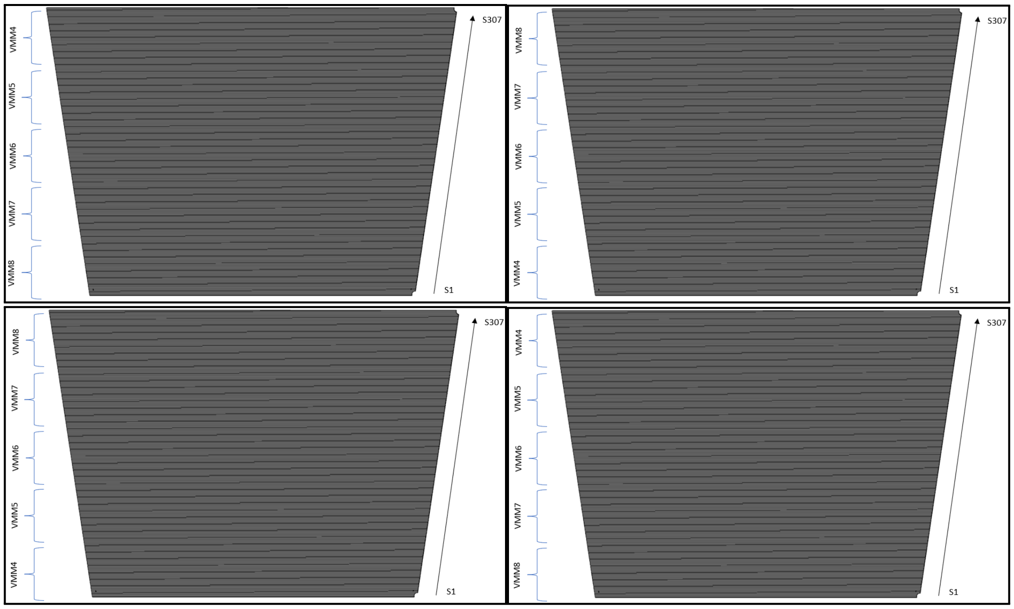

Figure C.4: Strips electrode layout for the four layers of a sTGC quadruplet. Each of the four layers has a total of 307 strips running perpendicularly to the wires.

Figure C.4 shows the 307 strips found in each of the four layers. However, unlike the wires and the pads, which could all be electrically connected to a single VMM, the 307 strips are distributed across 5 VMMs (VMM4 - VMM8); a VMM has a maximum capacity of 64 readout channels. Again each strip is labeled by a specific number from 1 to 307 running from the shorter edge to the longer edge. Also, approximately labeled is the number of the VMM responsible for reading out that section of strips. Notice that for certain layers the VMM numbers run ascending (from shorter edge to longer edge) while others are descending.

In summary, being able to quickly convert from a VMM channel number to an electrode number is useful in being able to identify a physical location on the quad requiring further analysis. A more complete mapping with complete channel numbering for each of the 307 strips in the form of a spreadsheet can be found on the same gitlab where the scripts can be found (`https://gitlab.com/charliebchen/mcgill-stgc-feb-vmm3-characterization`). Finally, given that McGill's role will switch in 2019 to the QL2 quadruplet type (middle sector on a large wedge), a channel mapping for the QL2 is located in the same repository.

References

[1] S. L. Glashow, "Partial-symmetries of weak interactions," *Nuclear Physics*, vol. 22, no. 4, pp. 579 – 588, 1961. [Online]. Available: http://www.sciencedirect.com/science/article/pii/0029558261904692 4

[2] S. Weinberg, "A model of leptons," *Phys. Rev. Lett.*, vol. 19, pp. 1264–1266, Nov 1967. [Online]. Available: https://link.aps.org/doi/10.1103/PhysRevLett.19.1264 4

[3] A. Salam, "Elementary particle physics: Relativistic groups and analyticity," *Eighth Nobel Symposium. Stockholm: Almquvist and Wiksell*, p. 367, 1968. 4

[4] D. J. Gross and F. Wilczek, "Ultraviolet behavior of non-abelian gauge theories," *Phys. Rev. Lett.*, vol. 30, pp. 1343–1346, Jun 1973. [Online]. Available: https://link.aps.org/doi/10.1103/PhysRevLett.30.1343 4

[5] M. E. Naschie, "On quarks confinement and asymptotic freedom," *Chaos, Solitons & Fractals*, vol. 37, no. 5, pp. 1289 – 1291, 2008. [Online]. Available: http://www.sciencedirect.com/science/article/pii/S0960077908000490 4

[6] ATLAS Collaboration, "Observation of a new particle in the search for the standard model higgs boson with the atlas detector at the lhc," *Physics Letters B*, vol. 716, no. 1, pp. 1 – 29, 2012. [Online]. Available: http://www.sciencedirect.com/science/article/pii/S037026931200857X 5

[7] "Standard Model of Particle Physics." [Online]. Available: https://en.wikipedia.org/wiki/Standard_Model#/media/File:Standard_Model_of_Elementary_Particles.svg 5

[8] M. Gell-Mann, "A schematic model of baryons and mesons," *Physics Letters*, vol. 8, pp. 214–215, Feb. 1964. [Online]. Available: http://adsabs.harvard.edu/abs/1964PhL.....8..214G 5

[9] G. Zweig, "An SU(3) model for strong interaction symmetry and its breaking. Version 1," 1964. 5

[10] F. Abe, H. Akimoto, A. Akopian, M. G. Albrow, S. R. Amendolia, D. Amidei, J. Antos, C. Anway-Wiese, S. Aota, G. Apollinari, and et al., "Observation of Top Quark Production in $p\bar{p}$ Collisions with the Collider Detector at Fermilab," *Physical Review Letters*, vol. 74, pp. 2626–2631, Apr. 1995. 5

[11] B. Pontecorvo, "Mesonium and Anti-Mesonium," *Journal of Experimental and Theoretical Physics*, vol. 6, p. 429, May 1957. [Online]. Available: http://www.jetp.ac.ru/cgi-bin/e/index/e/6/2/p429?a=list 6

[12] Y. Fukuda, T. Hayakawa, E. Ichihara, K. Inoue, K. Ishihara, H. Ishino, Y. Itow, T. Kajita, and et al., "Evidence for Oscillation of Atmospheric Neutrinos," *Physical Review Letters*, vol. 81, pp. 1562–1567, Aug. 1998. 6

[13] SNO Collaboration, "Direct evidence for neutrino flavor transformation from neutral-current interactions in the sudbury neutrino observatory," *Phys. Rev. Lett.*, vol. 89, p. 011301, Jun 2002. [Online]. Available: https://link.aps.org/doi/10.1103/PhysRevLett.89.011301 6

[14] C. Patrignani *et al.*, "Review of Particle Physics," *Chin. Phys.*, vol. C40, no. 10, p. 100001, 2016. 6, 9, 10

[15] F. Englert and R. Brout, "Broken Symmetry and the Mass of Gauge Vector Mesons," *Physical Review Letters*, vol. 13, pp. 321–323, Aug. 1964. 7

[16] P. W. Higgs, "Broken Symmetries and the Masses of Gauge Bosons," *Physical Review Letters*, vol. 13, pp. 508–509, Oct. 1964. 7

[17] G. S. Guralnik, C. R. Hagen, and T. W. Kibble, "Global Conservation Laws and Massless Particles," *Physical Review Letters*, vol. 13, pp. 585–587, Nov. 1964. 7

[18] J. Schwinger, "On Quantum-Electrodynamics and the Magnetic Moment of the Electron," *Physical Review*, vol. 73, pp. 416–417, Feb. 1948. 7

[19] G. Gabrielse, D. Hanneke, T. Kinoshita, M. Nio, and B. Odom, "New determination of the fine structure constant from the electron g value and qed," *Phys. Rev. Lett.*, vol. 97, p. 030802, Jul 2006. [Online]. Available: https://link.aps.org/doi/10.1103/PhysRevLett.97.030802 7

[20] K. A. Meissner and H. Nicolai, "Conformal symmetry and the Standard Model," *Physics Letters B*, vol. 648, pp. 312–317, May 2007. 7

[21] J. L. Feng, K. T. Matchev, and F. Wilczek, "Neutralino dark matter in focus point supersymmetry," *Physics Letters B*, vol. 482, no. 4, pp. 388 – 399, 2000. [Online]. Available: http://www.sciencedirect.com/science/article/pii/S0370269300005128 8

[22] P. H. Chankowski, J. Ellis, K. A. Olive, and S. Pokorski, "Cosmological fine tuning, supersymmetry and the gauge hierarchy problem," *Physics Letters B*, vol. 452, no. 1, pp. 28 – 38, 1999. [Online]. Available: http://www.sciencedirect.com/science/article/pii/S0370269399001689 8

[23] C. Grupen and B. Shwartz, *Particle Detectors*, 2nd ed., ser. Cambridge Monographs on Particle Physics, Nuclear Physics and Cosmology. Cambridge University Press, 2008. 8, 10, 12, 14, 24

[24] P. Sigmund, *Particle Penetration and Radiation Effects: General Aspects and Stopping of Swift Point Charges*, 2006. 8

[25] M. Boezio and E. Mocchiutti, "Chemical composition of galactic cosmic rays with space experiments," *Astroparticle Physics*, vol. 39-40, pp. 95 – 108, 2012, cosmic Rays Topical Issue. [Online]. Available: http://www.sciencedirect.com/science/article/pii/S0927650512001119 11

[26] W. Baade and F. Zwicky, "Cosmic Rays from Super-novae," *Proceedings of the National Academy of Science*, vol. 20, pp. 259–263, May 1934. 11

[27] A. Haungs *et al.*, "KCDC - The KASCADE Cosmic-ray Data Centre," *J. Phys. Conf. Ser.*, vol. 632, no. 1, p. 012011, 2015. 11

[28] W. R. Leo, *Techniques for Nuclear and Particle Physics Experiments: A How to Approach*, 1987. 13, 15

[29] H. Iams and B. Salzberg, "The secondary emission phototube," *Proceedings of the Institute of Radio Engineers*, vol. 23, no. 1, pp. 55–64, Jan 1935. 13

[30] "Photomultiplier Tube Schematic." [Online]. Available: https://en.wikipedia.org/wiki/Photomultiplier#/media/File:PhotoMultiplierTubeAndScintillator.svg 14

[31] G. Charpak, R. Bouclier, T. Bressani, J. Favier, and Ä. ZupanÄŊiÄŊ, "The use of multiwire proportional counters to select and localize charged particles," *Nuclear Instruments and Methods*, vol. 62, no. 3, pp. 262 – 268, 1968. [Online]. Available: http://www.sciencedirect.com/science/article/pii/0029554X68903716 14

[32] T. Schörner-Sadenius, Ed., *The Large Hadron Collider*. Berlin: Springer, 2015. [Online]. Available: http://www.springer.com/gb/book/9783319150017 16

[33] F. Englert, "The BEH mechanism and its scalar boson," *Annalen Phys.*, vol. 526, no. 5-6, pp. 201–210, 2014. 16

[34] I. Aracena, "Operational experience of the atlas high level trigger with single-beam and cosmic rays," in *2009 IEEE Nuclear Science Symposium Conference Record (NSS/MIC)*, Oct 2009, pp. 219–222. 17

[35] O. Brüning, H. Burkhardt, and S. Myers, "The large hadron collider," *Progress in Particle and Nuclear Physics*, vol. 67, no. 3, pp. 705 – 734, 2012. [Online]. Available: http://www.sciencedirect.com/science/article/pii/S0146641012000695 17

[36] M. Benedikt, P. Collier, V. Mertens, J. Poole, and K. Schindl, "LHC Design Report. 3. The LHC injector chain," 2004. 18

[37] The ATLAS Collaboration, "The atlas experiment at the cern large hadron collider," *Journal of Instrumentation*, vol. 3, no. 08, p. S08003, 2008. [Online]. Available: http://stacks.iop.org/1748-0221/3/i=08/a=S08003 18, 19, 20, 21, 22, 23, 24

[38] E. Daw, "Lecture 7 - rapidity and pseudorapidity," 2012. [Online]. Available: http://www.hep.shef.ac.uk/edaw/PHY206/Site/2012_course_files/phy206rlec7.pdf 19

[39] The ATLAS Collaboration, "Atlas pixel detector electronics and sensors," *Journal of Instrumentation*, vol. 3, no. 07, p. P07007, 2008. [Online]. Available: http://stacks.iop.org/1748-0221/3/i=07/a=P07007 20

[40] A. Abdesselam and et al, "The barrel modules of the atlas semiconductor tracker," *Nuclear Instruments and Methods in Physics Research Section A: Accelerators, Spectrometers, Detectors and Associated Equipment*, vol. 568, no. 2, pp. 642 – 671, 2006. [Online]. Available: http://www.sciencedirect.com/science/article/pii/S016890020601388X 21

[41] The ATLAS TRT Collaboration, "The atlas trt barrel detector," *Journal of Instrumentation*, vol. 3, no. 02, p. P02014, 2008. [Online]. Available: http://stacks.iop.org/1748-0221/3/i=02/a=P02014 21

[42] G. Aad *et al.*, "The ATLAS Inner Detector commissioning and calibration," *Eur. Phys. J.*, vol. C70, pp. 787–821, 2010. 21

[43] I. Koletsou, "The atlas liquid argon calorimeter at the lhc," *Nuclear Instruments and Methods in Physics Research Section A: Accelerators, Spectrometers, Detectors and Associated Equipment*, vol. 628, no. 1, pp. 351 – 354, 2011, vCI 2010. [Online]. Available: http://www.sciencedirect.com/science/article/pii/S016890021001541X 22

[44] D. Scannicchio, "Atlas trigger and data acquisition: Capabilities and commissioning," *Nuclear Instruments and Methods in Physics Research Section A: Accelerators, Spectrometers, Detectors and Associated Equipment*, vol. 617, no. 1, pp. 306 – 309, 2010, 11th Pisa Meeting on Advanced Detectors. [Online]. Available: http://www.sciencedirect.com/science/article/pii/S0168900209013382 24, 25

[45] M. Stockton, "The atlas level-1 central trigger," *Journal of Instrumentation*, vol. 6, no. 01, p. C01075, 2011. [Online]. Available: http://stacks.iop.org/1748-0221/6/i=01/a=C01075 24

[46] S. Ask, D. Berge, P. Borrego-Amaral, D. Caracinha, N. Ellis, P. Farthouat, P. GÃčllnÃű, S. Haas, J. Haller, P. Klofver, A. Krasznahorkay, A. Messina, C. Ohm, T. Pauly, M. Perantoni, H. P. L. Junior, G. Schuler, D. Sherman, R. Spiwoks, T. Wengler, J. M. de Seixas, and R. T. Teixeira, "The atlas central level-1 trigger logic and ttc system," *Journal of Instrumentation*, vol. 3, no. 08, p. P08002, 2008. [Online]. Available: http://stacks.iop.org/1748-0221/3/i=08/a=P08002 25

[47] B. Stelzer, "The new small wheel upgrade project of the atlas experiment," *Nuclear and Particle Physics Proceedings*, vol. 273-275, pp. 1160 – 1165, 2016, 37th International Conference on High Energy Physics (ICHEP). [Online]. Available: http://www.sciencedirect.com/science/article/pii/S2405601415006719 26

[48] K. Ntekas, "The ATLAS New Small Wheel Upgrade Project," May 2014. [Online]. Available: https://cds.cern.ch/record/1703718 26

[49] A. Abusleme and et al, "Performance of a Full-Size Small-Strip Thin Gap Chamber Prototype for the ATLAS New Small Wheel Muon Upgrade," *Nucl. Instrum. Methods Phys. Res., A*, vol. 817, no. arXiv:1509.06329, pp. 85–92. 10 p, Sep 2015. [Online]. Available: http://cds.cern.ch/record/2054249 27

[50] T. Kawamoto, S. Vlachos, L. Pontecorvo, J. Dubbert, G. Mikenberg, P. Iengo, C. Dallapiccola, C. Amelung, L. Levinson, R. Richter, and D. Lellouch, "New Small Wheel Technical Design Report," Tech. Rep. CERN-LHCC-2013-006. ATLAS-TDR-020, Jun 2013, aTLAS New Small Wheel Technical Design Report. [Online]. Available: https://cds.cern.ch/record/1552862 27, 28, 30

[51] E. P. Codina, "Small-strip thin gap chambers for the muon spectrometer upgrade of the atlas experiment," *Nuclear Instruments and Methods in Physics Research Section A: Accelerators, Spectrometers, Detectors and Associated Equipment*, vol. 824, pp. 559 – 561, 2016, frontier Detectors for Frontier Physics: Proceedings of the 13th Pisa Meeting on Advanced Detectors. [Online]. Available: http://www.sciencedirect.com/science/article/pii/S0168900215014692 28, 29, 81

[52] Y. Giomataris, P. Rebourgeard, J. Robert, and G. Charpak, "Micromegas: a high-granularity position-sensitive gaseous detector for high particle-flux environments," *Nuclear Instruments and Methods in Physics Research Section A: Accelerators, Spectrometers, Detectors and Associated Equipment*, vol. 376, no. 1, pp. 29 – 35, 1996. [Online]. Available: http://www.sciencedirect.com/science/article/pii/0168900296001751 29, 30

[53] M. Bianco, "Micromegas detectors for the muon spectrometer upgrade of the atlas experiment," *Nuclear Instruments and Methods in Physics Research Section A: Accelerators, Spectrometers, Detectors and Associated Equipment*, vol. 824, pp. 496 – 500, 2016, frontier Detectors for Frontier Physics: Proceedings of the 13th Pisa Meeting on Advanced Detectors. [Online]. Available: http://www.sciencedirect.com/science/article/pii/S0168900215014503 30

[54] G. Sekhniaidze, "Construction and performance of the stgc and micromegas chambers for atlas nsw upgrade," *Journal of Instrumentation*, vol. 12, no. 03, p. C03020, 2017. [Online]. Available: http://stacks.iop.org/1748-0221/12/i=03/a=C03020 31

[55] B. Lefebvre and B. Vachon, "Characterization studies of small-strip Thin Gap Chambers for the ATLAS Upgrade," Aug 2018, presented 2018. [Online]. Available: http://cds.cern.ch/record/2633639 33, 35

[56] S. Majewski, G. Charpak, A. Breskin, and G. Mikenberg, "A thin multiwire chamber operating in the high multiplication mode," *Nuclear Instruments and Methods in Physics Research*, vol. 217, no. 1, pp. 265 – 271, 1983. [Online]. Available: http://www.sciencedirect.com/science/article/pii/0167508783901461 35

[57] R. Keyes, K. Johnson, L. Pepin, F. Léger, C. Qin, S. Webster, A. Robichaud-Véronneau, C. Bélanger-Champagne, B. Lefebvre, S. Robertson, A. Warburton, B. Vachon, and F. Corriveau, "Development and characterisation of a gas system and its associated slow-control system for an atlas small-strip thin gap chamber testing facility," *Journal of Instrumentation*, vol. 12, no. 04, p. P04027, 2017. [Online]. Available: http://stacks.iop.org/1748-0221/12/i=04/a=P04027 35, 36, 37, 38

[58] G. Iakovidis, "VMM3, an ASIC for Micropattern Detectors," CERN, Geneva, Tech. Rep. ATL-MUON-PROC-2018-003, Mar 2018. [Online]. Available: http://cds.cern.ch/record/2309951 46

[59] B. Vachon, Private Communication, 2018. 60, 63

[60] R. Brun and F. Rademakers, "ROOT: An object oriented data analysis framework," *Nucl. Instrum. Meth.*, vol. A389, pp. 81–86, 1997. 64

[61] J. A. Högbom, "Aperture Synthesis with a Non-Regular Distribution of Interferometer Baselines," *Astronomy and Astrophysics, Supplement*, vol. 15, p. 417, Jun. 1974. 66